

Strain and Strain Gradient Measurement Using Fibre Bragg Grating Sensors

By
Michael C. Kennedy B.Sc.

Submitted for the degree of Doctor of Philosophy

Presented to
Dublin City University

Research Supervisor

Dr. Vincent Ruddy,
School of Physical Sciences,
Dublin City University.

September 1999

List of symbols		List of symbols	
a	Fiber core radius	μ_0	Permeability of free space
α	Refractive index apodisation parameter	n_1	Refractive index n_1 =core, n_2 =cladding
α_T	Coefficient of thermal expansion	n_{eff}	Effective refractive index of an optical mode in a fibre core
b	Interference filter half width at half maximum	n^*	Effective refractive index of a Fabry-Perot interference filter
β	Core mode propagating constant	ν	Poisson's ratio
δ	A small difference	p_e	Effective photoelastic constant
Δ	Fibre refractive index profile height ($\Delta = n_1^2 - n_2^2 / 2n_1^2$)	p_y	p_{11}, p_{12} , Pockel's piezo coefficients of the stress optic tensor
Δx	A small change in x	pm	Pico-meters
$\overline{\delta n_{eff}}$	Mean amplitude of the refractive index modulation	$\phi(z)$	Phase of refractive index modulation
E	Electric field of the electromagnetic wave	$R(z)$	E field of incident wave on fibre Bragg grating
ε	Mechanical strain	ρ	Amplitude reflection coefficient
ε_0	Permittivity of free space	ρ^2	Power reflection coefficient
ξ	Thermo-optic coefficient	$S(z)$	E field of reflected wave on fibre Bragg grating
g	Gradient of strain $\delta\varepsilon / \delta Z$	t	Time
g_s	Gauge factor of wire strain guage	U	Fibre core mode parameter
i	$\sqrt{-1}$, square root of -1	V	Fibre normalised frequency
$J_l(z)$	Bessel function of the first kind of order l of the function z	W	Fibre cladding mode parameter
K_ε	Wavelength/strain coefficient	W_G	Gaussian $1/e$ half linewidth
K_T	Wavelength/temperature coefficient	ω	Angular frequency of electromagnetic wave
$K_l(z)$	Modified Bessel function of the second kind of order l of the function z	z	Position along a fibre core axis
$\kappa(z)$	Mode power coupling coefficient	Z	Characteristic impedance $= \sqrt{\mu / \varepsilon}$
L	Grating length	Z_0	Characteristic impedance of free space $= \sqrt{\mu_0 / \varepsilon_0}$
L_C	Cantilever length		
λ	Wavelength		
λ_B	Bragg wavelength		
Λ	Grating spatial periodicity in length		

DECLARATION

I hereby certify that this material, which I now submit for assessment on the programme of study leading to the award of Doctor of Philosophy, is entirely my own work and has not been taken from the work of others, save and to the extent that such work has been cited and acknowledged within the text of my work.

Signed: Michael Kennedy
Candidate

Date: 13/12/1999

Acknowledgements

I would firstly, and most importantly like to thank my parents, Maura, Christy and my sister Christina for all their support over the duration of this work. Without them I am sure none of this would ever have come to fruition.

Secondly I feel indebted to Dr. Vince Ruddy for the tremendous amount of effort he has put into this body of work. Without his constant encouragement and help, the past few years would not have been as enjoyable as they have been. I would also like to thank Dr. Brian Lawless for his many varied inputs to this work and the many 'off topic' conversations we have had over the years. The whole staff of the Physics Department have, I am sure, at some stage been quizzed on many of the aspects in this thesis, and for their help I am truly grateful. There are some of them who deserve a special mention because they answered more than their fair share of these. These people are Dr. Tony Cafolla, Dr. John Costello, Dr. John Paul Mosnier and Dr. Miles Turner.

And finally I must thank the many people who have made the difficult times bearable, most of them have absolutely no scientific background and gave inspiration often times without knowing it. These are in no particular order (except the first one) so don't worry if you find yourself at the end of the list!

Anne, Maurice, Nigel, Rob, Rolly, Br. (The Boss) McDonnell, Brian, Jim Fitzpatrick and family, Joe, Carmel, Amy, Kate, Terry, Andrew, Dawn, Stephen, Tony, Her Mick, Ann, Owen, Miriam, Tom, Steve, Paud, Aidan, Colm, Sarah-Jane, Tony NPT, Eileen, Kieran.

I wish to dedicate this work to the memory of Mary Hayden (1944-1997) and Charlie Orr (1913-1999) who through their outlook on life gave me the strength to work on even when I felt like giving up.

Abstract

The use of apodised in-fibre Bragg gratings in the measurement of both strain and strain gradient is discussed. A system of two Bragg gratings of similar but slightly displaced Bragg wavelength, joined using a 3dB coupler was used with a specially designed spectrum analyser of approximately nine picometers wavelength resolution. This consisted of a scanning Fabry Perot interference filter and photodiode detector unit interfaced to a PC. The reflection spectrum of both gratings, one exposed to strain, the other used as a temperature-referencing channel, was constructed using a Voigt type deconvolution. A directed evolution software algorithm was used as a line fitting routine to extract both the Bragg wavelengths and linewidths of the light back reflected from the gratings. A cantilever type strain rig in a temperature-controlled environment was used to create known strain and strain gradient fields. The variations in the Bragg wavelength with strain over a -400 to +600 microstrain range was measured from which the strain sensitivity of 0.962 ± 0.002 pm/microstrain, at ~ 1300 nm was determined. The temperature sensitivity was also evaluated. The linewidth of the back reflected spectrum from the Bragg grating was measured as a function of strain gradient (g) over the range -1.0 to +1.5 microstrain per mm and was fitted to a quadratic in g . This functional form was explained using a model based on coupled mode theory applied to apodised gratings.

Chapter 1 Introduction to Fibre Bragg Gratings 1

1.1 Introduction: 1

1.2 Mode propagation in step-index fibres:..... 2

1.3 Single mode fibres: 4

1.4 Bragg gratings in singlemode fibres: 5

1.5 Bragg gratings as strain sensors..... 12

1.6 Conclusions 14

1.7 References 15

Chapter 2 Theory of Fibre Bragg gratings 17

2.1 Introduction 17

2.2 Coupled mode theory 17

2.3 Reflection coefficient of first order diffraction in a Bragg grating 21

2.4 Apodised Grating Spectra 30

2.5 Factors which affect the values of λ_0 and W , the central wavelength and linewidth of the reflection spectrum 39

2.5.1 Temperature 40

2.5.2 , Strain 41

2.5.3 Strain Gradient 43

2.6 Simulation techniques 45

2.6.1 Transfer matrix method 46

2.6.2 Rouards’s method 47

2.7 Conclusions 48

2.8 References 49

Chapter 3 Bragg Grating Fabrication 52

3.1 Introduction 52

3.2 The Mechanism of refractive index modulation. 52

3.3 Standing wave Grating (The two beam interferometer)..... 55

3.4 Holographic Gratings..... 55

3.5 Phase Mask Grating Writing 57

3.6 Type I and Type II Bragg gratings 60

3.7 Laser selection for writing fibre Bragg gratings..... 60

3.8 Conclusions 61

3.9 References 63

Chapter 4 Fibre Bragg grating sensing 65

4.1 Introduction 65

4.2 Variation of Bragg wavelength and linewidth with strain..... 66

4.3 Variation of Bragg wavelength and linewidth with temperature..... 68

4.4 Simultaneous strain and temperature measurement 70

4.4.1 Reference fibre Bragg grating 70

4.4.2 Dual-wavelength superimposed fibre Bragg gratings 70

4.4.3 Harmonics Method 71

4.4.4 Dual Diameter fibre Bragg grating 71

4.4.5 Extrinsic techniques 73

4.5	Strain Gradient.....	73
4.6	Other external effects.....	75
4.6.1	Pressure	75
4.6.2	Dynamic Magnetic Field	76
4.7	Conclusions	78
4.8	References	79
Chapter 5	<i>Design of a strain sensor system with temperature compensation.....</i>	80
5.1	Introduction	80
5.2	Twin fibre approach.....	81
5.3	Wavelength analyser	84
5.3.1	Commercial systems.....	84
5.3.2	Multi-layer interference filter	85
5.3.3	Optical source considerations and selection	89
5.3.4	Optical detector considerations and selection.....	90
5.3.5	Grin lens	92
5.3.6	Fibre couplers.....	93
5.4	Automating wavelength analysis.....	95
5.5	The cantilever strain rig.....	99
5.6	Conclusion.....	102
5.7	References	105
Chapter 6	<i>Deconvolution of Spectra</i>	107
6.1	Introduction	107
6.2	Genetic algorithm approach to find solution in large search space	108
6.3	Directed evolution system	112
6.4	Using a Voigt function as the experimental lineshape.....	116
6.5	Conclusion.....	119
6.6	References	121
Chapter 7	<i>Measurement of Strain and Strain Gradient using a pair of Bragg grating gauges. 122</i>	122
7.1	Introduction	122
7.2	Calibration of cantilever using wire strain gauges	122
7.3	Variation of Bragg wavelength with strain	125
7.4	Variation of Bragg wavelength with temperature.....	130
7.5	Variation of linewidth with strain gradient	132
7.6	Conclusion.....	136
7.7	References	137
Chapter 8	<i>Discussion of experimental results and conclusions.....</i>	138
8.1	Introduction	138
8.2	Variation of Bragg wavelength with strain	138
8.3	Variation of Bragg wavelength with temperature.....	142
8.4	Variation of linewidth with strain gradient	143
8.5	Further Work	145
8.6	Conclusions	146

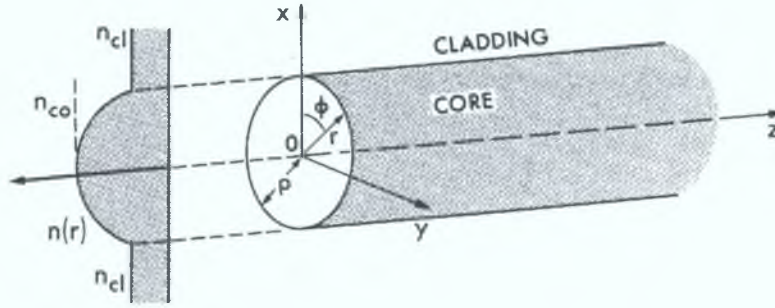
8.7	References	147
<i>Appendix A</i>		149
A.1	Hyperbolic functions of complex variables	149
A.2	Inverse trigonometric functions	149
A.3	Useful complex number relations.....	149
<i>Appendix B System Specification Sheets</i>		150
B.1	Fibre Specifications	150
B.2	Photodiode.....	151
B.3	ELED.....	155
B.4	Electronics.....	159
B.4.1	Photodiode Amplifier Circuit	159
B.4.2	ELED Driver Circuit	159
B.5	Grin Lens	160
B.6	Stepper Motor.....	163
B.7	Gearbox.....	166
B.8	Strain Gauge	168
<i>Appendix C C Code listings</i>		171
C.1	Program 1: Control rotation stage and sample data from photodiode amplifier	171
C.2	Program 2: Convert multi-scan datafile into single scan data files.....	177
C.3	Program 3: Genetic Algorithm for deconvolution of spectra	178
C.4	Program 4: Routines to test viability of deconvolution system.....	189
C.5	Program 5: Simulation of Bragg grating with apodisation.....	204

Chapter 1 Introduction to Fibre Bragg Gratings

1.1 Introduction:

Optical fibres are waveguides of optical radiation in which waves can propagate by total internal reflection. These waves consist of oscillating E and H fields in the fibre core with spatially decaying evanescent fields in the waveguide claddings. If the cores of such waveguides are modified by either a periodic modulation of their diameter or refractive index then light propagating in the core will be diffracted by the periodic grating-like structure. This diffraction, which is analogous to the scattering of X-ray radiation in crystal lattices, is called Bragg diffraction and the perturbation of the fibre is called a Bragg grating. The presence of a grating – consisting of a periodic refractive index in an optical fibre – can cause the coupling of light into counter propagating modes when it travels along the fibre. In this chapter the diffraction of light in step index singlemode fibre gratings and the use of the back reflected light to interrogate the grating spacing is discussed. Mode propagation in singlemode fibres is outlined and the occurrence of counter propagation modes due to the resonant coupling created by the grating is discussed in terms of a simple model of Fresnel reflection from the gratings ‘rulings’ and the more rigorous model of mode coupling. The use of diffracted light, or counter propagating optical modes to interrogate the grating, via its wavelength, is discussed with special reference to the strain field to which the grating is exposed.

1.2 Mode propagation in step-index fibres:



In a step index cylindrical waveguide consisting of a core of radius a and a refractive index n_1 surrounded by an infinite ($r \gg a$) cladding of refractive index n_2 ($n_1 > n_2$) light of vacuum wavelength λ will propagate as a series of modes with core and cladding E-fields given respectively by

$$\begin{aligned} E_{core} &= AJ_l(UR) \cos(l\phi) \exp[i(\omega t - \beta z)] \\ E_{cladding} &= AK_l(WR) \cos(l\phi) \exp[i(\omega t - \beta z)] \\ R &= r/a \end{aligned} \quad \text{E 1.1}$$

The above functions are solutions of the scalar wave equation in cylindrical polar coordinates (r, ϕ, z) . ω is the angular frequency of the light wave vibration and β is the mode propagation constant. The functional form of the field shows a radial dependence $J_l(UR)$ in the core and a plane wave like behaviour in the z direction with a periodicity of β . The core mode parameter U and the cladding-mode parameter W are related to the vacuum wavenumber k ($= 2\pi/\lambda$) by

$$U = a\sqrt{n_1^2 k^2 - \beta^2} \quad ; \quad W = a\sqrt{\beta^2 - n_2^2 k^2} \quad \text{E 1.2}$$

and U and W are related through the normalised frequency V of the waveguide given by

$$V^2 = U^2 + W^2 = a^2 k^2 (n_1^2 - n_2^2) \quad \text{E 1.3}$$

U and W are real quantities i.e. from Equation 1.2 β lies in the range

$$n_2 k \leq \beta \leq n_1 k \quad \text{E 1.4}$$

The mode propagation constant β divided by k is sometimes referred to as the mode effective index, which by Equation 1.4 is bounded in

$$n_2 \leq n_{\text{eff}} \leq n_1 \quad \text{E 1.5}$$

The functions J_l and K_l are Bessel functions of the first kind of order l and modified Bessel functions of the second kind respectively. For large arguments UR and WR respectively the Bessel $J_l(UR)$ is approximately a damped sinusoidal wave function while $K_l(WR)$ is an exponentially decaying function in the cladding as shown in Figure 1.1.

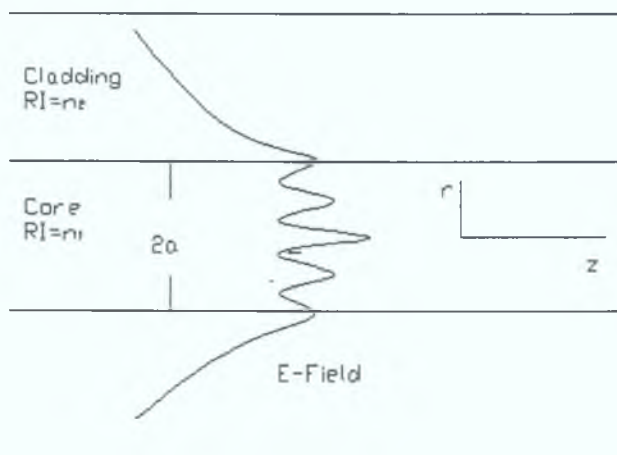


Figure 1.1

The eigenvalues U and W are solutions of the eigenvalue equation based upon two boundary conditions at the interface $R = 1$ (i.e. $r = a$). These conditions are the

continuity of the radial E field and its derivative at the interface and arise because of the continuity of E_{\perp} and D_{\parallel} at an interface of two dielectrics under the conditions that n_1 and n_2 are not significantly different in magnitude – the so-called ‘weakly guiding’ condition. This is discussed in detail in such texts as “*Optical Waveguide Theory*” by Snyder and Love [1] and “*Theory of Dielectric Optical Waveguides*” by Marcuse [2].

1.3 Single mode fibres:

When the waveguides V number is less than 2.045 (the first solution of $J_1(V) = 0$) then only one mode, the $l = 0, m = 1$ mode can be sustained in the waveguide.

Because the Bessel $J_0(UR)$ is approximately Gaussian in shape the fundamental $l = 0, m = 1$ mode has a spatial intensity distribution which peaks on the core axis ($r = R = 0$) and decays radially into the core ($r \leq a$) and in the cladding $r > a$. The E-field wavefunctions for this mode are, since $l = 0$, by Equation 1.1

$$\begin{aligned} E_{core} &= AJ_0(UR) \exp[i(\omega t - \beta z)] \\ E_{cladding} &= BK_0(UR) \exp[i(\omega t - \beta z)] \end{aligned} \quad \text{E 1.6}$$

, where the core mode parameter U and cladding parameter W ($= \sqrt{V^2 - U^2}$) satisfy the simplified eigenvalue equation

$$\boxed{\frac{U J_1(U)}{J_0(U)} = \frac{W K_1(W)}{K_0(W)}} \quad \text{E 1.7}$$

For a particular waveguide (i.e. one for which the normalised frequency V is known, and is less than 2.405) trial solutions of U in $(0, V)$ and W ($= \sqrt{V^2 - U^2}$) may be inserted in Equation 1.7 to find the first root of the eigenvalue equation to specify the

spatial distribution of the fundamental mode of the waveguide through a determination of U (and from it W).

1.4 Bragg gratings in singlemode fibres:

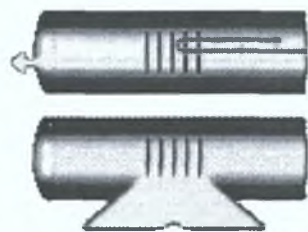


Figure 1.2

By an in-fibre Bragg grating is meant a periodic refractive index profile in z along the axis of a section of fibre core created by some means as shown in Figure 1.2.

If the core refractive index in the grating section of the fibre has a sinusoidal axial variation i.e. $n(z)$ can be written in the form

$$n(z) = n_0 + (\Delta n) \cos\left(\frac{2\pi z}{\Lambda}\right)$$

E 1.8

, where (Δn) represents the modulation depth of the refractive index variation created in the grating and Λ is the periodicity of the refractive index profile along the fibre axis (in the z direction). n_0 is the mean value of the core refractive index about which the periodic variation oscillates.

When light of vacuum wavelength λ , or propagation constant β ($= n_{eff} k = 2\pi n_{eff} / \lambda$) in the form of the fundamental mode of the fibre waveguide is incident on the grating some of the optical power is reflected at each ruling due to the “impedance mismatch” which is refractive index dependant. The characteristic impedance of the waveguide core (Z) is given by the ratio of the E and H fields of the optical mode and is expressed by

$$Z = \frac{1}{n} \sqrt{\frac{\mu_0}{\epsilon_0}} = \frac{Z_0}{n}$$

E 1.9

, Z_0 is the characteristic impedance of free space $\sqrt{\mu_0/\epsilon_0}$ or about 376 ohms, and n is

the refractive index of the glass of the core. The amplitude reflection coefficient at an

interface between media of characteristic impedances Z_1 and Z_2 is known to be

$\frac{(Z_2 - Z_1)}{(Z_2 + Z_1)}$ for normal incidence. If the grating has a ruling spacing which varies with

position along the waveguide then the wavelets reflected from successive rulings will

be progressively more and more out of phase and as a result interfere destructively. If,

however the propagation constant β of the mode i.e. the spatial frequency of the

wavetrain in the z direction is half the spatial frequency ($2\pi/\Lambda$) of the rulings the

wavelets which are back reflected will all be in phase and interfere constructively.

This condition is given by

$$\beta = \frac{1}{2}(2\pi/\Lambda)$$

or using $\beta = n_{eff} k$ this reduces to

$$\lambda_B = 2n_{eff} \Lambda$$

E 1.10

This is the Bragg condition for first order diffraction of radiation incident normal to

the plane of the grating ($2d \sin \theta = n\lambda$, with $\theta = 90^\circ$ and $n = 1$). The Bragg condition

is modified from a vacuum wavelength λ to λ/n_{eff} for light in the waveguide core.

An analysis of the amplitude of the back reflected light based upon coherent Fresnel

reflection from the successive layers can be shown to be given by

$$\rho = \tanh \left[2 \left(\frac{\Delta n}{n} \right) L / \Lambda \right]$$

or using Equation 1.10

$$\rho \cong \tanh \left[4(\Delta n) \frac{L}{\lambda_B} \right] \quad \text{E 1.11}$$

where L is the total length of the grating.

The power reflection coefficient (ρ^2) is then

$$\rho^2 \cong \tanh^2 \left[4(\Delta n) \frac{L}{\lambda_B} \right] \quad \text{E 1.12}$$

As the argument $4(\Delta n) \frac{L}{\lambda_B}$ increases, the power reflection coefficient ρ^2 approaches 1.0 ($\tanh(x)=0.996$ at $x=1$) showing that the reflectivity of the grating at the Bragg wavelength may be extremely high – provided $L(\Delta n)$ is comparable in magnitude to λ_B . The spectral linewidth of the reflected light has been quoted by Inoue et al (1995) to be

$$\Delta\lambda_B \approx \left(\frac{\lambda_B^2}{\pi n L} \right) \sqrt{\pi^2 + \left(\frac{\pi \Delta n L}{\lambda_B} \right)^2}$$

or approximately

$$\Delta\lambda_B \approx \frac{\lambda_B^2}{nL} \quad \text{E 1.13}$$

when $(\Delta n)L \ll \lambda_B$. With L , typically of the order of millimeters and λ_B of the order of microns the linewidth is small, of the order of 1nm or less.

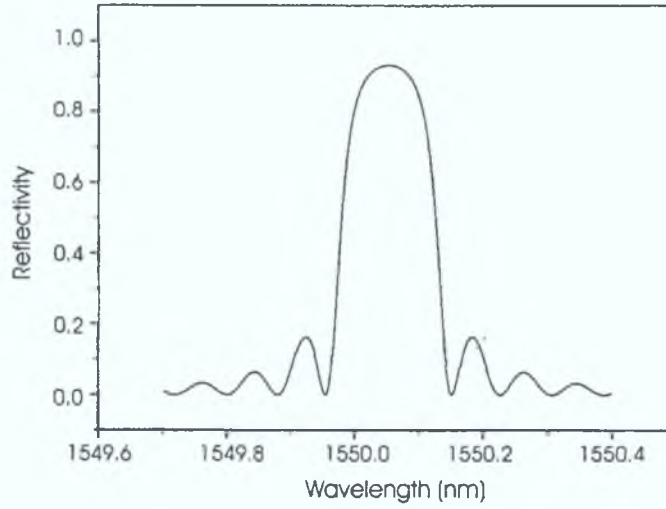


Figure 1.2

(From *Fiber Bragg Gratings*, Othonos & Kalli 1999 $\Delta n = 3.0 \times 10^{-4}$, $L = 2.0 \text{ mm}$)

It is evident from Equation 1.12 that the grating reflectivity at the Bragg wavelength λ_B increases with the total ruled length (L) and the amplitude of the refractive index (Δn) impressed in the fibre. As the impedance mismatch ($Z_2 - Z_1$) depends directly on (Δn) and since ρ^2 in turn scales as $(Z_2 - Z_1)^2$ this effect is not surprising.

The creation of a back reflected or counter propagating fundamental mode by a (periodic) grating in a fibre may also be treated by “coupled mode theory”, in which the grating is treated as a perturbation to the waveguide. Taking the z component of the perturbation Hamiltonian as

$$\cos(2\pi z/\Lambda)$$

E 1.14

the incident wavefunction of the singlemode fibre (without the grating) is, by perturbation theory [5] changed by an amount proportional to the matrix element

$$(H_1)_{jk} \text{ or}$$

$$(H_1)_{\beta-\beta'} = \int_{-L/2}^{L/2} \exp(-i\beta z) \cdot \cos\left(\frac{2\pi z}{\Lambda}\right) \cdot \exp(i\beta' z) dz \quad \text{E 1.15}$$

for a forward propagating mode of propagation constant β coupled to a backward propagating mode of propagation constant $-\beta'$. The perturbation shown in Equation 1.14 can be expressed in the form of

$$\frac{1}{2} \left\{ \exp\left(\frac{i2\pi z}{\Lambda}\right) + \exp\left(-\frac{i2\pi z}{\Lambda}\right) \right\}$$

the matrix element $(H_1)_{\beta,-\beta'}$ has terms of the form

$$\frac{\sin\left(\frac{2\pi}{\Lambda} + \beta - \beta'\right) \frac{L}{2}}{\left(\frac{2\pi}{\Lambda} + \beta - \beta'\right)} \quad \text{E 1.16}$$

and

$$\frac{\sin\left(-\frac{2\pi}{\Lambda} + \beta - \beta'\right) \frac{L}{2}}{\left(-\frac{2\pi}{\Lambda} + \beta - \beta'\right)} \quad \text{E 1.17}$$

When L is a large number, compared to Λ , both these expressions (Equation 1.16 and 1.17) are representations of the Dirichlet form of the Dirac delta function and so the perturbation to the incident waveform is proportional to

$$\delta\left(\frac{2\pi}{\Lambda} + \beta - \beta'\right) + \delta\left(-\frac{2\pi}{\Lambda} + \beta - \beta'\right) \quad \text{E 1.18}$$

This can be seen in “*Quantum Mechanics*” by Blokinsteve [6] for the analogous case of scattering by a periodic potential. [Here $\delta(x)$ is the Dirac delta function]. Because of the delta function the perturbation to the wavefunction has finite values only at

$$\frac{2\pi}{\Lambda} = \beta' - \beta \quad \text{and} \quad \frac{2\pi}{\Lambda} = \beta - \beta' \quad \text{E 1.19}$$

If the forward propagating mode and backward propagating mode are both fundamental modes of the waveguide then $\beta' = -\beta$ and the condition in Equation 1.19 reduces to

$$\frac{2\pi}{\Lambda} = -2\beta \quad \text{and} \quad \frac{2\pi}{\Lambda} = +2\beta \quad \text{E 1.20}$$

The latter is identical to that derived in Equation 1.10, the so-called Bragg condition for $n = 1$ and $n = -1$ at normal incidence ($\theta = 90^\circ$). Thus at a wavelength λ_B given by $2n_{eff}\Lambda$ a grating of periodicity Λ creates a strong counter propagating mode to the incident forward propagating mode.

By treating the wave amplitude of the incident wave $X(z)$ and the amplitude of the counter propagating fundamental mode $Y(z)$ as shown in “*Optical Waveguide Theory*”, Snyder and Love (1983) [1], equations 27-27 (a & b) it can be shown that, using the boundary conditions $X(0) = 1$ at the ‘entrance face’ and $Y(L) = 0$ at the ‘exit face’ of the grating

$$\begin{aligned} X(z) &= \cosh\left(\frac{k\Delta nz}{2}\right) - \sinh\left(\frac{k\Delta nz}{2}\right) \tanh\left(\frac{k\Delta nL}{2}\right) \\ Y(z) &= \sinh\left(\frac{k\Delta nz}{2}\right) - \cosh\left(\frac{k\Delta nz}{2}\right) \tanh\left(\frac{k\Delta nL}{2}\right) \end{aligned} \quad \text{E 1.21}$$

The ratio of the reflected amplitude $Y(0)$ to the incidence amplitude $X(0)$ is therefore

$$\rho = -\tanh\left(\frac{k\Delta nL}{2}\right)$$

and the reflected power coefficient (ρ^2) is then

$$\rho^2 = \tanh^2 \left(\frac{\pi \Delta n L}{\lambda_B} \right) \quad \text{E 1.22}$$

at the Bragg wavelength.

Comparison of equations 1.22 and 1.12 for the reflection coefficient of the fundamental mode from a Bragg grating derived in one case from the impedance mismatch induced in the core refractive index and from coupled mode theory show a common dependency on $(\Delta n) L / \lambda_B$, the simpler (impedance mismatch) approach having a factor of π instead of the factor of 4 from the more extensive coupled mode approach.

The case of contra directional coupling of light from a medium where a diffraction grating is created in it by a propagating acoustic wave, the so called ‘acousto-optic effect’ is treated in various texts such as “*Optical Electronics*” by Ghatak and Thyagarajan [10] and “*Fundamentals of Photonics*” by Saleh and Teisch [11]. The acousto-optic effect at ‘large Bragg angles’ is treated in section 18.5.2 of the former and they too predict a reflection coefficient similar to that shown in equation 1.12 [See equation 18.96 Ghatak and Thyagarajan]. In the acousto-optic effect the Bragg condition is a result of momentum conservation where the wavevector of the diffracted beam \bar{k}_r is related to the incident wavevector \bar{k} and that of the sound wave \bar{q} by

$$\bar{k}_r = \bar{k} + \bar{q}$$

as shown in Saleh and Teich Equation 20.1-15.

Taking $\bar{k} = n_1 k = n_1 \frac{2\pi}{\lambda}$, $\bar{k}_r = -\frac{n_1 2\pi}{\lambda}$ and $\bar{q} = \frac{2\pi}{\Lambda}$ this vector form of the Bragg condition and that of equation 1.10 are reconciled (\bar{k}_r is negative being in the opposite direction vectorally to \bar{k}).

Provided the grating index profile is a pure cosine (or sine) function of position z along the fibre axis then it has only the spatial frequency $2\pi/\Lambda$ or Fourier component.

This gives rise to *only one* order of diffraction. This is analogous to Fraunhofer diffraction on a holographic (sinusoidal) grating where only a central maximum and two first order maxima ($n = +1$ and $n = -1$ in $d \sin \theta = n\lambda$) are observed [7]. If during manufacture the grating refractive index profile reaches saturation then one Fourier frequency alone cannot specify the transparency of the grating and multiple order diffraction – analogous to the case of the plane diffraction grating is observed.

If the grating is fabricated in a multimode ($V \gg 2.405$) step index fibre then for each wavelength of light there will be a group of possible modes each identified by a different value of β the propagation constant. As the Bragg condition is $2\beta = 2\pi/\Lambda$ there may be one β value which satisfies the condition so this particular wavelength will experience a high reflectivity. For another wavelength one of its modes may also satisfy the same condition. Thus, when polychromatic light is launched into the fibre the reflection from the grating will show a series of lines at various wavelengths. If the refractive index profile is transversely uniform (i.e. varying in the z direction only/constant in the xy plane) there is no induced intermode coupling however as the mode orthogonality condition is not changed by the grating.

1.5 Bragg gratings as strain sensors

We have seen that a sinusoidal refractive index profile grating in a step index fibre waveguide gives rise to first order Bragg diffraction of incident light at a “*particular wavelength*” of

$$\lambda_B = 2n_{eff} \Lambda$$

In this equation Λ is the periodicity of the index profile and n_{eff} is the effective index of the optical mode. As λ_B is a physically measurable quantity its’ magnitude can be used to infer the grating periodicity. By monitoring the “*shift*” in the Bragg wavelength of the light which is back reflected from the grating the change in Λ can be inferred. Similarly a structure to which the fibre grating is bonded, or in which it is embedded, may be monitored for changing strain. As the reflected light is not purely monochromatic but possesses a line structure this may be used to investigate how the strain varies across the length of the Bragg grating; in other words the strain gradient along the grating is responsible for a modification of the line structure.

This work describes measurements of strain and strain gradient via the wavelength structure of the counter propagating optical mode in a Bragg grating, the center wavelength being dependant on the mean strain across the grating and the linewidth measuring the strain gradient across it.

As temperature also affects both the terms n_{eff} and Λ in the Bragg equation E1.10, the wavelength and linewidth are also temperature dependant. The measurements made in this work remove the temperature sensitivity using two Bragg gratings of closely spaced wavelengths, one exposed to a strain field while the second experiences only changes in ambient temperature.

1.6 Conclusions

We have seen that the presence of a grating in a singlemode step index fibre (with rulings normal to the fibre axis) gives rise to a high reflection of an incident mode at a particular wavelength of light. This resonant effect is similar to Bragg diffraction at normal incidence but unlike the latter is predicted to occur only in the first order (if the grating has a sinusoidal refractive index profile in the z direction). This counter-propagating mode, of a particular wavelength light may be used to interrogate the grating periodicity Λ and monitor as a result the strain condition of the fibre grating and that of the structure to which it is bonded or in which it is embedded. This is the principle of the fibre Bragg grating sensor.

1.7 References

- [1] Snyder A.W. and Love J.D., "*Optical Waveguide Theory*", Chapman and Hall, London (1983)
- [2] Marcuse D., "*Theory of Dielectric Optical Waveguides*", Academic Press, NY (1974)
- [3] Haus H.A., "*Waves and Fields in Optoelectronics*", Prentice-Hall Inc., NY (1984)
- [4] Inoue A, Shigehana M, Ito M, Inai M, Hattori Y and Mizunami T.,
"Fabrication and Application of fiber Bragg grating – A review",
Optoelectronics – Devices and Technology (Japan) Vol 10 No 1 pg119-130
(1995)
- [5] Merzbacher E., "*Quantum Mechanics*", Wiley & Son, NY (1961)
- [6] Blokhintsev D.I., "*Principles of Quantum Mechanics*", Allyn and Bacon, Boston (1964)
- [7] Fowles G.R., "*Introduction to Modern Optics*", Dover Publications Inc, Toronto (1975)
- [8] Wansen K.H., Voss K.F. and Kersey A.D., "*Novel Fiber Devices and Sensors based on multimode fiber Bragg gratings*", 10th International Conference on Optical Fibre Sensors, Glasgow (1994) p265-268
- [9] Kittel C, "*Introduction to Solid State Physics*", Wiley & Sons Inc., NY, (1996)
Chapter 2

- [10] Ghatak A.K. and Thyagarafan, "*Optical Electronics*", Cambridge University Press, Cambridge (1989), Chapter 18 : Acoustooptic Effect-Bragg Diffraction
- [11] Saleh B.E.A. and Teich M.C., "*Fundamentals of Photonics*", Wiley & Son Inc., NY, (1991) Equation 20.1-15

Chapter 2 Theory of Fibre Bragg gratings

2.1 Introduction

The theory of the diffraction of light in a step index waveguide containing a spatially periodic refractive index profile is discussed in terms of the coupling of light energy between forward and backward propagating modes in the waveguide. The spectral profile of the counter propagating modes is developed for the simplest index profile where the periodic perturbation has a constant amplitude (the waveguide equivalent of the plane diffraction grating) and extended to the apodised grating where a position varying profile is superimposed on top of the periodic variation. The parameters that determine the line profile (intensity versus wavelength), the mode power coupling coefficient (κ) and detuning parameter (σ) are discussed and their importance in determining the lineshape (i.e. its central location in wavelength and linewidth) is highlighted.

2.2 Coupled mode theory

Light propagates in single mode (step index) fibres with an E-field which is given by,

$$J_0(UR) \exp[i(\omega t - \beta z)] \quad \text{E 2.1}$$

where $J_0(UR)$ represents the spatial amplitude in the radial direction ($R = r/a$), U is an eigenvalue of an eigenvalue equation and J_0 is the zero order Bessel function. The second term in equation 2.1 represents a plane wave modulation in the z (or axial) direction with angular frequency ω , and spatial periodicity β . For a bound mode β is constrained by the equation

$$n_2 k < \beta < n_1 k \quad \text{E 2.2}$$

where n_1 and n_2 are the refractive indices of the core and cladding respectively and k is the vacuum wavenumber of the light ($2\pi/\lambda$); λ is the vacuum (or air) wavelength of the light. β is called the propagation constant of the mode and because of the limiting condition in equation 2.2 is often written as

$$\beta = n_{\text{eff}} k \quad \text{E 2.3}$$

Here n_{eff} is called the “effective index” of the mode. The mode core parameter U is given by

$$U = a \sqrt{n_1^2 k^2 - \beta^2} \quad \text{E 2.4}$$

which is a dimensionless parameter which lies between 0 and V , the normalized frequency or “ V number” of the fibre

$$V = ka \sqrt{n_1^2 - n_2^2} \quad \text{E 2.5}$$

A mode propagating in the positive z direction will have a spatial modulation of

$$\exp[i(\omega t - \beta_1 z)] \quad \text{E 2.6}$$

while one counter-propagating in the opposite (or $-Z$ direction) will be specified by

$$\exp[i(\omega t + \beta_2 z)] \quad \text{E 2.7}$$

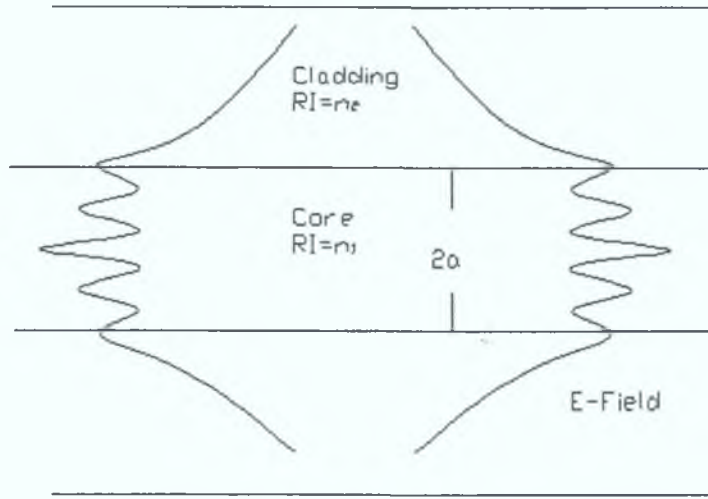


Figure 2.1

As well as having a modulation $J_0(UR)$ in the transverse direction in the core the modes also have an “evanescent tail” in the cladding given by

$$K_0(WR) \quad \text{E 2.8}$$

where K_0 is the modified Bessel function which has an approximately exponentially decaying functional form. W is called the “cladding mode parameter”, is defined by

$$W = a\sqrt{\beta^2 - n_2^2 k^2} \quad \text{E 2.9}$$

, is a real quantity (because of condition 2.2) and is related to U and V by

$$V^2 = U^2 + W^2 \quad \text{E 2.10}$$

If we now consider two modes of the fibre waveguide,

$$\begin{aligned} \psi_1 &= A_1 J_0(U_1 R) \exp[i(\omega t - \beta_1 z)] \\ \psi_2 &= A_2 J_0(U_2 R) \exp[i(\omega t - \beta_2 z)] \end{aligned}$$

subject to the perturbation of the form

$$\cos\left(\frac{2\pi}{\Lambda}z\right) \quad \text{E 2.11}$$

then using perturbation theory the coupling of energy between the initial state (ψ_1) and the final state (ψ_2) will be proportional to the matrix element

$$\int \exp(-\beta_1 z) \exp(2\pi i z / \Lambda) \exp(-\beta_2 z) dz \quad \text{E 2.12}$$

This integral has a delta function value having a value of 1.0 at

$$\beta_1 - \beta_2 = \pm \frac{2\pi}{\Lambda} \quad \text{E 2.13}$$

When $\beta_2 = -\beta_1$, equation 2.13 gives

$$\beta = \pm \frac{\pi}{\Lambda}$$

using equation 2.3 we get

$$\boxed{\lambda = 2n_{eff} \Lambda} \quad \text{E 2.14}$$

That is strong coupling of light from a forward propagating mode to a counter propagating one will occur at a (free space) wavelength λ given by $2n_{eff} \Lambda$, Λ is the periodicity of the perturbation in the waveguide. This is readily visualised as follows.

If the perturbation is in the refractive index of the glass of the fibre core then wavelets of the incident wave are continuously back reflected due to the mismatch in the refractive index. According to the Fresnel equations a refractive index change from $n(z)$ to $n(z + \delta z)$ gives rise to a power reflection of magnitude

$$\left\{ \frac{n(z) - n(z + \delta z)}{n(z) + n(z + \delta z)} \right\}^2 \quad \text{E 2.15}$$

as shown in many texts e.g. [3].

All the wavelets are in phase when the spatial periodicity β of the incident wave matches that of the periodicity Λ of the refractive index profile of the fibre core. This gives rise to the phase matching condition given by equation 2.2 which in turn is a simplification of the Bragg condition [4] for diffraction at normal incidence,

$$\begin{aligned} 2d \sin \theta &= n\lambda \\ \theta &= \text{grazing incidence angle} \\ n &= 1, 2, 3, \dots \end{aligned}$$

or in this case ($\theta = 90^\circ$)

$$2\Lambda = n\lambda \quad \text{E 2.16}$$

With $\lambda_{\text{waveguide}} = \lambda/n_{\text{eff}}$, we get from equation 2.16,

$$\lambda = \frac{2n_{\text{eff}}\Lambda}{n}$$

or a similar expression to 2.14 for the first order ($n = \pm 1$) diffraction. First order only diffraction is also a feature of a plane diffraction grating in which a sinusoidal transparency is imposed on the N evenly spaced apertures [5].

2.3 Reflection coefficient of first order diffraction in a Bragg grating

The development of the coupled mode formulation to describe in particular the coupling of the energy from the propagating mode to a counter propagating one was developed by many authors e.g. [6]. If $\bar{n}(x, y)$ and $n(x, y, z)$ are the refractive index profiles of the uniform waveguide and the section perturbed by the presence of the Bragg grating respectively then the E field of the light in the grating section satisfies the scalar wave equation

$$\left\{ \nabla_t^2 + k^2 n^2(x, y, z) + \frac{\partial^2}{\partial t^2} \right\} E(x, y, z) = 0 \quad \text{E 2.17}$$

where ∇_t^2 is the transverse component of the Laplacian operator. If the refractive index profile is given by

$$n^2(x, y, z) = \bar{n}^2(x, y) + \overline{\partial n_{eff}} \left\{ 1 + v \cos \left[\frac{2\pi z}{\Lambda} + \phi(z) \right] \right\} \quad \text{E 2.18}$$

and if the total field is written as the superposition of two counter propagating modes of propagation constants β and $-\beta$ i.e.

$$E(x, y, z) = R(z)E_1(x, y)\exp(-i\beta z) + S(z)E_2(x, y)\exp(i\beta z) \quad \text{E 2.19}$$

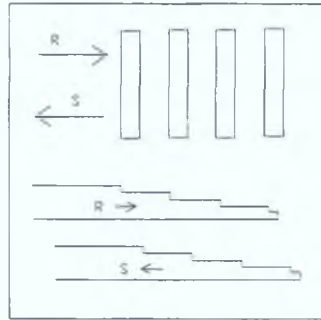


Figure 2.2

the wave equation gives rise to two first order equations for $R(z)$ and $S(z)$, the incident and reflected waves.

The wave equation generates two parameters κ , a mode coupling coefficient defined by

$$\kappa = \frac{\frac{kv}{2n_0} \int_{A_\infty} (n^2 - \bar{n}^2) E_1 E_2 dA}{\int_{A_\infty} E_1^2 dA} \quad \text{E 2.20}$$

, the integrals being over the fibre cross section A_∞ , and σ defined by

$$\hat{\sigma} = 2\pi n_{eff} \left\{ \frac{1}{\lambda} - \frac{1}{\lambda_D} \right\} + \frac{2\pi \overline{\delta n_{eff}}}{\lambda} - \dot{\phi}(z)/2 \quad \text{E 2.21}$$

$\hat{\sigma}$ represents the frequency deviation from the Bragg condition. We are using here the symbolism of Erdogan [7] namely:

- (i) $\overline{\delta n_{eff}}$ is the ‘dc’ refractive index change spatially averaged over a grating period
- (ii) v is the fringe visibility of the index change
- (iii) Λ is the grating period
- (iv) $\lambda_D = 2n_{eff}\Lambda$ is the design wavelength for Bragg diffraction
- (v) $\phi(z)$ is a phase term to allow for grating chirp

The first order equations for the incident wavefield $R(z)$ and the counter propagating wavefield $S(z)$ are then

$$\begin{aligned} \frac{dR}{dz} &= i\hat{\sigma}R(z) + i\kappa S(z) \\ \frac{dS}{dz} &= -i\hat{\sigma}S(z) - i\kappa R(z) \end{aligned} \quad \text{E 2.22}$$

where terms proportional to d^2R/dz^2 and d^2S/dz^2 have been neglected, on the assumption that $R(z)$ and $S(z)$ are slowly varying functions of z . These coupled mode equations which describe how the incident field $R(z)$ decreases and the reflected wave $S(z)$ increases in intensity as the wave motion penetrates more deeply into the grating are derived in detail in various texts [8,9,10]. The reflection spectrum is then S/R . If we express $y = S/R$ then the coupled mode equations (2.22) can be readily combined to yield

$$\frac{dy}{dz} + i\kappa y^2 + 2i\hat{\sigma}y + i\kappa = 0 \quad \text{E 2.23}$$

This is the Riccati equation for y [10]. The solution of this equation for constant coupling coefficient κ is simplified by the substitution given in [11]

$$y(z) = \frac{w'(z)}{w(z)} \left(\frac{1}{i\kappa} \right) \quad \text{E 2.24}$$

which turns the first order Riccati equation for y into the second order equation for w of

$$w'' + 2i\hat{\sigma}w' - \kappa^2 w = 0 \quad \text{E 2.25}$$

which is the equation of the damped harmonic oscillator with imaginary damping coefficient $2i\hat{\sigma}$. This has an exact solution [12] of

$$\begin{aligned} w &= c_1 \exp\{(\gamma - i\hat{\sigma})z\} + c_2 \exp\{(-\gamma - i\hat{\sigma})z\} \\ &= \exp(-i\hat{\sigma}z) \{C \cosh \gamma z + D \sinh \gamma z\} \end{aligned} \quad \text{E 2.26}$$

where $\gamma = \sqrt{\kappa^2 - \hat{\sigma}^2}$ and c_1, c_2, C and D are constants. Substituting 2.26 into equation 2.24 gives the reflection coefficients S/R as

$$\begin{aligned} \frac{S}{R} &= \left(\frac{1}{i\kappa} \right) \left(\frac{\frac{d}{dz} \{ \exp(-i\hat{\sigma}z) (C \cosh \gamma z + D \sinh \gamma z) \}}{\{ \exp(-i\hat{\sigma}z) (C \cosh \gamma z + D \sinh \gamma z) \}} \right) \\ &= \left(\frac{1}{i\kappa} \right) \left(\frac{\gamma C \sinh \gamma z + \gamma D \cosh \gamma z - i\hat{\sigma}C \cosh \gamma z - i\hat{\sigma}D \sinh \gamma z}{C \cosh \gamma z + D \sinh \gamma z} \right) \end{aligned} \quad \text{E 2.27}$$

If we chose our origin at $z = 0$ at the distal end of the grating

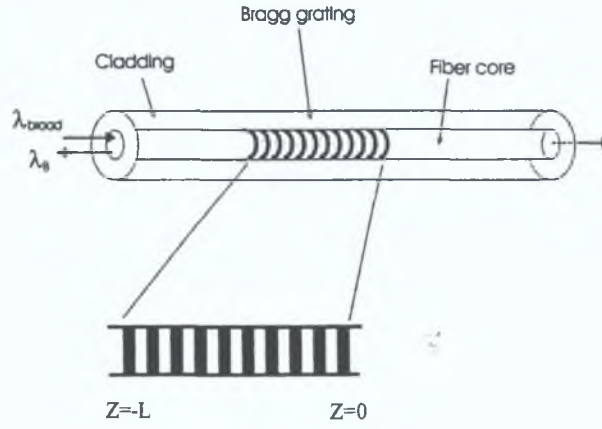


Figure 2.3

and invoke the criterion that $y = 0$ @ $z = 0$ then the boundary condition imposes the following relationship between C and D of equation 2.27.

$$\gamma D - i\hat{\sigma}C = 0 \tag{E 2.28}$$

$$\text{i.e. } D = \frac{i\hat{\sigma}}{\gamma} C$$

Then the reflection coefficient S/R simplifies to

$$y = \frac{1}{i} \left\{ \frac{\kappa \sinh \gamma z}{\gamma \cosh \gamma z + i\hat{\sigma} \sinh \gamma z} \right\} \tag{E 2.29}$$

Haus (1984) has developed a simplified derivation of this expression.

The intensity spectrum given by yy^* (where y^* is the complex conjugate of y) or

$$\frac{\kappa^2 \sinh^2 \gamma z}{\gamma^2 \cosh^2 \gamma z + \hat{\sigma}^2 \sinh^2 \gamma z}$$

$$\gamma = \sqrt{\kappa^2 - \hat{\sigma}^2}$$

This can also be expressed as

$$\frac{\sinh^2 \gamma z}{\cosh^2 \gamma z - \hat{\sigma}^2 / \kappa^2}$$

E 2.30

This expression predicts the intensity profile of the back reflected light from a Bragg grating in which the mode coupling coefficient – defined in 2.20 – is independent of z , as in equation 2.23. This applies to the case of a grating in which the refractive index perturbation is purely sinusoidal i.e. the fringe visibility v of equation 2.18 is a constant and the coupling coefficient κ is

$$\kappa = \frac{\pi}{\lambda} v \overline{\delta n_{eff}}$$

E 2.31

At the incident edge of the grating $z = -L$ the reflection spectrum is the given by

$$\frac{\sinh^2 \gamma L}{\cosh^2 \gamma L - \hat{\sigma}^2 / \kappa^2}$$

E 2.32

The wavelength dependence of this lineshape is determined by $\gamma = \sqrt{\kappa^2 - \hat{\sigma}^2}$. As both κ and $\hat{\sigma}$ are wavelength dependent (equations 2.31 and 2.21) γ can be either a purely real number or a purely imaginary one. When γ is imaginary ($\gamma = i\gamma'$) the term $\sinh^2 \gamma L \rightarrow i \sin \gamma' L$ and $\cosh^2 \gamma L \rightarrow \cos^2 \gamma' L$ in equation 2.30.

The spectral shape of the counter propagating mode from the grating (given by equation 2.32) can be plotted by taking values for $\overline{\delta n_{eff}}$, v , L and λ_D . Using

$\overline{\delta n_{eff}} = 2 \times 10^{-4}$, $v = 1$, $L = 2.5 \text{ mm}$ and $\lambda_D = 1555 \text{ nm}$ a spectrum of the following shape is predicted.

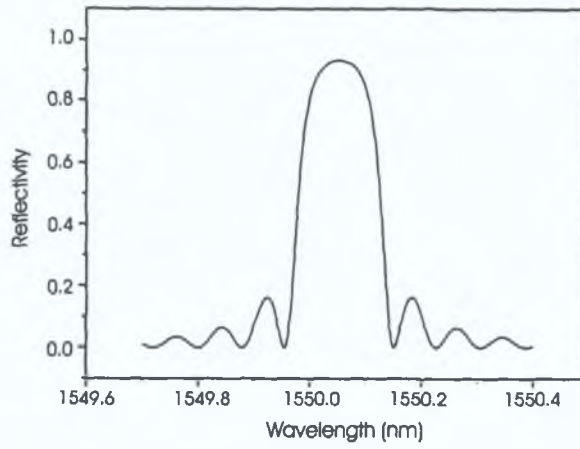


Figure 2.4

The spectrum

$$|y|^2 = \frac{\sinh^2 \sqrt{\kappa^2 - \hat{\sigma}^2} L}{\cosh^2 \sqrt{\kappa^2 - \hat{\sigma}^2} L - \hat{\sigma}^2}$$

E 2.33

has it's peak when

$\sinh \sqrt{\kappa^2 - \hat{\sigma}^2} L$ is a maximum

$\cosh \sqrt{\kappa^2 - \hat{\sigma}^2} L$ is a minimum

i.e. when

$$\hat{\sigma} = 0$$

From equation 2.21 $\hat{\sigma}$ is zero when

$$2\pi n_{eff} \left\{ \frac{1}{\lambda} - \frac{1}{\lambda_D} \right\} + \frac{2\pi \overline{\delta n_{eff}}}{\lambda} - \frac{\dot{\phi}(-L)}{2} = 0$$

If we call λ_0 the value of λ at which $\hat{\sigma} = 0$ then

$$\lambda_0 = \frac{\lambda_D \left(1 + \overline{\delta n_{eff}} / n_{eff}\right)}{1 + \lambda_D \dot{\phi}(-L) / 4\pi n_{eff}}$$

E 2.34

When the refractive index profile is exactly sinusoidal there is no chirping of the grating i.e.

$$\phi(z) = 0$$

E 2.35

$$\dot{\phi}(-L) = 0$$

$$\lambda_0 = \lambda_D \left\{1 + \overline{\delta n_{eff}} / n_{eff}\right\}$$

, and with $\overline{\delta n_{eff}} / n_{eff} \ll 1$

$$\lambda_{max} \cong \lambda_D$$

At the peak ($\hat{\sigma} = 0$) the term $\gamma = \kappa$ and the line intensity becomes

$$\tanh^2 \kappa L$$

E 2.36

When $\kappa L = 1.0$ $\tanh(\kappa L) = 0.76$ and the peak reflectivity is 0.58 or 58%. When $\kappa L = 1.5$ the peak reflectivity is $\cong 90\%$.

The first minimum of equation 2.33 occurs when $\hat{\sigma} = \pm \kappa$. Using equation 2.21 we get

$$\frac{\pi}{\lambda} v \overline{\delta n_{eff}} = \frac{2\pi n_{eff}}{\lambda} \left(1 + \overline{\delta n_{eff}} / n_{eff}\right) - \frac{2\pi n_{eff}}{\lambda_D} - \frac{\dot{\phi}(-L)}{2}$$

E 2.37

or

$$\frac{\pi}{\lambda} v \overline{\delta n_{eff}} = \pm 2\pi n_{eff} \left\{ \frac{1}{\lambda} - \frac{1}{\lambda_0} \right\}$$

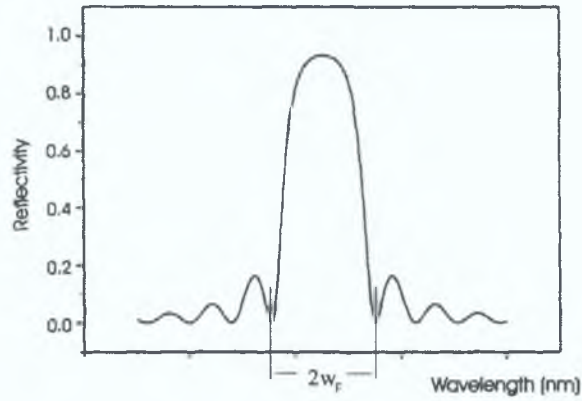


Figure 2.5

If we define the full width as W_F

then

$$W_F \cong \frac{v \overline{\delta n_{eff}} \lambda_0}{2 n_{eff} \left(1 + \overline{\delta n_{eff}} / n_{eff} \right)} \quad \text{E 2.38}$$

Using $\lambda \cong 2 n_{eff} \Lambda$ this reduces to

$$W_F \cong \Lambda \overline{\delta n_{eff}} \quad \text{E 2.39}$$

And the fractional linewidth W_F / λ_0 is

$$\frac{W_F}{\lambda_0} \cong \frac{v \overline{\delta n_{eff}}}{n_{eff}} \quad \text{E 2.40}$$

Taking, for example $\lambda_D = 1500 \text{ nm}$ and $\overline{\delta n_{eff}} = 1 \times 10^{-4}$ with $n_{eff} = 1.5$ for silica, the predicted linewidth W_F , for a fringe visibility of 1.0 is 0.1 nm. If light from a broadband source is launched into a fibre containing a Bragg grating then the incident and reflected spectrum (R and S) are

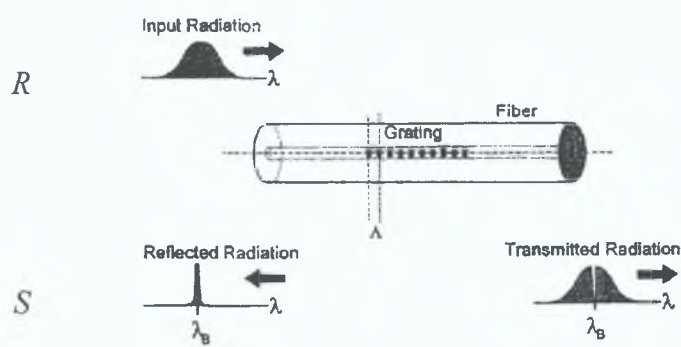


Figure 2.6

2.4 Apodised Grating Spectra

In a simple Bragg grating the refractive index modulation has a constant amplitude over a finite extent of the fibre core.

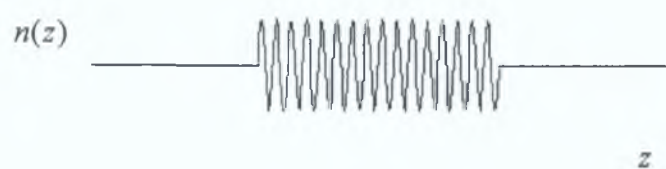


Figure 2.7

The Fourier spectrum of a sine function of infinite extent shows only power at one frequency. If the sine function is finite in extent there are other components in the frequency spectrum. These are caused by the abrupt edges of the grating and are a feature of the spectrum of plane diffraction gratings (in Fraunhofer diffraction) which show also secondary and higher order peaks. By smoothing the input and exit refractive index profiles of the Bragg grating these side lobes (or secondary peaks) can be reduced or removed completely. This process is called apodisation (literally “removing the feet”).

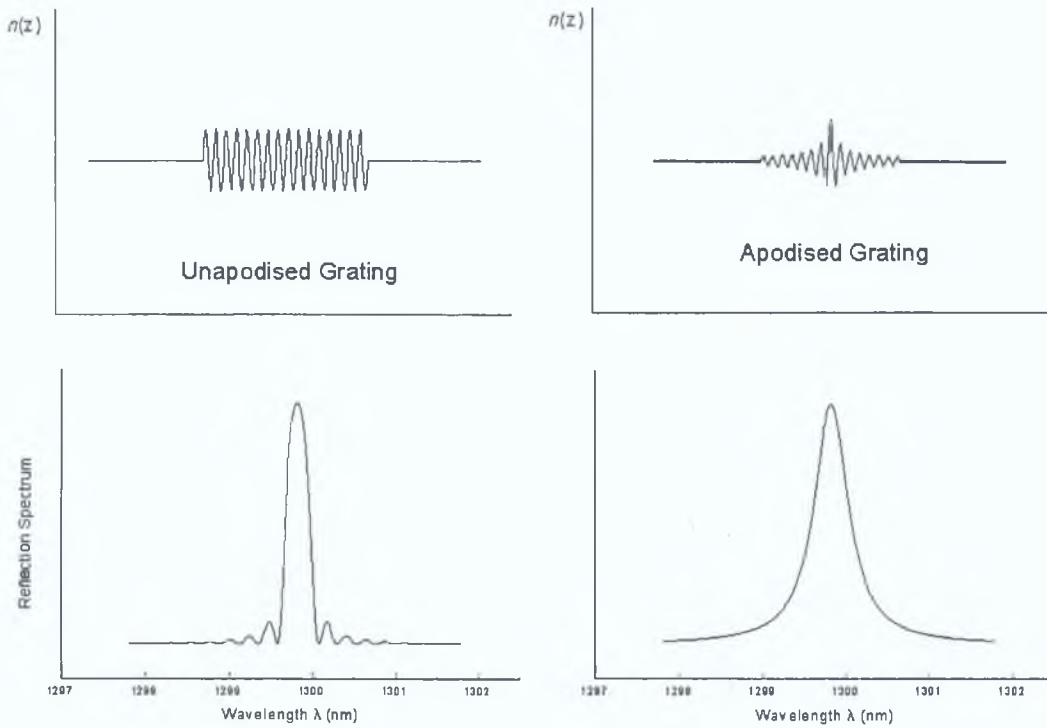


Figure 2.8

In the apodised grating the refractive index profile of figure 2.2 is modified by a z dependant amplitude

$$n^2(x, y, z) = \bar{n}^2(x, y) + \overline{\delta n_{eff}} \left\{ 1 + v(z) \cos \frac{2\pi}{\Lambda} [z + \phi(z)] \right\} \quad \text{E 2.41}$$

where $v(z)$ has a maximum at the grating center $z = -L/2$ and decreases gradually towards the grating edges of $z = -L$ and $z = 0$. Light incident on such a grating will encounter increasing refractive index changes until it reaches the grating centre and then continuously decreasing index modulation both superimposed on the sinusoidal periodicity

$$\cos \frac{2\pi}{\Lambda} [z + \phi(z)] \quad \text{E 2.42}$$

This is equivalent to the plane **diffraction grating** in which the transparency of the individual apertures is modified continuously from one edge to the other.

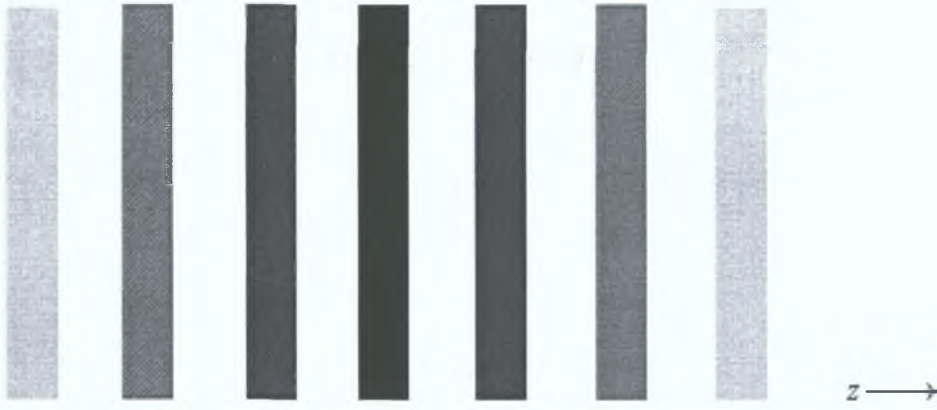


Figure 2.9

Because of this apodisation the coupling coefficient between a mode and its counter propagating equivalent (of the equal and opposite β) is now a function of position within the grating i.e. $\kappa = \kappa(z)$. The effect of apodisation is to redistribute energy in the diffraction pattern and reduce the intensity of the secondary diffraction maxima, in keeping with the literal translation of apodisation namely “removal of the feet”. The apodisation of the Bragg grating is achieved during the writing process of the index modulation profile by using the inherent intensity variation across the laser beam and or a varying transparency in the mask used to create the interference pattern which sets up the holographic grating. It was shown in [15] that side lobe suppression could be achieved with a quadratic apodisation and that the reflection spectrum of a grating reduces to the Fourier transform of the coupling coefficient $\kappa(z)$ for low reflectivities.

When a grating is written by a laser oscillating in the fundamental $TEM_{0,0}$ mode the intensity of the beam is Gaussian i.e. it falls exponentially with the square of the distance from the spot centre. With such a laser the apodisation $v(z)$ is of the form

$$v(z) = \exp\left[-\alpha\left(z + \frac{L}{2}\right)^2\right] \quad \text{E 2.43}$$

taking as before the origin at the distal end of the grating and it's centre to be at $z = -L/2$, where L is its length. In the refractive index profile $n^2(x, y, z)$ we have in this case

$$n^2(x, y, z) = \bar{n}^2(x, y) + \overline{\delta n_{eff}} \left\{ 1 + \exp\left[-\alpha(z + L/2)^2\right] \cos\left[\frac{2\pi z}{\Lambda} + \phi(z)\right] \right\} \quad \text{E 2.44}$$

and we can replace the term $\exp\left[-\alpha(z + L/2)^2\right]$ outside the $\cos(2\pi z/\Lambda)$ term with an imaginary phase term within the $\cos((2\pi z/\Lambda) + \phi)$ term. If we write the apodisation phase factor as $\phi_A(z)$ then (for Gaussian apodisation)

$$\phi_A(z) = i\alpha(z + L/2)^2 \quad \text{E 2.45}$$

and

$$\exp[i\phi_A(z)] = \exp[-\alpha(z + L/2)^2] \quad \text{E 2.46}$$

is exactly the Gaussian apodisation $v(z)$. Taking the coupling coefficient κ now to be constant

$$\kappa = \frac{\pi}{\lambda} \overline{\delta n_{eff}} \quad \text{E 2.47}$$

($v = 1$ in equation 2.31) and the detuning parameter $\hat{\sigma}$ now to be a complex number with real part

$$\hat{\sigma}_r(-L) = 2\pi n_{eff} \left\{ \frac{1}{\lambda} - \frac{1}{\lambda_0} \right\} + \frac{2\pi}{\lambda} \overline{\delta n_{eff}} - \frac{\dot{\phi}_r(-L)}{2}$$

and imaginary part

$$\hat{\sigma}_{im}(-L) = - \left[\frac{\dot{\phi}_{im}(z)}{2} \right]_{z=-L} = \frac{\alpha L}{2} \quad \text{E 2.48}$$

we can determine the spectral profile of the counter-propagating mode as [equation 2.32]

$$\frac{\sinh^2(\gamma_c L)}{\cosh^2(\gamma_c L) - (\hat{\sigma}_r + i\hat{\sigma}_{im})^2 / \kappa^2} \quad \text{E 2.49}$$

where γ_c is now a complex number given by

$$\gamma_c = \sqrt{\kappa^2 - \hat{\sigma}_r^2 + \hat{\sigma}_{im}^2 - 2i\hat{\sigma}_r\hat{\sigma}_{im}} \quad \text{E 2.50}$$

This function can be calculated for certain grating parameters $\overline{\delta n_{eff}}, n_{eff}, L$ and the intensity profile parameter α of the writing laser. Writing $\gamma_c L$ as $\gamma_c L = A + iB$ the back-reflected spectrum from the apodised grating is

$$|y|^2 = \frac{\sinh^2(A + iB)}{\cosh^2(A + iB) - [\hat{\sigma}_c^2 / \kappa^2]} \quad \text{E 2.51}$$

where $\hat{\sigma}_c = \hat{\sigma}_r + i\hat{\sigma}_{im}$ and

$$\begin{aligned} A &= \{(\kappa^2 - \hat{\sigma}_r^2 + \hat{\sigma}_{im}^2)^2 + 4\hat{\sigma}_r^2\hat{\sigma}_{im}^2\}^{1/4} L \cos(\theta/2) \\ B &= \{(\kappa^2 - \hat{\sigma}_r^2 + \hat{\sigma}_{im}^2)^2 + 4\hat{\sigma}_r^2\hat{\sigma}_{im}^2\}^{1/4} L \sin(\theta/2) \\ \tan \theta &= \frac{-2\hat{\sigma}_r\hat{\sigma}_{im}}{\kappa^2 - \hat{\sigma}_r^2 + \hat{\sigma}_{im}^2} \end{aligned} \quad \text{E 2.52}$$

In evaluating equation 2.51 the expression in Appendix A for hyperbolic sine and cosine functions given are used. In calculating θ in equation 2.52 care must be taken to prevent the introduction of arbitrary phase changes of $\pm \pi$ where $\kappa^2 - \hat{\sigma}_r^2 + \hat{\sigma}_{im}^2$ or $\hat{\sigma}_r$ changes sign at particular wavelengths. A program to evaluate the spectrum was written in FORTRAN (appendix C, program 5) and we are grateful to Mosnier and Cafolla [17] for assistance in its successful execution.

Using the following parameters

$$n_{eff} = 1.45, \overline{\delta n_{eff}} = 2 \times 10^{-4}, \lambda_D = 1300nm, L = 2mm$$

the spectral shape of the reflection spectrum as predicted by the model was calculated and normalised with respect to the peak height, for various values of the Gaussian apodisation function α ,

- (i) $\alpha = 0$ no apodisation
- (ii) $\alpha = 1 \times 10^3 m^{-2}$
- (iii) $\alpha = 5 \times 10^5 m^{-2}$
- (iv) $\alpha = 1 \times 10^6 m^{-2}$

the results are presented in figure 2.4,

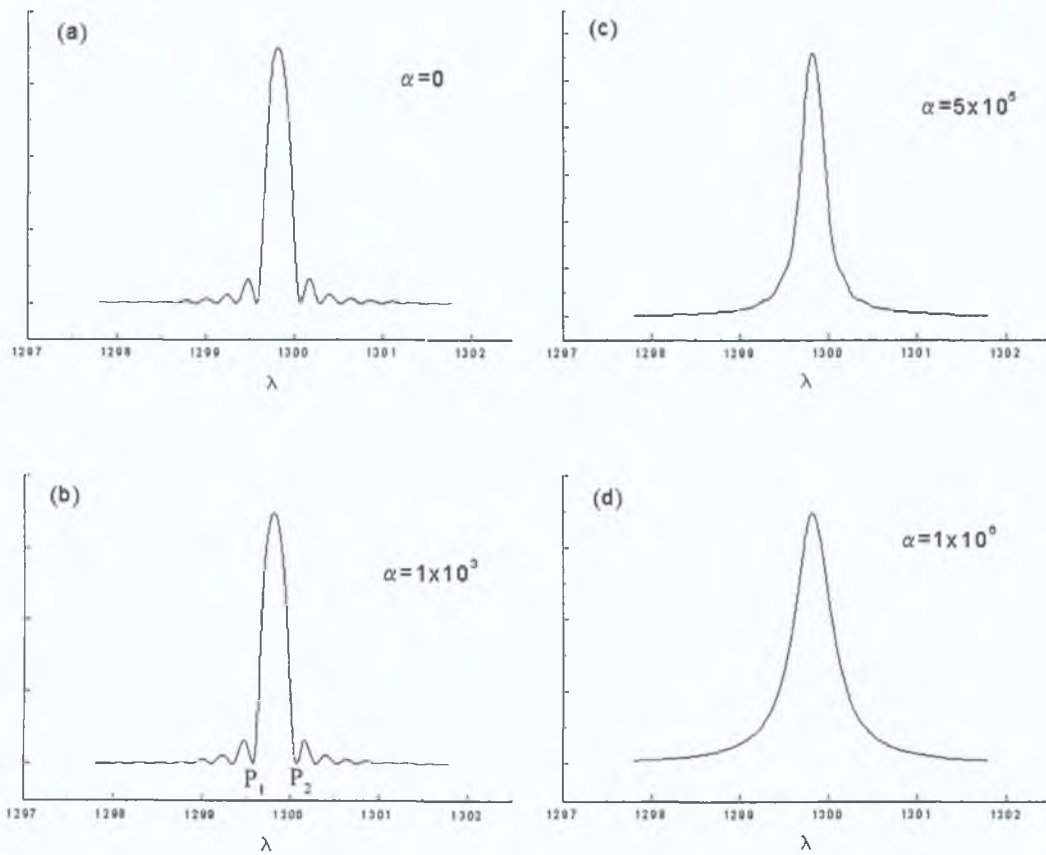


Figure 2.10

$$\lambda_0 = \frac{\lambda_D \left\{ 1 + \overline{\delta n_{eff}} / n_{eff} \right\}}{1 + \left(\lambda_D / 4\pi n_{eff} \right) \left\{ \hat{\phi}_r(-L) + \hat{\phi}_{im}(-L) \right\}} \quad \text{E 2.54}$$

This can be compared to λ_0 for the unapodised grating given by equation 2.34. It can be seen that apodisation as reflected in a non zero imaginary component of the grating phase $\phi(-L)$ gives rise to a very small shift in the central wavelength λ_0 .

The width of the spectral line is no longer easily defined as, for non zero values of B in equation 2.51, the numerator is no longer ever zero (or the denominator infinitely large). This is consistent with the spectrum shown in figure 2.4(b), but the first turning point P_1 and P_2 can be located from the condition that $\sinh(A + iB)$ is a minimum and $\cosh(A + iB)$ is a maximum. This occurs when A is a minimum or $\hat{\sigma}_r = \hat{\sigma}_{im}$ from equation 2.50. As $\hat{\sigma}_r = 0$ at $\lambda = \lambda_0$ the points P_1 and P_2 are separated by $2W$ where

$$W = \frac{\pi \overline{\delta n_{eff}} \lambda_0 + \left(\frac{\hat{\sigma}_{im}^2 \lambda_0^3}{\pi \overline{\delta n_{eff}}} \right) - \hat{\sigma}_{im} \lambda_0^2}{2\pi n_{eff} \left(1 + \frac{\overline{\delta n_{eff}}}{n_{eff}} \right)} \quad \text{E 2.55}$$

which, as expected, reduces to equation 2.38 in the limit $\hat{\sigma}_{im} = 0$ for an unapodised grating.

As apodisation is increased, by increasing the value of α , the shape of the spectrum approximates to a Gaussian shape where the term $(A + iB)$ is now dominated by the iB term and the argument $(A + iB)$ is small so that $\sinh(A + iB)$ can be approximated by $\exp(A + iB)$ and $\cosh(A + iB)$ by 1.0. Because of the $\hat{\sigma}_r^2$ and $\hat{\sigma}_{im}^2$ terms in $\gamma_c L$

the wavelength dependence of the spectrum line is symmetric in $(\lambda - \lambda_0)$ and is of the form

$$\exp\left[-c(\lambda - \lambda_0)^2\right] \quad \text{E 2.56}$$

,where c is a constant. Thus the line shape is Gaussian as seen earlier in figure 2.4(d).

Writing the line profile as

$$\exp\left[-(\lambda - \lambda_0)^2 / W_G^2\right] \quad \text{E 2.57}$$

W_G represents the half width at the $1/e$ height

and W_G is given by

$$W_G = \frac{\lambda_0}{2\pi n_{eff} \left(1 + \frac{\delta n_{eff}}{n_{eff}}\right)} \left\{ \pi \overline{\delta n_{eff}} \sqrt{1 - \left(\frac{\lambda_0 \alpha L}{2\pi \overline{\delta n_{eff}}}\right)^2} + \frac{\lambda_0 \phi(-L)}{2} \right\} \quad \text{E 2.58}$$

or

$$W_g = \frac{\lambda_0}{2\pi n_{eff} \left(1 + \frac{\delta n_{eff}}{n_{eff}}\right)} \left\{ \pi \overline{\delta n_{eff}} \sqrt{1 - \left(\frac{\alpha L^2 / 2}{\kappa_0 L}\right)^2} + \frac{\lambda_0 \phi(-L)}{2} \right\} \quad \text{E 2.59}$$

where

$$\kappa_0 L = \left(\frac{\pi \overline{\delta n_{eff}}}{\lambda_0} \right) L$$

As before if apodisation is weak ($\alpha \rightarrow 0$) W_G reduces to

$$\frac{\lambda_0 \overline{\delta n_{eff}}}{n_{eff} \left(1 + \frac{\overline{\delta n_{eff}}}{n_{eff}} \right)}$$

which is consistent with equation 2.38 in which the fringe visibility is take as $v = 1.0$.

For very strong apodisation i.e. $\alpha L^2/2 \gg \kappa_0 L$ equation 2.59 shows that the linewidth is no longer dependant on $\overline{\delta n_{eff}}$, the refractive index modulation

$$W_G \cong \frac{\alpha L \lambda_0^2}{4\pi n_{eff}} \quad \text{E 2.60}$$

(for $\overline{\delta n_{eff}}/n_{eff} \ll 1$), and in this limit the peak reflectivity ρ^2 can be shown for

$\alpha L^2/2 \gg \kappa_0 L$ to be

$$\rho^2 \approx \tanh^2 \left(\alpha L^2 / 2 \right) \quad \text{E 2.61}$$

2.5 Factors which affect the values of λ_0 and W , the central wavelength and linewidth of the reflection spectrum

We have seen in equation 2.54 and 2.59 respectively how the grating properties

n_{eff} , $\overline{\delta n_{eff}}$, $\lambda_D (= 2n_{eff} \Lambda)$, and $\phi(-L)$ affect both λ_0 the central wavelength and W

the linewidth of the spectral line back reflected from the Bragg grating. Parameters which affect any of these properties will result in modifications to both λ_0 and W as well. As the peak wavelength λ_0 is, for both the simple unapodised grating and the Gaussian apodised gratings directly proportional to $\lambda_D (= 2n_{eff} \Lambda)$ any factors which affect the magnitude of n_{eff} or Λ will lead to a shift in the central wavelength of the grating. Likewise the linewidth for both unapodised and apodised gratings depend on

λ_D , and through it are both n_{eff} and Λ . Strain, strain gradient and temperature affect respectively Λ , $\phi(-L)$ and n_{eff} and we will examine each effect in turn.

2.5.1 Temperature

As λ_0 is directly proportional to the product of n_{eff} and Λ we can write

$$\ln \lambda_0 = \ln n_{eff} + \ln \Lambda + \text{constant}$$

or differentiating

$$\frac{1}{\lambda_0} \left(\frac{\partial \lambda_0}{\partial T} \right) = \frac{1}{n_{eff}} \left(\frac{\partial n}{\partial T} \right) + \frac{1}{\Lambda} \left(\frac{\partial \Lambda}{\partial T} \right) = (\xi + \alpha_T) \quad \text{E 2.62}$$

where ξ is $\frac{1}{n_{eff}} \left(\frac{\partial n}{\partial T} \right)$ is the thermooptic coefficient and α_T is $\frac{1}{\Lambda} \left(\frac{\partial \Lambda}{\partial T} \right)$ is the

coefficient of linear expansion. ξ has a value of 8.3×10^{-6} [21] for germania doped

silica and α_T has a value of 5.5×10^{-7} [21] so that the temperature coefficient of λ for

a Bragg grating is

$$\frac{1}{\lambda} \left(\frac{\partial \lambda}{\partial T} \right) = 8.85 \times 10^{-6} \text{ } ^\circ\text{C}^{-1}$$

which gives $(\partial \lambda / \partial T) \approx 11.5 \text{ pm}/^\circ\text{C}$ at $\lambda = 1300 \text{ nm}$ or $\approx 13.3 \text{ pm}/^\circ\text{C}$ at $\lambda = 1500 \text{ nm}$.

The linewidth depends upon the product of the terms $\overline{\delta n_{eff}}$ and Λ so that

$$\frac{1}{W} \left(\frac{\partial W}{\partial T} \right) = \frac{\partial}{\overline{\delta n_{eff}}} \left(\frac{\partial \overline{\delta n_{eff}}}{\partial T} \right) + \frac{1}{\Lambda} \left(\frac{\partial \Lambda}{\partial T} \right) = (\xi + \alpha_T) \quad \text{E 2.63}$$

as before. This leads to a linewidth temperature coefficient $\frac{1}{W} \left(\frac{\partial W}{\partial T} \right)$ which is equal

to that of the wavelength dependence figures given above.

2.5.2 Strain

A strain applied to the Bragg grating will lead to a change in the periodicity Λ of the rulings and also to a variation in the refractive index n_{eff} of the glass of the fibre core.

A strain of ε increases Λ to $\Lambda(1 + \varepsilon)$ and as λ_0 depends upon the product of Λ and n_{eff} we get

$$\frac{1}{\lambda} \left(\frac{\partial \lambda}{\partial \varepsilon} \right) = \frac{1}{\Lambda} \left(\frac{\partial \Lambda}{\partial \varepsilon} \right) + \frac{1}{n_{eff}} \left(\frac{\partial n_{eff}}{\partial \varepsilon} \right) \quad \text{E 2.64}$$

Term one in the equation has a value of unity while term two, which represents the photoelastic induced change in the refractive index of the glass, is given by the effective photoelastic constant p_e as

$$p_e = \left(n^2 / 2 \right) [p_{12} - \nu(p_{11} + p_{12})] \quad \text{E 2.65}$$

p_{11} and p_{12} are the Pockel's piezo coefficients of the stress-optic tensor, ν is

Poisson's ratio and n is the index of refraction of the glass of the fibre core. Using values quoted in [13] p_e is given as 0.22 so that

$$\frac{1}{\lambda} \left(\frac{\partial \lambda}{\partial \varepsilon} \right) = 1 - p_e = 0.78 \quad \text{E 2.66}$$

We get then

$$\begin{aligned} \frac{\partial \lambda}{\partial \varepsilon} &= 1.014 \text{ pm} / \mu\varepsilon^* \quad @ \lambda = 1300 \text{ nm} \\ &= 1.200 \text{ pm} / \mu\varepsilon \quad @ \lambda = 1550 \text{ nm} \end{aligned} \quad \text{E 2.67}$$

as quoted in [24],[25] and [26].

As the linewidth (W_G) is proportional to the product of Λ and $\overline{\delta n_{eff}}$ we can write

$$\begin{aligned}
\frac{1}{W} \left(\frac{\partial W}{\partial \varepsilon} \right) &= \frac{1}{\Lambda} \left(\frac{\partial \Lambda}{\partial \varepsilon} \right) + \frac{1}{\delta n_{eff}} \left(\frac{\partial \delta n_{eff}}{\partial \varepsilon} \right) \\
&= \frac{1}{\Lambda} \left(\frac{\partial \Lambda}{\partial \varepsilon} \right) + \frac{1}{n_{eff}} \left(\frac{\partial n_{eff}}{\partial \varepsilon} \right) \\
&= (1 - p_e) = 0.78
\end{aligned}
\tag{E 2.68}$$

as derived earlier. Taking a nominal linewidth of $1nm$ the sensitivity of the linewidth to strain is then

$$\begin{aligned}
\frac{\partial W}{\partial \varepsilon} &= 0.78 \times 10^{-15} \text{ meters per microstrain} \\
&= 7.8 \times 10^{-4} \text{ pm per } \mu\varepsilon
\end{aligned}$$

This is a factor of over 1500 lower in sensitivity than $\partial \lambda / \partial \varepsilon$.

With a single measurement of a shift in Bragg wavelength ($\Delta \lambda$) it is not possible to decouple the temperature and strain dependant effects as

$$\Delta \lambda = \left(\frac{\partial \lambda}{\partial T} \right) (\Delta T) + \left(\frac{\partial \lambda}{\partial \varepsilon} \right) (\Delta \varepsilon)
\tag{E 2.69}$$

with the temperature effect typically of the order of $10 \text{ pm}/^\circ\text{C}$ and the strain effect of the order of $1 \text{ pm} / \mu\varepsilon$. This is analogous to the measurement of strain using a wire or semiconductor strain gauge where changes in ambient temperature affect the resistance of the gauge in tandem with changes in strain. In the case of wire/semiconductor strain gauges the effect of changes in ambient temperature may be removed by having the strain gauges in pairs and wired into a Wheatstone bridge circuit. One gauge monitors temperature variations only while the other (the active one) responds to both temperature and strain. Being wired in a potential divider

* $1 \mu\varepsilon$ or 1 micron strain is 10^{-6}

configuration the bridge output is then dependant on the strain effect only, the temperature effect being equal in both gauges.

Temperature and strain can be decoupled using either two Bragg gratings, one sensitive to temperature alone (the reference grating), the other to temperature and strain (the active grating) - the method used in [27] and [28] – or by using two superimposed fibre Bragg gratings of different Bragg wavelengths ($\lambda_{B_1}, \lambda_{B_2}$) as reported in [29].

2.5.3 Strain Gradient

When a Bragg grating is chirped i.e. when the ruling periodicity Λ of the refractive index modulation varies across the length of the grating then each section of the grating contributes a local Bragg wavelength $\lambda_B(z)$ given by

$$\lambda_B(z) = 2n_{eff}(z)\Lambda(z) \tag{E 2.70}$$

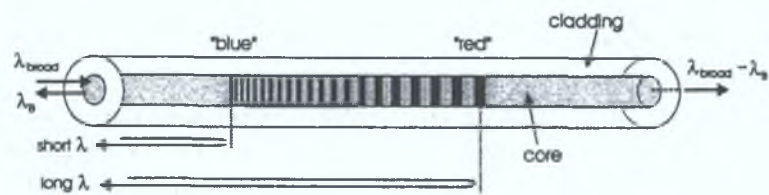


Figure 2.11

If the grating is exposed to a non-uniform strain (or temperature gradient) different sections of the grating contribute different wavelengths to the reflection spectrum and broaden the spectrum while decreasing the peak reflectivity. For a uniform strain gradient $g(= \partial \epsilon / \partial z)$ the periodicity Λ of the rulings becomes

$$\Lambda(1 + gz) \tag{E 2.71}$$

and the phase factor in the index modulation $\cos\left\{\frac{2\pi z}{\Lambda} + \phi(z)\right\}$ becomes

$$\cos\left\{\frac{2\pi z}{\Lambda(1+gz)} + \phi(z)\right\} \quad \text{E 2.72}$$

Using the binomial expansion for $gz \ll 1$ the index modulation is then

$$\cos\left\{\frac{2\pi z}{\Lambda} - \frac{2\pi gz^2}{\Lambda}\right\} \quad \text{E 2.73}$$

i.e. the strain gradient has introduced a phase factor of

$$\phi_g(z) = -\frac{2\pi gz^2}{\Lambda} \quad \text{E 2.74}$$

Since the width of the reflection spectrum depends on $\dot{\phi}(-L)/2$, as shown in equation 2.59 the linewidth carries a term of

$$\frac{\dot{\phi}(-L)}{2} = +\frac{2\pi gL}{\Lambda} \quad \text{E 2.75}$$

The linewidth of the back reflected light from the grating will therefore be an indication of both the magnitude and direction of the strain gradient g over the length of the Bragg grating. Using equation 2.75 in equation 2.59 we see that the sensitivity of the linewidth to the strain gradient g is

$$\begin{aligned} \frac{\partial W}{\partial g} &= \frac{\lambda_0}{2\pi n_{eff}} \frac{\partial [\lambda_0 \dot{\phi}(-L)/2]}{\partial g} \\ &\approx 2\lambda_0 L \end{aligned} \quad \text{E 2.76}$$

When the grating is exposed to a strain gradient the imaginary phase factor $\phi_A(z)$ - due to apodisation – changes from

$$i\alpha(z + L/2)^2 \quad \text{to} \quad i\alpha[z(1 + gz) + L/2]^2$$

And the linewidth W_G becomes

$$\begin{aligned} W_G &= \frac{\lambda_B}{2\pi n_{eff}} \left\{ \pi \overline{\delta n_{eff}} + \frac{2\pi g L \lambda_B}{\lambda} + \frac{\alpha L}{2} (1 + gL - 2g^2 L^2) \right\} \\ &= \lambda_B \left(\frac{\overline{\delta n_{eff}}}{2n_{eff}} \right) - 2g \lambda_B L \left\{ 1 + \frac{\alpha L^2}{4\pi n_{eff}} \right\} + g^2 \left(\frac{\lambda_B L^4 \alpha}{2\pi n_{eff}} \right) \end{aligned} \quad \text{E 2.77}$$

or

$$W_G = A - B_1 g + B_2 g^2 \quad \text{E 2.78}$$

Thus there are three contributions to the linewidth:

1. A constant term $\lambda_B (\overline{\delta n_{eff}}) / 2n_{eff}$
2. A term linear in g , due to the distribution of $\Lambda(z)$ along the grating, and a contribution due to the modification in the apodisation profile caused by the strain gradient
3. A term quadratic in g , due to the modification of the apodisation profile

2.6 Simulation techniques

The simplest method of Bragg grating simulation is the straightforward numerical integration of the coupled-mode equations. While this method is capable of simulating the transfer function accurately, it is computationally slow. In the following section two computational methods are described which allow a Bragg grating to be

simulated. The first, the transfer matrix method [29], is fast and accurate for both strong and weak gratings with or without apodisation. The second, Rouard's Method [23], [31], is slow as it is still computationally heavy but it has the main advantage that it allows refractive index profiles of many designs to be modeled.

2.6.1 Transfer matrix method

A solution for a grating of length L , with a coupling coefficient $\kappa(z)$ and grating spacing $\Lambda(z)$ is required. In the transfer matrix method, the coupled mode equations [Equations 2.22] are used to generate the output fields of a small section (δL) of the grating for which the three parameters are constant. These results are then used as the inputs to the adjacent sections of the grating. A matrix which describes the whole system may be written as

$$\begin{bmatrix} R(-\delta L/2) \\ S(-\delta L/2) \end{bmatrix} = [T^1] \begin{bmatrix} R(\delta L/2) \\ S(\delta L/2) \end{bmatrix} \quad \text{E 2.79}$$

For a reflection grating the input field amplitude is normalised to unity and the output of the grating is zero, as there is no perturbation beyond the end of the Bragg grating.

By applying these boundary conditions we arrive at

$$\begin{bmatrix} 1 \\ S(-\delta L/2) \end{bmatrix} = \begin{bmatrix} T_{11} & T_{12} \\ T_{21} & T_{22} \end{bmatrix} \begin{bmatrix} R(\delta L/2) \\ 0 \end{bmatrix} \quad \text{E 2.80}$$

It can be seen from this that the transmission and reflection amplitudes are given respectively by

$$R(\delta L/2) = \frac{1}{T_{11}}$$

$$S(-\delta L/2) = \frac{T_{21}}{T_{11}}$$

Now there are new fields which can be transformed into a second transfer matrix, T^2 , and so on until the full grating has been processed. This gives us the transfer matrix as follows

$$\begin{bmatrix} R(-\delta L/2) \\ S(-\delta L/2) \end{bmatrix} = [T] \begin{bmatrix} R(\delta L/2) \\ S(\delta L/2) \end{bmatrix}$$

where the matrix $[T]$ is given by,

$$[T] = \prod_{j=1}^N [T^j] \quad \text{E 2.81}$$

From the coupled mode equations the transfer matrix elements may be determined and a solution may be produced.

2.6.2 Rouards's method

This method consists of breaking the Bragg grating into a set of layers along the length of the grating. Each layer is treated as an interface with a complex reflectivity, which include a phase change through the layer. To model the grating accurately the refractive index profile is broken up into sections which are smaller than the grating period Λ . A recursive technique is then applied to calculate the reflectivity for each set of layers which make up a single grating period. Thus, the problem is reduced to calculating the amplitude of the reflectivity for each single period. This method is useful for modeling gratings which have complex refractive index modulation profiles. The main drawback of this system is however that computational errors can become significant at large numbers of thin film layers. The basic analysis is similar to that used the transfer matrix method but the reflectivity is simply calculated from the difference in the refractive index between two adjacent layers.

2.7 Conclusions

We have seen, using the coupled mode theory approach, that fibre Bragg gratings can be described fully. It has been shown that for a simple, purely sinusoidal grating the reflection spectrum can be described as in equation 2.30, with a maximum intensity given by equation 2.36 and width given by equation 2.40. A detailed discussion of apodisation has been given, with special attention being given to the apodisation generated by the use of a laser with a Gaussian beam profile in the grating manufacture. This apodisation has been shown to “remove the side lobes” from the grating reflection spectrum. The apodisation of the grating causes the reflection spectrum to be broadened as shown in figure 2.4. A full description of the effect of temperature, strain and strain gradient has been given and numerical evaluations of each of these effects have been made. Both temperature and strain have been shown to cause a shift in the central wavelength of the Bragg grating (λ_0), while the strain gradient has been shown to alter the linewidth of the reflected spectrum. Two of the most common simulation techniques have been described, although neither of these was used, as a full simulation using the coupled mode equations was done. Both of these techniques, transfer matrix and Rouard’s method, have differing advantages which make them useful in simulating many different types of Bragg gratings.

2.8 References

- [1] Snyder A.W. and Love J.D., “*Optical Waveguide Theory*”, Chapman and Hall (1983)
- [2] Gradshteyn I.S., Ryzhik I.M. and Jeffrey A. (ed), “*Tables of Integrals, series and products*”, Academic Press N.Y. (1994)
- [3] Hecht E., “*Optics*”, Addison-Wesley Publications Co. Mass. U.S.A. (1987)
- [4] Hook J.R. and Hall H.E., “*Solid State Physics – Second Ed.*”, Wiley and Sons (1991)
- [5] Fowles G.R., “*Introduction to Modern Optics*”, Dover Press N.Y. (1989)
- [6] Yariv A., “Coupled Mode Theory for guided wave optics”, I.E.E.E. Journal Quantum Electronics, QE-9 No.9 (1973) Pg919-933
- [7] Erdogan T., “Fibre Grating Spectra”, Journal of Lightwave Technology, Vol 15 (No. 8) Pg1277-1294
- [8] Kogelnik H., “*Theory of optical waveguides*”, Guided wave optoelectronics, T. Tamir Ed., NY Springer-Verlay (1990)
- [9] Ghatak A and Thyagarajan, “*Introduction to fibre optics*”, Cambridge University Press (1998), Appendix E, Equations E20 and E21
- [10] Gradshteyn I.S., Rhzhik I.M. and Jeffrey A (Ed.), “*Tables of integrals, series and products*”, Academic Press N.Y. (1994), Section 16.515
- [11] Zwillinger D., “*Handbook of Differential Equations*”, Academic Press, San Diego (1989), II A.75

- [12] Polyanin A.D. and Zaitsev V.F., “*Handbook of exact solutions for ordinary differential equations*”, CRC Press (1995), Pg132
- [13] Rao Y.J., “In-fibre Bragg grating sensors”, *Measurement Science Technology*, Vol 8 Pg335-375 (1997)
- [14] Haus H.A. “*Waves and fields in optoelectronics*”, Prentice-Hall New Jersey (1984), Section 8.1 Equation 8.18
- [15] Kogelnik H., *Bell System Technology Journal*, Vol 55 Pg109-126 (1976)
- [16] Abramowitz M. and Stegun I.A. (eds), “*Handbook of Mathematical Functions*”, National Bureau of Standards (1968), Eqn. 4.5.49 and 4.5.50
- [17] Mosnier J.P. and Cafolla A.A., School of Physical Sciences, Dublin City University – Private communications
- [18] Cross P.S. and Kogelnik H., “Sidelobe suppression in corrugated waveguide filters”, *Optics Letters* Vol 1 No. 1 (1977) Pg43-45
- [19] Hecht E., “*Optics*”, Addison-Wesley Publ. Co. (1974) pg492
- [20] Takahashi S. and Shibata S., “Thermal variation of attenuation for optical fibres”, *Journal of non-crystalline solids*, Vol 30 (1979) Pg359-370
- [21] Van Vlack L.H., “*Elements of Materials Science and Engineering*”, Addison-Wesley (1985) Appendix C
- [22] Guenther R., “*Modern Optics*”, Wiley and Sons, N.Y. (1990), Table 14.7
- [23] Weller-Brophy L.A. and Hall D.G., “Analysis of waveguide gratings”, *Journal Optical Society of America* Vol 4 No.1, Pg60-65 (1987)

- [24] Cruz J.L., Dong L., Barcelos S. and Reekie L. "In-fibre Bragg gratings with various chirp profiles made in etched tapers", *Applied Optics*, Vol 35 No. 34, Pg6781-6788 (1996)
- [25] Kersey A.D., Davis M.G., Patrick H.J., LeBlanc M., Koo K.P., Askins C.G., Putman M.A. and Friebele E.J., "Fibre Grating sensors", *Journal of Lightwave Technology*, Vol 15 No. 8 (Aug 1997) Pg1442-1462
- [26] Morley W.W., Meltz G. and Welss J.M., "Evaluation of a fibre Bragg grating hydrostatic pressure sensor", *Proceedings of 8th International Conference on Optical Fibre Sensors*, (CA, U.S.A. (1992) post deadline paper)
- [27] Xu M.G., Archambault J.L, Reeke L and Dakin J.P., "Thermally compensated bending guage using surface mounted fibre gratings", *International Journal of Optoelectronics*, Vol 9 Pg281-283 (1994)
- [28] Xu M.G., Archambault J.L, Reeke L and Dakin J.P., "Discrimination between strain and temperature effects using dual wavelength fibre grating sensors", *Electron Letters*, Vol 30 Pg1085-1087 (1994)
- [29] Yamada M. and Sakuda K., "Analysis of almost periodic distributed feedback slab waveguides via a fundamental matrix approach", *Applied Optics* 26(16), Pg3474-3478 (1987)
- [30] Rouard M.P., "Etudes des proprietes optiques des lames metalliques tres minces", *Annal. Physic II* Vol 7 No. 20 (1937)

Chapter 3 Bragg Grating Fabrication

3.1 Introduction

To create a Bragg grating in a fibre waveguide requires a periodic index modulation to be impressed along the core axis of the fibre. This can be achieved by a variety of methods. In this chapter the index modulation mechanism will be discussed together with the various interferometric techniques which have been used to “write” fibre Bragg gratings.

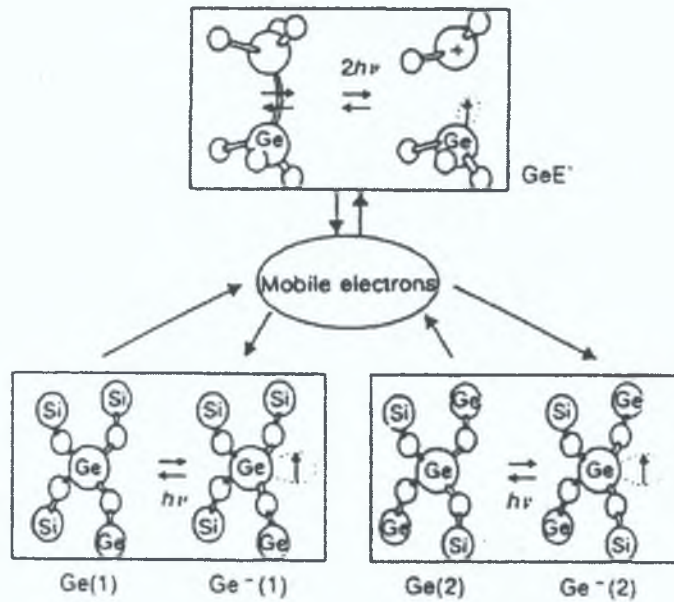
3.2 The Mechanism of refractive index modulation.

Optical fibres are fabricated from glasses or plastics with the inner core region made of a material with slightly higher refractive index n_1 than the surrounding cladding material (of index n_2). By doping with low concentrations of ‘impurities’ the refractive index differential between the core material and the cladding is created in the fibre preform and transferred to the fibre on drawing out. Many optical fibres are made from fused silica (SiO_2), with the core doped to increase the refractive index above that of the cladding. Various dopants can be used with germania (GeO_2) being by far the most common. Doping levels of a few percent by weight are typical. When germania-silicate glasses are exposed to UV light in the 240-260 nm range, they are observed to develop refractive index changes. This process which is related to the breaking of the Si-Ge bonds in the glass, by the high energy UV photons, results in the freeing of electrons which can be trapped at germanium sites to form negatively charged colour centres. These colour centres cause a change in the absorption spectrum and this can be related to a change in the real component of the

refractive index of the glass by the Kramer-Kronig relationship [1]. This equation relates the refractive index $n(\lambda)$ to the absorption coefficient $\alpha(\lambda)$ through integrals, over all frequencies of the real and imaginary part of the electrical susceptibility of the medium $\chi(\lambda)$.

During fibre fabrication, by chemical vapour deposition, bonds such as Si-Ge; Si-Ge and Ge-Ge may be formed; normally there are “bridging oxygens”. Photon absorption near 245nm now causes breakage of these bonds and should (according to the Kramer–Kronig relationship) cause a reduction in the refractive index of the glass. However a positive change of refractive index increase is observed. Atkins et al [9] have reconciled this problem by showing that the bleaching of the 245nm band is accompanied by the appearance of a strong absorption band below 200nm.

Two other mechanisms to explain the change in refractive index with UV photon absorption at 245nm have been proposed. In one, the so called “Dipole Model” the fabrication of a dipole between the negatively charged colour centre and the $\text{Ge} \equiv \text{Si}^+$ bond is suggested. The E field of the dipole is then conceived to give rise to the refractive index change via the electroptical effect. The third model, the so called “Compaction Model” envisages the bond breakages by the UV absorption resulting in a compression of the glass structure and a resulting increase in glass density and thereby the refractive index.



Breakage of Ge-Si bond and movement of electrons

Figure 3.1 Inoue et al (1995)

Two types of glass modification by UV photon absorption have been identified. Type I modification which it is thought to be related to colour centre sensitivity and Type II which is attributed to actual damage to the glass. The latter is more stable at high temperatures.

The mechanism of Type II damage, discovered by the Optoelectrical Research Centre of the University of Southampton U.K., where the core is precisely damaged by a single pulse of the order of 40 mJ of laser light, is not fully understood. It is possible that photon absorption at 248 nm causes excitation of electrons into the conduction band of silica where, in the presence of UV, they seed the formation of a free-electron plasma. This then produces a sudden increase in UV absorption and permanent damage to the glass.

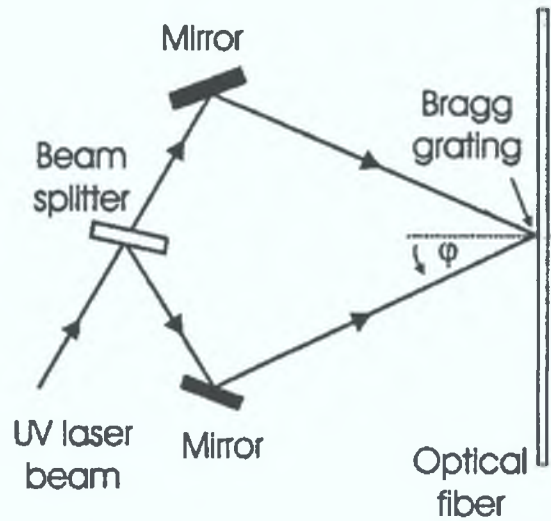
Lemaire et al (1993) have sensitised fibres to the photo refractive effect by the so called “hydrogen loading”. This involves diffusing the hydrogen molecules into the fibres core at low temperatures and high pressure. The presence of hydrogen increases the concentration of bleachable germanium oxygen deficiency. The UV induced refractive index can reach 1×10^{-2} with germania doped singlemode fibres, with 6% by weight Ge-O₂ after H₂ loading at 200 atmospheres of pressure at room temperature for 1 week.

3.3 Standing wave Grating (The two beam interferometer)

The first fibre grating was written by Hill et al in 1978 [4] using an Argon-Ion laser beam ($\lambda = 488$ nm blue, and $\lambda = 514.5$ nm green) launched into a fibre core. Fresnel reflection (typically ~4%) from the open distal end created a standing wave pattern of $\lambda/2$ antinode to antinode spacing. The high intensity laser standing wave pattern - modulated spatially along the fibre axis – created a refractive index modulation by a Type I mechanism. Because such gratings can be formed with only one periodicity ($\lambda/2$ of the laser light used in fabrication) and are also photosensitive, they can be bleached using visible light.

3.4 Holographic Gratings.

In 1989 Meltz et al [5] of United Technologies Conn. USA suggested that gratings could be written in fibres by exposing the fibre core from the side by two interfering coherent UV beams through the cladding glass. A frequency doubled Argon ion laser was used to



produce a 244nm source. The beam was split in amplitude by a beam splitter - as shown - to create an interference pattern on the fibre using cylindrical lenses.

This combination of two collimated beams of monochromatic light produces “Cosine² fringes” along the fibre as in the formation of a holographic grating. The spacing of the “rulings” (Λ) of the grating formed obeys.

$$2\Lambda \sin\left(\frac{\phi}{2}\right) = \lambda \quad \text{E 3.1}$$

where λ is the wavelength of the light used. Ruling spacing Λ may be selected by a suitable choice of ϕ , the angle between the two interfering beams.

The lateral extent of the grating written in the fibre depends upon the coherence properties of the laser used. While coherence lengths of 25 mm are achievable with some excimer lasers, transverse coherence is still quite poor and gratings of at most a few mm in length can be achieved by this method. [It can be seen from Equation 1.11 that short gratings have a low reflectivity at the Bragg wavelength]. For grating writing which involves multiple laser shots the interferometer work surface must be

stabilised against vibration and air currents over the exposure time of up to a few minutes. Consistent and repeatable grating writing with this holographic technique is difficult to achieve.

3.5 Phase Mask Grating Writing

The manufacture of phase masks, diffractive optic elements with a sinusoidal transparency over each aperture together with a π phase changing feature impressed over half the field of each aperture, has greatly simplified the manufacture of Bragg gratings. These masks are made of high quality fused silica by photolithographic means. The grating surface relief, over half of each mask aperture, is designed so that,

$$\frac{2\pi}{\lambda}(n-1)d = \pi \quad \text{E 3.2}$$

as shown originally by Hill et al (1993) [6]. Here λ is the wavelength of the monochromatic light (often a KrF excimer laser of 248 nm wavelength) used to illuminate the mask and d is the thickness of the silica (of refractive index n). When the transparency function of the mask is given by

$$-\cos\left(\frac{2\pi x}{a^*}\right) \quad \text{for } -a^*/2 < x < 0$$

and

$$+\cos\left(\frac{2\pi x}{a^*}\right) \quad \text{for } 0 < x < +a^*/2 \quad \text{E 3.3}$$

(the + and – signs displaying the phase change induced over the two halves of the masks aperture and the $\cos(2\pi x/a^*)$ showing the sinusoidal variation of transparency with location x within the aperture) it can be shown that the Fraunhofer diffraction

pattern, obtained by taking the Fourier transform of the aperture function in equation 3.3 has

- No zero order diffractive pattern
- First order $n = +1$ and $n = -1$ diffraction
- No higher order structure

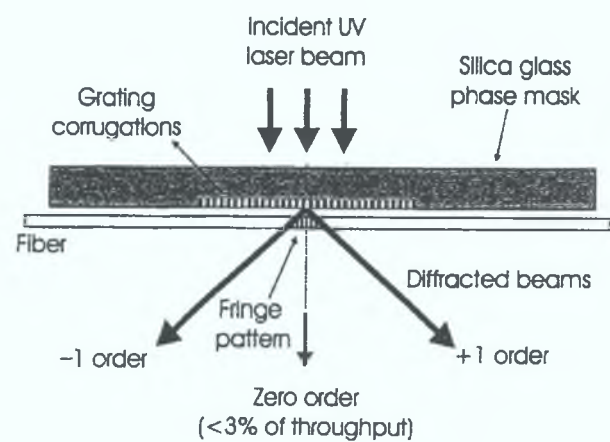


Figure 3.2

The zero order suppression, brought about by the interference of the two straight-through ($\theta = 0$) beams, one of which is π out of phase with the other, is a result of the phase change introduced in the mask. Suppression to transmission levels of $\sim 2\%$ of the incident intensity in zero order have been achieved. The effect of zero order suppression is to diffract substantial amounts of optical power into each of the two

first order diffraction beams. Power levels of 35% in each order have been achieved. The real effect of the phase mask is therefore to create two high intensity coherent beams as shown above.

The interference pattern created by these two beams, at an angle of 2θ to one another is given by $a^* \sin \theta = \lambda$ (since $n = \pm 1$) creating a “cos²” type interference fringe pattern on the fibre with a periodicity Λ given by

$$2\Lambda \sin \theta = \lambda \quad \text{E 3.4}$$

(using equation 3.1 with $\phi = 2\theta$) Equating equations 3.3 and 3.4 gives

$$a^* = 2\Lambda \quad \text{E 3.5}$$

i.e. the periodicity of the grating formed is half that of the phase mask (a) used to make it.

Since by equation 1.10

$$\lambda_{\text{Bragg}} = 2n_{\text{eff}} \Lambda \quad \text{E 3.6}$$

then

$$\lambda_{\text{Bragg}} = n_{\text{eff}} a^* \quad \text{E 3.7}$$

The spacing of the rulings of the phase mask (a^*) is the desired Bragg wavelength of the grating divided by the effective index of the fundamental mode in the fibre. The latter is typically 1.4 - 1.5 for silica fibre. Therefore to make a Bragg grating with a central wavelength of say 1550 nm (where silica has its minimum attenuation)

requires a phase mask of about 1000nm ($\sim 1 \mu\text{m}$) spacing or a Bragg grating periodicity Λ of about 500 nm.

It should be noted that the wavelength of the laser light used does not affect the periodicity impressed in the fibre core nor the Bragg wavelength of the grating created.

3.6 Type I and Type II Bragg gratings

Type I gratings are generated via photochromic effects (induced colour centre formation) with multiple UV laser pulses at energy densities clearly below the damage threshold of the fibre ($\sim 1 \text{ J} / \text{cm}^2$). Type II gratings are generated with energy densities close to the damage threshold of the fibre causing actually damage to the structure of the silica in the core of the fibre. There are a number of advantages of type II gratings over type I gratings and these are outlined below.

- Single laser pulse writing of type II gratings is possible
- Large index modulations are possible
- Type II gratings are stable at temperatures up to 800°C

The ability to produce a grating with a single pulse of a laser is of great importance as it allows gratings to be made during the drawing of the fibre.

3.7 Laser selection for writing fibre Bragg gratings

The most common laser used in the manufacture of fibre Bragg gratings is the KrF excimer laser. This is chosen because it operates at 248nm which fits into the absorption band of germanosilicate fibres. Excimer lasers are pulsed gas lasers. The

laser radiation is produced when a transient high voltage is discharged in a tube containing the KrF gas. Excimer lasers have short pulse durations ($\sim 10\text{-}50\text{ ns}$) and have high average powers ($\sim 150\text{ W}$). The profile of a typical excimer laser is shown below [8]. The beam profile has a distribution which is nearly Gaussian.

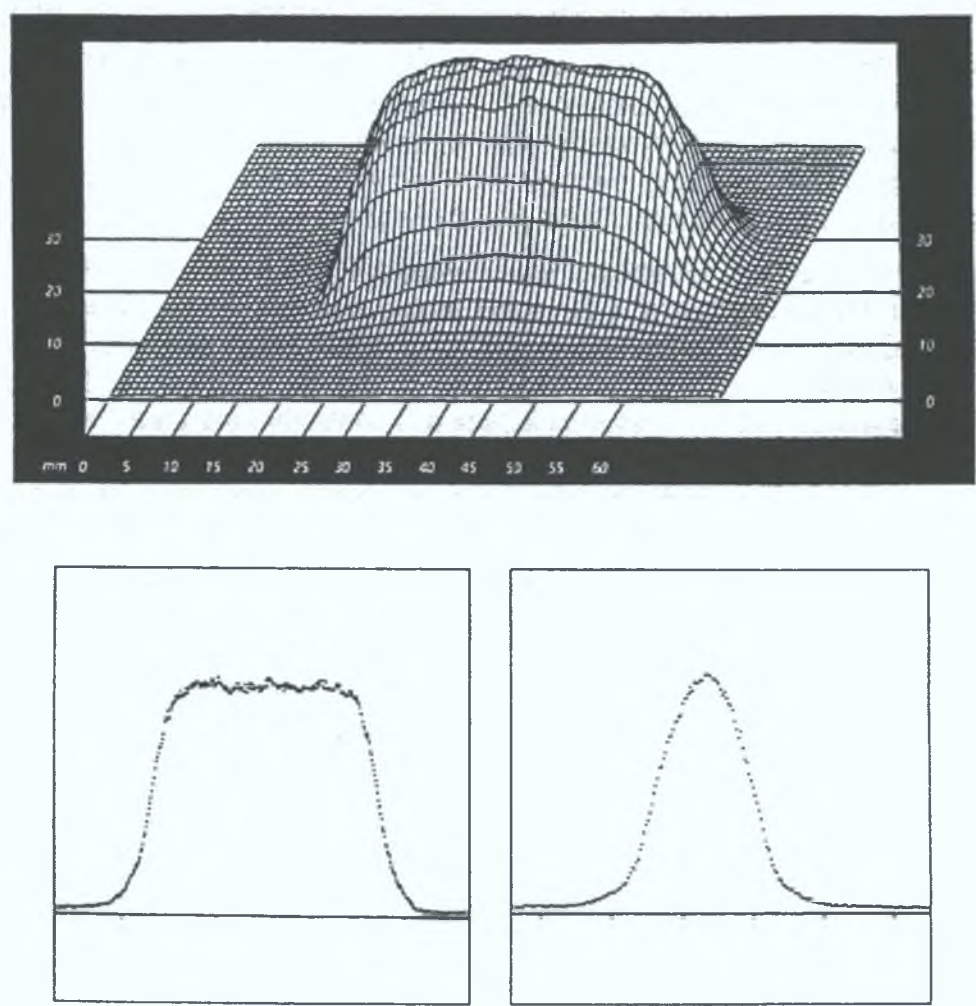


Figure 3.3 Excimer Laser profiles [8]

3.8 Conclusions

We have treated the fabrication of Bragg grating in fibres from a historical perspective beginning in 1978 with the standing wave grating and culminating with the present day use of phase masks. It has been seen that of the processes which may be employed to modulate the refractive index of the fibre, the generation of a type II grating is important if a long lasting and stable grating is to be made. KrF excimer

lasers have been seen to be most suitable for use in the 'writing' process due to their high output power and short pulse lengths.

3.9 References

- [1] Saleh B.E.A. and Teich M.E. "*Fundamentals of Photonics*" (Wiley + Sons N.Y. 1991) Eqn. 5.5.10 pg179.
- [2] Inoue A, Shigehana M, Ito M, Inai M, Hattori Y, Mizunami T., "Fabrication and application of fiber Bragg grating – A review", *Optoelectronics - Devices and Technology* Vol 10, No 1 pg119-130 (1995)
- [3] Lemaire P.J., Atkins R.M., Mirah V. and Reed W.A., "High-pressure H_2 loading as a technique for achieving ultrahigh UV photosensitivity and thermal sensitivity in GeO_2 doped optical fibers", *Electronic Letters* Vol 29, pg1191-1193 (1993)
- [4] Hill K.O., Fuji Y., Johnson D.C. and Kawasaki B.S., "Photosensitivity in optical waveguides: application to reflection filter fabrication", *Applied Physics Letters* Vol 32, pg647 –649 (1978)
- [5] Meltz G, Morey W, Glenn W.H., "Formation of Bragg gratings in optical fibres by transverse holographic methods", *Optics Letters* Vol 14, pg823 –821 (1989)
- [6] Bilodean F., Malo B., Albert J., Johnson D.C., Hill K.O., Hibino Y., Abe M., and Kawachi M., "Photosensitisation in optical fiber and silica on silicon/silica waveguides", *Optics Letters* Vol 18, 953 – 955 (1993)
- [7] Othonos A., Kyriacos K. "*Fiber Bragg Gratings*" Artech House Norwood MA U.S.A. (1999)

- [8] Lambda Physik, “Excimer Laser writing of optical fibre gratings”, Product application note.
- [9] Atkins R.M., Mizrahi V. and Erdogan T., “248nm induced vacuum UV spectral changes in optical fibre preform cores: Support for a color centre model of photosensitivity”, Electron Letters Vol 29, pg385-387 (1993)

Chapter 4 Fibre Bragg grating sensing

4.1 *Introduction*

Fibre Bragg gratings have great potential for a wide range of sensing applications where quasi-distributed measurements are required such as strain, temperature, and pressure. Compared with other fibre based sensors, the fibre Bragg grating has many advantages which make it a very attractive method of sensing. One of the most important advantages that fibre Bragg gratings have is that unlike many other fibre based sensors the measurements are made based on the central wavelength shift. This means that all results are insensitive to fluctuations in the irradiance of the optical source of the system. The inscription of fibre Bragg gratings into the core of the fibre is non-intrusive and thus does not alter the fibre diameter making small diameter probes possible for applications which require them, such as strain mapping in composite materials. They are potentially inexpensive to mass produce which would allow them to compete against conventional electrical sensors. They can be multiplexed using similar techniques as used for other types of fibre-optic sensors. Some of these techniques include wavelength, spatial and time division multiplexing. They have one very important property which makes them very suitable for operation in industrial and harsh environments; they are unaffected by electrical noise, which has been for many years the one major problem with conventional electrical strain gauges, which tend to act like aerials. In recent years fibre Bragg gratings have been applied to more and more industrial test sites including strain sensing for large structures (i.e. bridges and high rise buildings), aerospace and marine vessel monitoring.

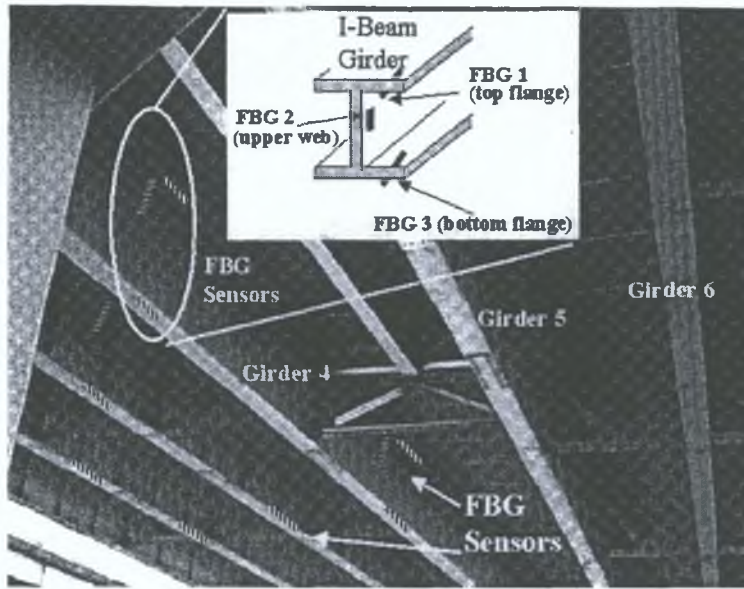


Figure 4.1 Fibre Bragg grating sensor array on the I-10 bridge in Las Cruces, New Mexico

4.2 Variation of Bragg wavelength and linewidth with strain

One of the most attractive applications of Bragg gratings is in strain measurement.

Fibre Bragg gratings are ideal for this application as the strain is converted to a shift in the Bragg wavelength (λ_B). This encoding means that the sensor gives absolute strain measurements, that the need for continuous measurements is forgone and periodic measurements only are needed.

The wavelength shift, $\Delta\lambda_B$, for an applied strain of $\Delta\varepsilon$ is given by

$$\Delta\lambda_B = \lambda_B(1 - p_e)\Delta\varepsilon \quad \text{E 4.1}$$

where p_e is the photoelastic coefficient of the fibre. This is given by

$$p_e = \frac{n_{eff}^2}{2} [p_{12} - \nu\{p_{11} + p_{12}\}] \quad \text{E 4.2}$$

p_{11} and p_{12} are components of the strain optic tensor and ν is Poisson's ratio. For typical telecommunications fibres the following table gives approximate values for the above variables.

Variable	Value
p_{11}	0.113 [1]
p_{12}	0.252 [1]
ν	0.16 [1]
n_{eff}	1.4675 [2]

Table 4.1

From this we can calculate p_e and thus evaluate the theoretical relationship between the change in the Bragg wavelength (λ_B) and the change in strain ($\Delta\varepsilon$). The photo elastic constant is found to be approximately 0.2085, from this we find that the relationship $\Delta\lambda_B/\Delta\varepsilon$ at 1300nm is approximately $1.03\text{ pm}/\mu S$. This is a linear relationship as shown in figure 4.2.

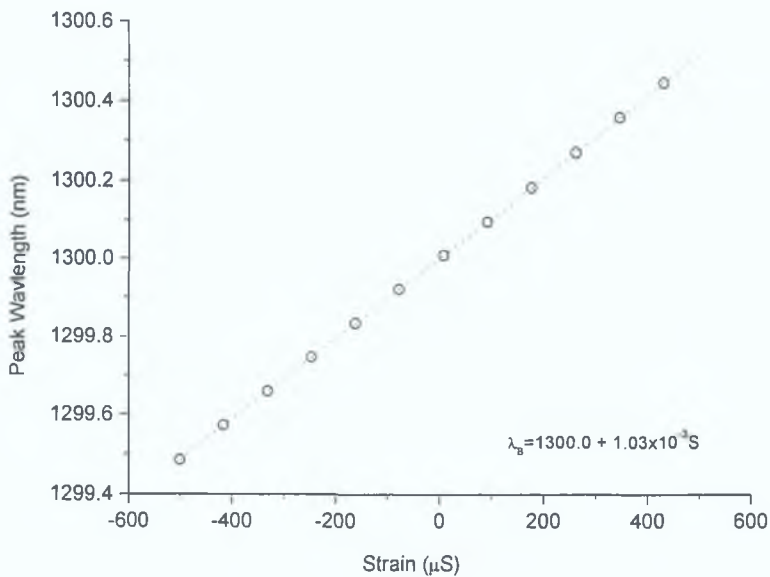


Figure 4.2

4.3 Variation of Bragg wavelength and linewidth with temperature

As with almost all sensor designs, it is most common that the sensor is inherently a temperature sensor. This leads in most cases to designs being employed which cancel out the effect of temperature. A full understanding of the effect of temperature changes on any sensor is therefore of the utmost importance. This is also true for fibre Bragg gratings. Much study has been done into the effect of temperature changes on fibre Bragg gratings, for sensors which need the effect removed and on sensors which are directly used as temperature sensors.

A change in temperature (ΔT) of the fibre Bragg grating will cause a shift in Bragg wavelength ($\Delta\lambda_B$) due to the thermal expansion which alters the grating spacing and the variation of the refractive index of the silica with temperature. This wavelength shift for a temperature change of ΔT may be written as

$$\Delta\lambda_B = \lambda_B(\alpha_\Lambda + \alpha_n)\Delta T \quad \text{E 4.3}$$

where $\alpha_\Lambda = (1/\Lambda)(\delta\Lambda/\delta T)$ is the thermal expansion coefficient for the fibre (this is approximately 0.55×10^{-6} for silica). α_n is the thermo-optic coefficient, and is given by $\alpha_n = (1/n_{\text{eff}})(\delta n_{\text{eff}}/\delta T)$ (this is approximately equal to 8.6×10^{-6} for telecommunications fibre). It can be clearly seen that the index change (α_n) is by far the most dominant effect by a factor of about 15. From equation 4.3 we can predict the response of the Bragg grating to temperature changes. Using the same values for the Bragg central wavelength as in the above section we find the temperature sensitivity of the grating to be $11.12 \text{ pm}/^\circ\text{C}$. This is shown in figure 4.3,

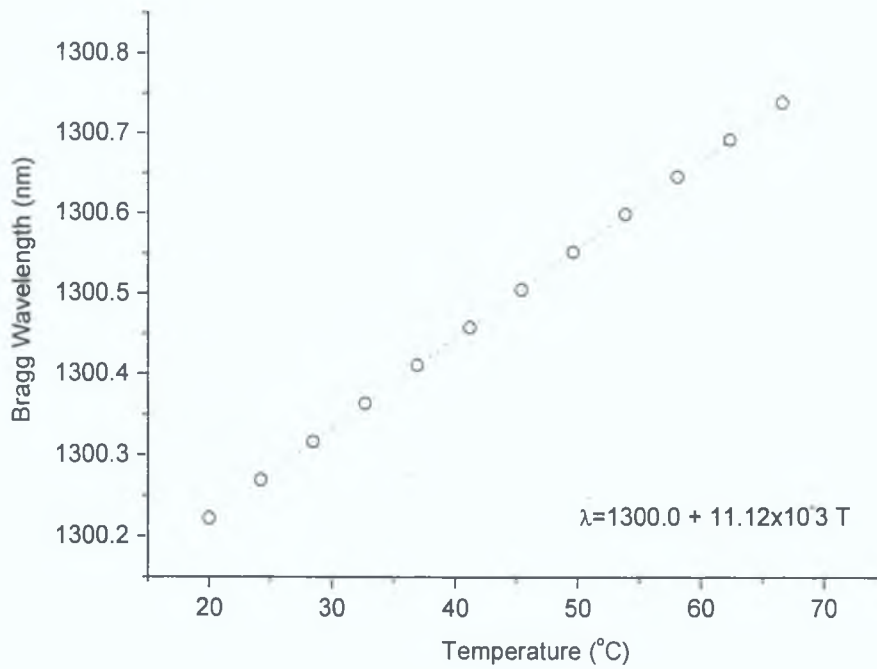


Figure 4.3

At very low temperatures silica glass has a negative thermal expansion coefficient [2] (i.e. temperatures below $\sim 150^\circ\text{K}$); this reduces the effectiveness of Bragg gratings in standard telecommunications fibres at cryogenic temperatures. The thermooptic index change is shown for silica glass in the graph below [3].

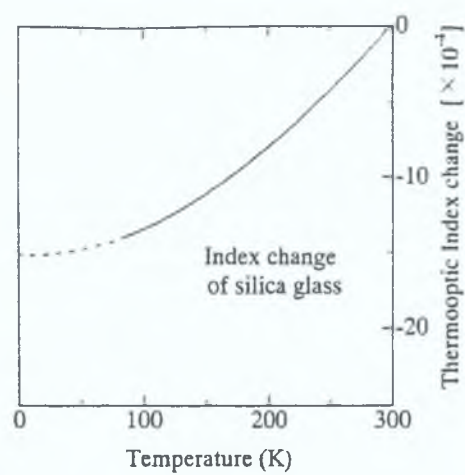


Figure 4.4

In the region that most studies have been carried out (200K – 300K) it can be seen that the thermo-optic index change is relatively linear.

4.4 Simultaneous strain and temperature measurement

In situations where a slowly varying strain or static strain is to be measured it is common that slowly varying large temperature excursions can be experienced. Hence some method of temperature compensation must be employed. A range of techniques have been proposed to achieve this, some of them are discussed below.

4.4.1 Reference fibre Bragg grating

This is the most common method; it employs two Bragg gratings one of which experiences the strain and temperature changes and the other grating experiences only the temperature variation. Thus the temperature effects can be removed as it is common to both Bragg gratings. This method is both simple and very effective.

4.4.2 Dual-wavelength superimposed fibre Bragg gratings

This method is based on the use of two fibre Bragg gratings being written in the same location in the core of the fibre. If one assumes that the wavelength shift is linear in strain and temperature, the wavelength shift is given by,

$$\Delta\lambda_B = K_\epsilon \Delta\epsilon + K_T \Delta T \quad \text{E 4.4}$$

where K_ϵ and K_T are the sensitivities of the grating to strain and temperature respectively. This assumes that the temperature and strain are independent. Hence for two superimposed gratings with differing wavelength we can write,

$$\begin{pmatrix} \Delta\lambda_{B1} \\ \Delta\lambda_{B2} \end{pmatrix} = \begin{pmatrix} K_{\epsilon1} & K_{T1} \\ K_{\epsilon2} & K_{T2} \end{pmatrix} \begin{pmatrix} \Delta\epsilon \\ \Delta T \end{pmatrix} \quad \text{E 4.5}$$

where 1 and 2 represent the two wavelengths. Once the sensitivities of the gratings (the K matrix) is known $\Delta\varepsilon$ and ΔT can be easily obtained. This concept has been shown for wavelengths of $0.85\ \mu m$ and $1.3\ \mu m$ [4].

4.4.3 Harmonics Method

For a strongly reflecting Bragg grating the refractive index perturbation may not be perfectly sinusoidal due to overexposure of the writing laser, resulting in the generation of harmonics. The wavelength of the first harmonic is twice that of the central Bragg wavelength. The first order amplitude will be small, around 2% of the amplitude of the central wavelength. This method, although useful in the fact only one grating is employed, requires the use of a broadband light source and detection scheme thus potentially making it very expensive or of poor resolution.

4.4.4 Dual Diameter fibre Bragg grating

It has been found that the responses to strain and temperature in a Bragg grating are affected by the cladding diameter [5]. By fusion splicing two fibre gratings with different cladding diameters together, such as shown below, the strain and temperature information can be extracted using a matrix scheme similar to that used in the superimposed grating method.

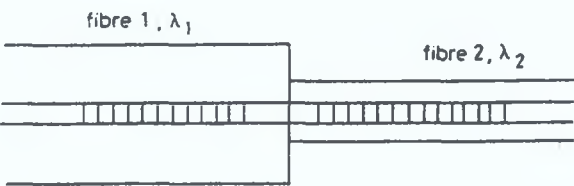


Figure 4.5

The change in the Bragg wavelengths ($\Delta\lambda_{Bi}$) of the two gratings by strain and temperature may be represented by

$$\Delta\lambda_{Bi} = \kappa_{\epsilon} \Delta\epsilon_i + \kappa_{Ti} \Delta T_i \quad i = 1, 2 \quad \text{E 4.6}$$

The strains experienced by the fibers will be related by

$$\frac{\Delta\epsilon_1}{\Delta\epsilon_2} = \frac{A_1}{A_2} \quad \text{E 4.7}$$

where A_1 and A_2 are the cross-sectional areas of the fibres.

It can be shown that the relationship between that wavelength shifts and the total strain experienced by the grating pair may be expressed as follows [5],

$$\begin{pmatrix} \Delta\lambda_{B1} \\ \Delta\lambda_{B2} \end{pmatrix} = \begin{pmatrix} \frac{K_{\epsilon 1}(l_1 + l_2)}{l_1 \left(1 + \frac{A_1 l_2}{A_2 l_1} \right)} & K_{T1} \\ \frac{K_{\epsilon 2}(l_1 + l_2)}{l_2 \left(1 + \frac{A_2 l_1}{A_1 l_2} \right)} & K_{T2} \end{pmatrix} \begin{pmatrix} \Delta\epsilon \\ \Delta T \end{pmatrix} \quad \text{E 4.8}$$

where l_1 and l_2 are the lengths of the fibre between the splice and the anchoring points of the fibres from the splice. The total system strain ($\Delta\epsilon$) is given by

$$\Delta\epsilon = \frac{(\Delta l_1 + \Delta l_2)}{(l_1 + l_2)} \quad \text{E 4.9}$$

When the two fibres have a similar response to temperature the centres of the two Bragg gratings will be shifted equally and thus their relative spacing will remain the same. Whereas a strain on the fibres will cause the centres to move differing amounts

causing a change in their relative spacing, thus making this system temperature insensitive.

4.4.5 Extrinsic techniques

Extrinsic techniques utilise external packages which either try to stabilise the temperature by sealing the grating in an insulated package or by encasing the fibre in a coating which nullifies the effect of temperature changes. The coating method uses the principle that materials expand at different rates, so by using a coating material which has a low rate of thermal expansion the fibre can be made to be less sensitive to temperature changes.

4.5 *Strain Gradient*

In most sensing situations the strain along the fibre is uniform. Therefore the strain may be directly determined from the reflected Bragg wavelength. If however, the grating is subjected to a strain gradient along its length not only will the reflected spectrum be altered in wavelength but it will also be distorted. This is due to the grating spacing (Λ) and the refractive index being nonuniform along the length of the grating. The spectral shape of the reflected spectrum will be dependent on the strain distribution along the grating's length. This strain gradient introduces a 'chirping' effect to the Bragg grating and thus allows us to calculate the strain induced along the length of the grating. This is illustrated in figure 4.5 [6].

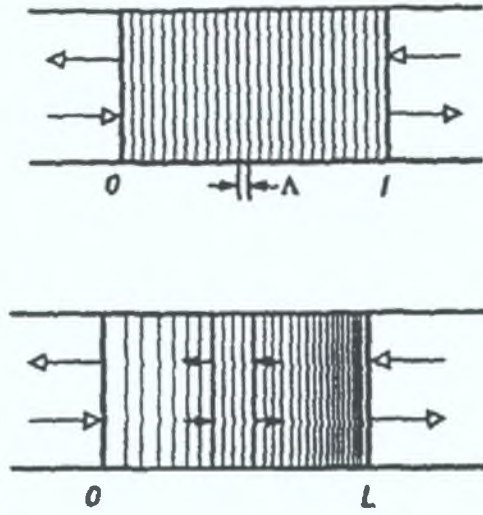


Figure 4.6

It can be seen that we can treat the Bragg grating with a strain gradient applied as a collection of smaller Bragg gratings with slightly differing pitches. If we assume that the gradient is linear across the length of the grating it was shown by Huang et al [6], that the line broadening ($\Delta\lambda$) appeared to obey

$$\Delta\lambda \approx \lambda_0 gL \quad \text{E 4.10}$$

This is obtained from the view that the spectrum obtained for the Bragg grating is just the sum of the reflections from each sub length section with its corresponding strain. For example if we are to use a fibre Bragg grating with a central wavelength (λ_B) of 1300.0 nm and a total grating length of 2.5mm it can be seen that the induced broadening of the reflected spectrum can be expected to be small, of the order of picometers, as can be seen in the graph below.

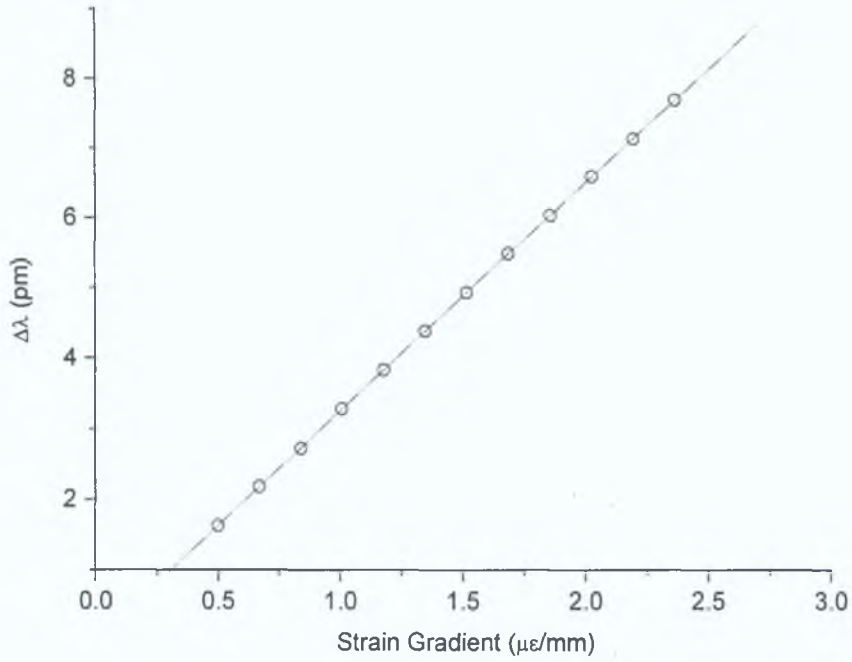


Figure 4.7

4.6 Other external effects

4.6.1 Pressure

When external pressure is applied to the area of the fibre Bragg grating the small fractional change in the diameter due to the applied pressure is negligible with respect to the change in refractive index and physical length. For a pressure change of ΔP , the corresponding change wavelength shift $\Delta\lambda_{B_p}$ is given by,

$$\frac{\Delta\lambda_{B_p}}{\lambda_B} = \frac{\Delta(n\Lambda)}{n\Lambda} = \left(\frac{1}{\Lambda} \frac{\delta\Lambda}{\delta P} + \frac{1}{n} \frac{\delta n}{\delta P} \right) \Delta P \quad \text{E 4.11}$$

with

$$\frac{\Delta L}{L} = - \frac{(1-2\nu)P}{E} \quad \text{E 4.12}$$

$$\frac{\Delta n}{n} = \frac{n^2}{2E}(1-2\nu)(2p_{12} + p_{11}) \quad \text{E 4.13}$$

where E is Young's modulus of the fibre. Given that $\Delta L/L = \Delta\Lambda/\Lambda$, the normalized pitch pressure is given by,

$$\frac{1}{\Lambda} \frac{\delta\Lambda}{\delta P} = -\frac{(1-2\nu)}{E} \quad \text{E 4.14}$$

$$\frac{1}{n} \frac{\delta n}{\delta P} = \frac{n^2}{2E}(1-2\nu)(2p_{12} + p_{11}) \quad \text{E 4.15}$$

By substituting equations 4.14 and 4.15 into equation 4.11, we obtain an equation for the wavelength-pressure sensitivity. This is given by,

$$\frac{\partial\lambda_{B_p}}{\partial P} = \lambda_B \left[-\frac{(1-2\nu)}{E} + \frac{n^2}{2E}(1-2\nu)(2p_{12} + p_{11}) \right] \quad \text{E 4.16}$$

For a Ge-doped fibre Bragg grating at $1.55\mu m$, $\partial\lambda_{B_p}/\partial P$ was measured as $-3 \times 10^{-3} \text{ nm MPa}^{-1}$ over a pressure range of 70 MPa [7].

4.6.2 Dynamic Magnetic Field

Bragg gratings have been shown to be capable of detecting dynamic magnetic fields utilising the Faraday effect to induce a slight change in the refractive index of the fibre experienced by left and right circularly polarised light traveling in the fibre [8]. In the presence of a longitudinal magnetic field, the fibre Bragg grating refractive index is changed for the two circular polarisations and because of this two Bragg wavelengths are obtained.

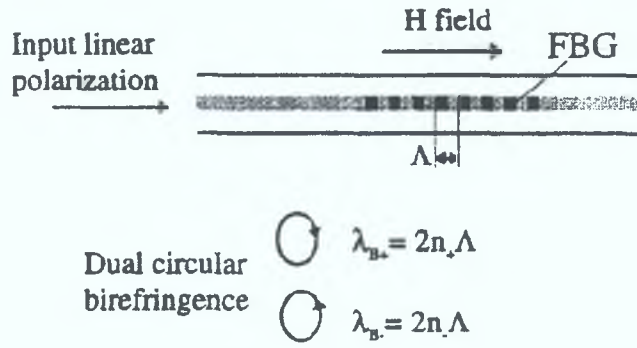


Figure 4.8 – Splitting of the Bragg resonance due to circular birefringence induced by a magnetic field.

$$\begin{aligned}\lambda_{B+} &= 2n_+ \Lambda \\ \lambda_{B-} &= 2n_- \Lambda\end{aligned}\tag{E 4.17}$$

Where the subscripts + and – represent the refractive index and Bragg wavelengths of the (left and right) circularly polarised light at the fibre Bragg grating. For normal telecommunications fibres this effect is very weak as it is determined by the inherent Verdet constant of the silica which is approximately $8 \times 10^{-1} \text{ rad T}^{-1} \text{ m}^{-1}$ at 1300 nm. The change is given by,

$$n_+ - n_- = \frac{V_d H \lambda}{2\pi}\tag{E 4.18}$$

,so that

$$\frac{\partial \lambda_B}{\partial H} = \frac{V_d \lambda_B}{\pi}\tag{E 4.19}$$

where V_d and λ_B are the Verdet constant and the wavelength of interest and H is the applied magnetic field. This wavelength shift is very small but B-fields of around 1 to 10^6 Gauss, or 100 Telsa, have been detected [8], showing a high linearity, making this approach suitable for applications in nuclear magnetic resonance and spectroscopy.

4.7 Conclusions

We have seen that the inherent properties of Fibre Bragg gratings make them suitable for strain sensors. This implementation is not without problems as the grating itself is highly sensitive to temperature. A number of methods for removing the temperature effect have been described. Some of these techniques are based on intrinsic effects of the gratings themselves, there have also been extrinsic methods described but these have been found to be less useful. A description of strain gradient effects, where the strain field is not uniform along the length of the Bragg grating, has been shown. This is a small effect, but it could prove a useful technique for measuring strain gradient in very localised areas. A description of two other external effects, pressure and large magnetic fields, have been discussed. It has been shown that the sensitivity to pressure is dominated by the change in the refractive index and the physical length of the fibre. The susceptibility of the Bragg grating to dynamic magnetic fields has been shown to be extremely small, and thus it's usefulness is limited to areas with large magnetic fields.

4.8 References

- [1] Friebele E.J., “*Fiber Bragg grating strain sensors: Present and future applications in smart structures*”, Optics & Photonics News, 33-37 (Aug. 1998)
- [2] Gupta S., Mizynami T, Yamao T., and Shimomura T., “Fibre Bragg grating cryogenic temperature sensors”, Applied Optics Vol 35, No 25 pg5202-5204 (1996)
- [3] Reid M.B. and Ozcran M., “Temperature dependence of fibre optic Bragg gratings at low temperature”, Optical Engineering, Vol 37 pg237-240 (1998)
- [4] Morley W.W., Meltz G. and Glenn W.H., “Fibre optic Bragg grating sensors” SPIE Proc, Vol 1169 pg98-107 (1989)
- [5] James S.W., Dockney M.L. and Tatam R.P., “Simultaneous independent temperature and strain measurement using in-fibre Bragg grating sensors”, Electronics Letters, Vol 32 pg1133-1134 (1996)
- [6] Huang S., LeBlanc M., Ohn M.M. and Measures R.M., “Bragg intragrating structural sensing”, Applied Optics, Vol 34 pg5003-5009 (1995)
- [7] Xu M.G., “Fiber Bragg grating based pressure sensor”, Electronics Letters, Vol 29 pg389-399 (1995)
- [8] Kersey A.D. and Marrone M.J., “Fiber Bragg grating high magnetic field probe”, 10th Optical Fibre Conference-Glasgow, Scotland, pg516-518 (1992)

Chapter 5 Design of a strain sensor system with temperature compensation

5.1 Introduction

The task of designing a system to interrogate one or more Bragg gratings, with a wavelength resolution of the order of tens of picometers (pm) is discussed with reference to the reasons why commonly available monochromators are unsuitable. As a fully temperature compensated system was required, a twin fibre approach, where one Bragg grating senses the temperature and the other both the strain and the temperature, was taken. The twin fibre approach led to the use of a fibre coupler to allow both Bragg gratings to be illuminated and interrogated simultaneously. To obtain the desired wavelength resolution a multi-layer interference filter used at oblique angles was employed. This facilitated resolutions of the order of $10pm$, which corresponds to approximately $10\mu\epsilon$ of strain or $1^\circ K$ in temperature. The interference filter was fully characterised using a Fourier transform spectrometer from which the effective refractive index of the filter (n^*) was calculated. A full description of the effect of light incident on a multi-layer interference filter at oblique angles is given. A description of the optical source (Edge emitting LED) and detector (Photodiode) used is included. The design of the turntable necessary to automate the rotation of the interference filter is shown, with attention being drawn to the importance of a small step angle and repeatability of rotational positioning. Finally a cantilever system is used to create a range of strain and strain gradients on the active Bragg grating, the dummy being used as a temperature drift reference channel.

5.2 Twin fibre approach

Bragg gratings being sensitive to both strain and temperature require some method of decoupling the two effects from each other before they may be used as strain sensors. One technique that may be employed is the use of two gratings, one which experiences both the strain and the temperature changes, and one that experiences the changes in temperature alone. The gratings employed here were chosen to be of a similar, but not identical, Bragg wavelength (λ_B). This choice allowed us to assume that the sensitivities of the Bragg grating with temperature (K_T), and strain (K_ϵ) were approximately the same.

$$\begin{aligned} K_T &= \lambda_B (\alpha_T + \alpha_n) \\ K_\epsilon &= \lambda_B (1 - p_e) \end{aligned}$$

E 5.1

where α_T is the thermal expansion coefficient for the fibre (this is around 0.55×10^{-6} for silica). α_n is the thermo-optic coefficient, and is approximately equal to 8.6×10^{-6} for telecommunications fibre. p_e is the photoelastic coefficient of the fibre; this is found to be approximately 0.2085 from equation 4.2. The two fibres used have Bragg gratings impressed at wavelengths of 1299.77nm and 1305.37nm respectively. Taking these figures the sensitivities of the gratings, to temperature and strain, at the two wavelengths can be calculated as given in the table below.

	$\lambda_{B(1299.77nm)}$	$\lambda_{B(1305.37nm)}$	% Difference
K_T	11.89 pm/°C	11.94 pm/°C	0.42%
K_ϵ	1.028 pm/µε	1.033 pm/µε	0.48%

This shows that for the chosen Bragg wavelengths we may consider their sensitivities to be equal for both temperature and strain. The system of removing the temperature effect is therefore straight forward and may be done as follows. Under zero strain conditions both of the central wavelengths of the gratings will be shifted by equal amounts and therefore their relative separation will remain constant. When a strain is applied to one of the Bragg gratings this will cause the central wavelength of that grating alone to be shift, thus changing the relative separation of the two gratings. Thus, from the change in the relative wavelength separation of the two gratings we may calculate the magnitude of the strain being applied to the non-reference grating.

$$\begin{aligned}\Delta\lambda_{B_{\text{Ref}}} &= K_T\Delta T + K_\epsilon\Delta\epsilon_1 \\ \Delta\lambda_{B_{\text{Active}}} &= K_T\Delta T + K_\epsilon\Delta\epsilon_2\end{aligned}\tag{E 5.2}$$

Since $\Delta\epsilon_1$ for the reference grating is equal to zero (remember that this gratings does no experience the strain effect) the shift in the wavelength $\Delta\lambda_{B_{\text{Ref}}}$ is caused entirely by the change in temperature experienced. Therefore the separation of the central wavelengths may be written as,

$$\begin{aligned}\Delta\lambda_{\text{Active-Ref}} &= \Delta\lambda_{B_{\text{Active}}} - \Delta\lambda_{B_{\text{Ref}}} = K_T\Delta T + K_\epsilon\Delta\epsilon_2 - K_T\Delta T - 0 \\ \Delta\lambda_{\text{Active-Ref}} &= K_\epsilon\Delta\epsilon_2 \\ \Delta\epsilon &= \frac{\Delta\lambda_{\text{Active-Ref}}}{K_\epsilon}\end{aligned}\tag{E 5.3}$$

By using this technique we have a simple but effective method of removing the ambient temperature effects from the system output, thus allowing us to directly access the strain experienced by the active Bragg grating.

Gratings with Bragg wavelengths of approximately 1300nm were chosen because of the window of silica at 1310nm (attenuation of approximately 0.34dB/km and the availability of high power LED sources and of PIN photodiodes with high

responsivities around 1300nm. The gratings were manufactured by Innovative Fibres of Ottawa, Canada from Corning SMF-28 singlemode fibre using a phase mask technique. The fibre (SMF-28) is a standard communications fibre with a cut off wavelength λ_{cf} of

$$1190nm \leq \lambda_{cf} \leq 1330nm$$

a core diameter of $8.3\mu m$, cladding diameter of $125\mu m$, numerical aperture of 0.13 and effective group refractive index (at 1310nm) of 1.4675. Between 1300 and 1310 nm the spectral attenuation of the fibre reduces from 0.35 to 0.34 dB/km. The gratings were fabricated to have a Gaussian profile reflection spectrum. The unstrained wavelength characteristics of a typical matched pair is shown below

	Grating No. 1	Grating No. 2
Central Wavelength (nm)	1299.77	1305.37
Full width at Half Maximum (nm)	0.46	0.44
Reflectivity at peak %	97.0	96.0

The Gaussian nature of the reflection spectrum of one such grating is shown in the technical specifications provided by the manufacturers. The resolution of the spectrum analyser used by the manufacturer was 0.1nm. The data is represented by the circles, while the Gaussian least squares fit is represented by the thin line in the following figure.

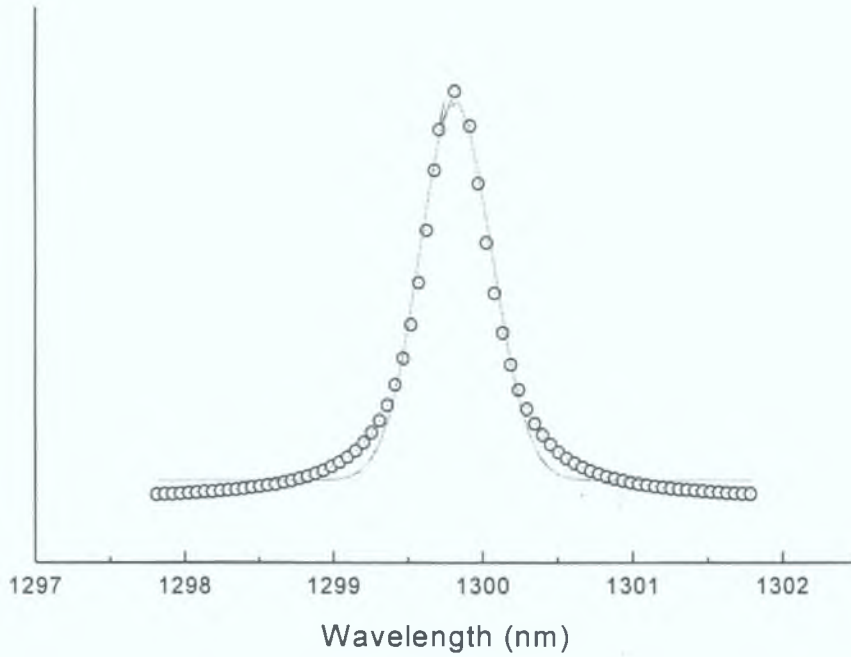


Figure 5.1

This typical (unstrained) grating spectrum was curve fitted to the Gaussian apodised grating model function given in Equation 2.49 and the best fit values of the grating parameters found to be

- | | | |
|-------|-------------------------------------|---|
| (i) | Maximum refractive index modulation | $\delta n_{eff} = 1.001 \times 10^{-3}$ |
| (ii) | Grating Length | $L = 2.5 \text{ mm}$ |
| (iii) | Gaussian apodisation variable | $\alpha = 4.1 \times 10^4 \text{ m}^{-2}$ |

5.3 Wavelength analyser

5.3.1 Commercial systems

There are many commercial systems which have been employed to interrogate fibre Bragg gratings. These tend to have one of two disadvantages, the most important being that they often have a resolution which is only of the order of 100pm, thus making them unsuitable for detecting small strains (note $1 \text{ pm} \cong 1 \mu\epsilon$). Secondly most

of the instruments, which are capable of reaching resolutions low enough to render them suitable for small strain detection, are very expensive. Listed below are some of the commonly used instruments for Bragg grating interrogation.

Analyser System	Manufacturer	Spectral Range (nm)	Resolution (nm)	Cost IR£
Digikrõm DK242	CVI Laser Corp	330-1500	0.04 [focal length 0.25m]	11,465
AQ-6310B	Ando Corp	1000-1500	0.4	8,500
S1000	Ocean Optics	850-1450	0.4	5,600

We required an instrument which had a resolution of the order of a few picometers and was relatively inexpensive. For these reasons a multi-layer interference filter was chosen for this purpose. The interference filter has the advantage that it is both inexpensive and its resolution is only limited by the minimum step size of the rotation stage employed. For general spectrum analysis interference filters have limited usefulness as they are only capable of working within small wavelength ranges, of the order of $35nm$. For this application this was found to be quite sufficient as a $20nm$ shift in the Bragg wavelength would correspond to a change of $2000^{\circ}C$ in the ambient temperature or a strain change of $20,000\mu\epsilon$. Both of these are well outside the normal operating limitations of the fibre used, so this does not place any limitation on the interference filter’s usefulness in this situation.

5.3.2 Multi-layer interference filter

To attain the spectral resolution required to interrogate the Bragg grating a multi-layer interference filter was chosen. A multi-layer interference filter consists of a number of

layers of dielectric materials of differing refractive indices coated onto a glass substrate. The dielectric materials on the substrate have different thickness. The combination of materials of differing refractive index ($n_1 - > n_m$) and thickness give rise to an overall refractive index for the filter (n^*). By careful choice of the combination of materials and thickness one can produce a filter of almost any nature. An interference filter of a narrow bandwidth at one distinct wavelength was required for our purpose. When light is incident on an interference filter at an oblique angle the central wavelength of transmission has been shown to shift to shorter wavelengths, the expression for this shift is given by Blifford (1966) [13],

$$\lambda_{\theta} = \lambda_0 \left[1 - \left(\frac{n_0}{n^*} \right)^2 \sin^2 \theta \right]^{\frac{1}{2}} \quad \text{E 5.4}$$

where,

λ_{θ}	Peak wavelength at incident angle (θ)
λ_0	Peak wavelength at normal incidence ($\theta = 0$)
n_0	Refractive index of the incident medium (air=1.0)
n^*	Effective index of filter
θ	Angle of incidence

This equation only holds for small angles, i.e. $\theta < 20^\circ$. At larger angles of incidence the corresponding angles of total internal reflection within the filter give rise to phase changes on reflection which are dependent on the plane of polarisation of the light. This in turn affects the condition for constructive interference in the filter and gives

rise to a splitting of the transmission spectrum. The spectral transmittance of a Fabry Perot filter is Lorentzian in nature [Lissberger (1959,1968)] [14],[15] with a functional form of

$$T(\theta) = \frac{T_0 b^2}{b^2 + \{2(\lambda - \lambda_0) + \lambda_0 \theta^2 / (n^*)^2\}^2} \quad \text{E 5.5}$$

where b is the halfwidth at half maximum of the transmittance at normal incidence $\theta = 0$, and T_0 is the filter's power transmittance at normal incidence. Equation 5.5, the Lorentzian transmittance function, can be written as

$$T(\theta) = \frac{T_0 b^2}{b^2 + \{2(\lambda - \lambda_0) + C \theta^2\}^2} \quad \text{E 5.6}$$

where $C = \lambda_0 / (n^*)^2$ and θ is a function of the number of steps (N) of the stepper motor from its location at $\theta = 0$. For the interference filter used the variables have the following values:

$$\begin{aligned} \lambda_0 &= 1308.5 \text{ nm} \\ b &= 2.537 \text{ nm} \\ C &= \lambda_0 / (n^*)^2 = 682.33 \text{ nm} \\ C \theta^2 &= 2.6939 \times 10^{-6} N^2 \end{aligned}$$

so that the transmittance function $T(\theta)$ can be calculated at each value of the incident angle θ . T_0 is a constant which is arbitrarily set to 1.0.

The wavelength shift of $T(\theta)$ is shown in the following spectrum which was taken with a Fourier transform spectrometer for incident angles θ in the range 0 to 20° C.

The filter used was manufactured by the Raynard Corporation of CA. U.S.A. with a normal incidence wavelength of transmission of ~1308nm.

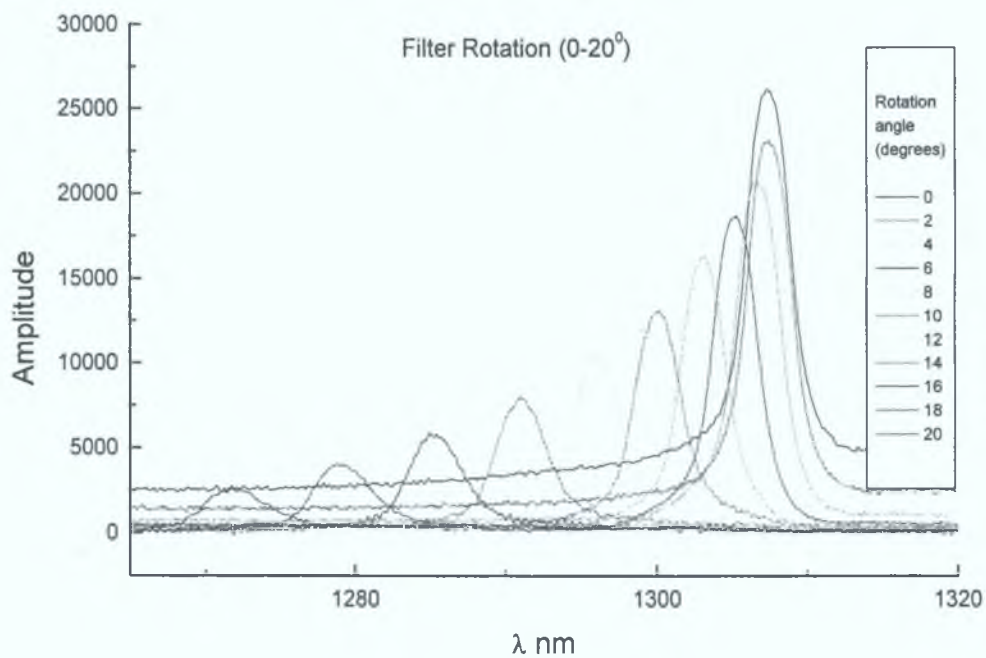


Figure 5.2

By curve fitting the above spectra to equation 5.6 a value for the effective refractive index (n^*) of the filter was obtained. A value of

$$n^* = 1.74195$$

was measured for the filters effective index at an ambient temperature of 21.0° C .

Because refractive index and dimensions are temperature dependant the transmission properties of Fabry Perot filters are a function of temperature. The shift in peak transmission wavelength is small with a value in the range 0.02 – 0.2nm/° C [2].

Because the system employed twin gratings, the separation of the central peaks of the Bragg gratings will remain constant as both grating spectra will shift equal amounts if

the filter temperature drifts, thus eliminating the effect of the temperature drift of the filter's peak transmission.

5.3.3 Optical source considerations and selection

As the Bragg grating system is based on wavelength detection, the intensity of the spectrum is of little importance once that spectrum is detectable. Thus the selection of a source to illuminate the gratings has very few constraints. The desired properties are as follows. Firstly it must be broad enough to cover the desired wavelength range. As most LED packages have a broad linewidth, this did not prove to be a difficulty, with most LED packages around the 1300nm range having full width at half maximum of approximately 80nm. The majority of LED in the 1300nm region are made of Indium Gallium Arsenide Phosphide (InGaAsP). The figure below shows the spectrum of the LED package used.

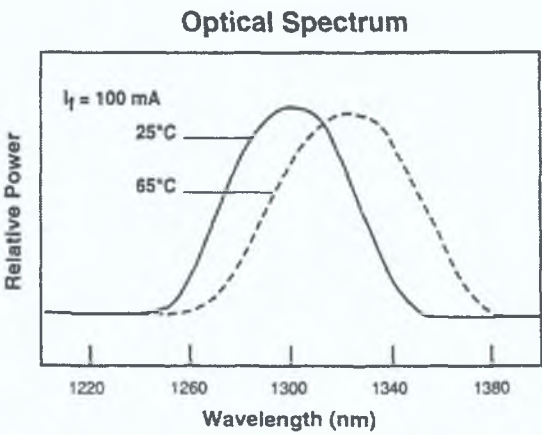


Figure 5.3

The other concern was the coupling of a good percentage of the light from the LED package into the fibre core (8.3 μm). This was easily achieved by the use of a source which is already designed to couple a single mode fibre to the LED in the package. The package chosen had a standard “FC” receptacle, into which the fibre, terminated with an FC connector, was connected. The LED chosen was manufactured by

EPITAXX Optoelectronic devices [6]. The LED was driven by a constant current source with a voltage regulator. A current of 100mA was chosen to drive the package at its optimum for optical output and lifetime.

5.3.4 Optical detector considerations and selection

The choice of detector was also very important as this element of the system needed to be able to detect light levels of the order of a few microwatts (μW). As wavelengths around the 1300nm region were being detected a Indium Gallium Arsenide (InGaAs) detector was chosen. It was important that the photodiode had a good spectral responsivity as this severely degrades the spectral performance of the detector. A plot of the surface responsivity is given below.

**Surface Plot of Response at 1300 nm
ETX 3000T5**

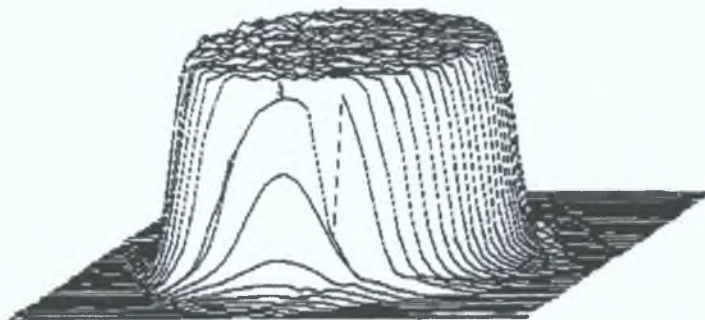


Figure 5.4

The photodiode was operated under reverse bias, under these conditions the low dark current of InGaAs becomes advantageous. Dark current is important because shot noise becomes the dominant source of noise. The equation below gives the formula for the r.m.s. shot noise current of a photodiode [7] per unit measurement bandwidth.

$$I_{SH}^2 = 2q|I_{PH}| + 2q|I_D| \quad \text{E 5.7}$$

with

I_{SH} = the shot noise current

q = the unit of electronic charge

I_{PH} = the photo generated current

I_D = photodiodes dark current

For example, the shot noise of an unilluminated 2mm InGaAs photodiode with a reverse bias of 5V and at room temperature arises from the dark current. Using the dark currents typical value of 12nA [7], the noise current is calculated to be $62 \text{ fA} / \text{Hz}^{1/2}$. InGaAs photodiodes have a wide operating region spanning 800nm to 1700nm approximately. The spectral response of the EPITAXX photodiode chosen is extremely stable over the 1300nm region we are interested in, as can be seen from the graph below.

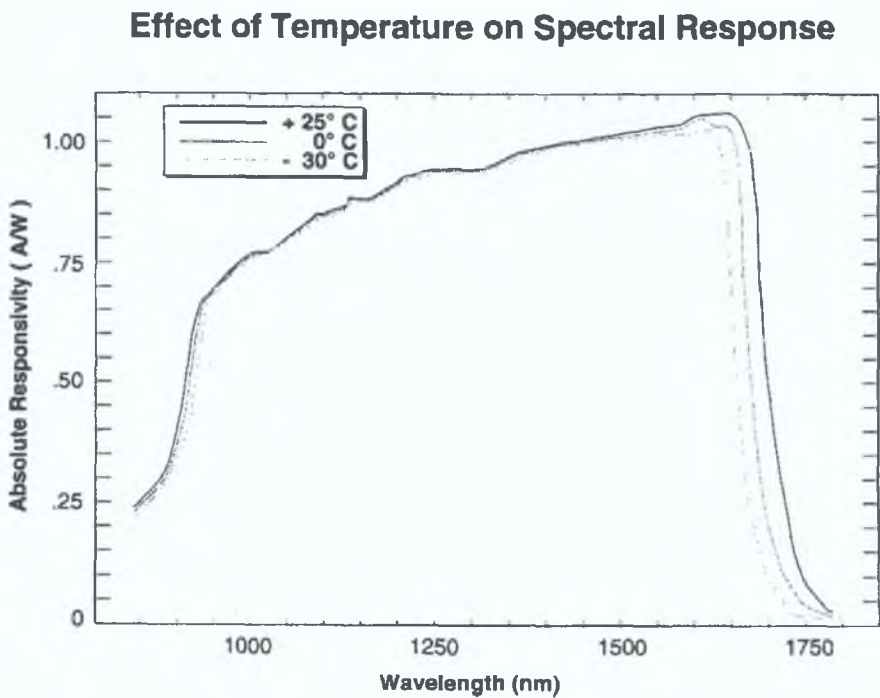


Figure 5.5

5.3.5 Grin lens

The interference filter was used as a monochromator element and its transmission properties are dependant on the incident light being in a parallel beam. In step index fibres the light emerges from the fibre end over a range of angles (in a cone of typically 5°). To eliminate this problem a grin (graded index lens) was employed. Grin lens can be used to collimate or focus light emerging from or entering a fiber optic system. The theory of grin lens is that instead of using conventional optics which require the formation of a curved surface on the optical material to manipulate the incident rays, grin lens have a graded index profile so that the ray path is continuously altered through a smooth refractive-index variation. The refractive index profile is given by [8],

$$N(r) = N_0 \left(1 - \frac{A}{2} r^2 \right) \quad \text{E 5.8}$$

where

N_0 = base refractive index (at the optical axis)

A = Gradient constant

r = radial position of the lens

This leads to a refractive index profile as shown below

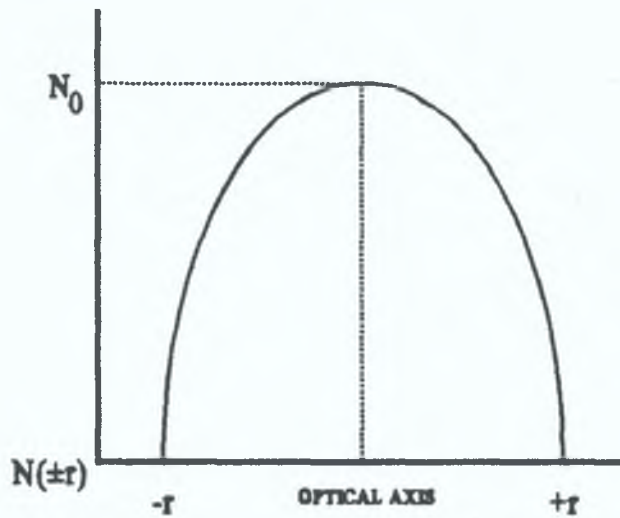


Figure 5.6

Another important concept in grin lens is the pitch. This describes the length of grin lens needed to complete one cycle, or sine wave. Since we require a grin lens to collimate our cone shaped beam from the optical fibre we require a 0.75 or 0.25 pitch grin lens as shown in the diagram below.

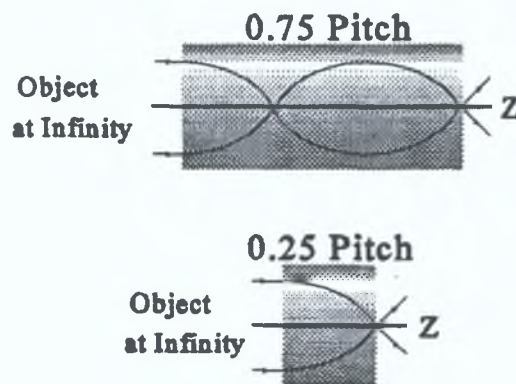


Figure 5.7

The use of a 0.25 pitch grin lens as shown facilitated the shaping of the beam of the optical fibre to give a parallel beam of light incident on the interference filter.

5.3.6 Fibre couplers

To illuminate both gratings simultaneously from one single input and collect the back reflected light from the gratings, the two fibres containing the Bragg gratings were coupled together. The optical fibre configuration is shown below with the coupling being achieved at the coupler which is represented as a large black dot.



Figure 5.8

The principal function of a fiber optic coupler is to transfer the optical power from one fibre to a different one in a controlled manner. This may be achieved by many means but by far the most common is the method described below. This method entails tapering the fibres by heating and drawing them together in a spiral fashion. For many applications the two fibres being coupled are required to receive 50% or 3dB of the power each, and when coupling two identical fibres together this is the most common outcome. Coupling is possible because the fields of a fibre mode extend into the cladding and interact with any other fibre which may be present. Using coupled mode theory we get the following equations for the power in each of the two fibres [9],

$$P_1(z) = \frac{1}{1 + a_+^2}, \quad P_2(z) = \frac{a_+^2}{1 + a_+^2} = 1 - P_1(z) \tag{E 5.9}$$

where

$$a_+(z) = \frac{\beta_2 - \beta_1}{2i\beta(z)} + \frac{1}{F} \tag{E 5.10}$$

and

$$F = \frac{1}{\left\{1 + \frac{(\beta_1 - \beta_2)^2}{-4\beta(z)}\right\}^{1/2}} \quad \text{E 5.11}$$

When both fibres are nearly identical, $\beta_1 \cong \beta_2$, then $F \cong 1$ and $a_+ \cong 1$, then the power in both fibres are around 3dB of the original power. This then gives us the required optical power to both Bragg gratings. The fibres carrying the Bragg gratings used in this work were coupled using a Gould fibre coupler (S/N 2068409) configured as in Figure 5.8.

5.4 Automating wavelength analysis

As we had chosen to use a rotating multi-layer interference filter as our spectral analyser, a system to automate the rotation of the filter was required. This system had to give small angular steps, as a spectral resolution of the order of a few picometers was required. This was achieved by employing a rotation stage driven by a stepping motor connected through a gearbox. A commonly available 1.8° stepper motor was chosen; this was also capable of producing half steps of 0.9° . This stepper motor was connected to the rotation stage through a 250:1 gearbox giving us a step size of 3.6×10^{-3} degrees. As from equation 5.4 we can see that the relationship between filter angle and the central wavelength of the filter is non-linear we have a range of wavelength resolutions across the useful range of the filter, this is shown below.

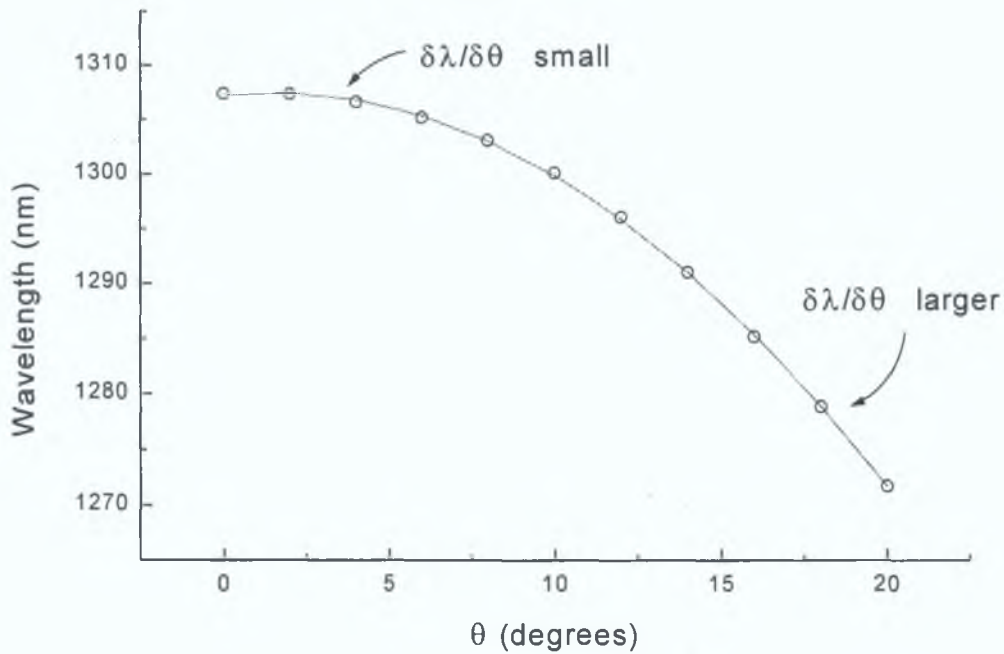


Figure 5.9

In the region of interest i.e. 1300-1305nm a single step of the stepper motor system corresponds to a wavelength shift in the filter transmittance of 2.65 pm . This is an acceptable resolution for the strains we wish to detect. Stepping motors operate by energising the coils in a particular sequence which cause the shaft to rotate as each electromagnet in turn opposes the permanent magnet connected to the drive shaft. The following diagrams show the most common configuration for stepper motors and the sequence needed to generate a sequence of half steps.

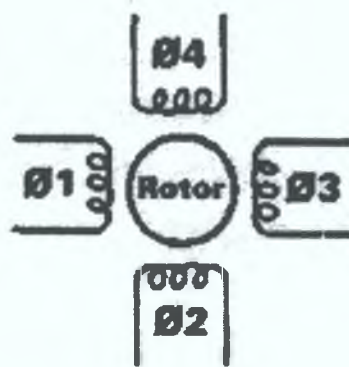


Figure 5.10

Step Number	$\phi 1$	$\phi 2$	$\phi 3$	$\phi 4$
	On	Off	On	Off
1	On	Off	Off	Off
2	On	Off	Off	On
3	Off	Off	Off	On
4	Off	On	Off	On
5	Off	On	Off	Off
6	Off	On	On	Off
7	Off	Off	On	Off
8	On	Off	On	Off

Since we do not require the stepper motor to move any substantial load the normal torque considerations can be ignored. Another property of stepper motors is their positional accuracy, this represents the tolerance of each angular step movement. This is typically within 5% of one step [10], which corresponds to a wavelength error of approximately $0.15\mu m$. This is a non-cumulative error, i.e. this remains constant regardless of the number of steps advanced. Overshoot may also occur when making a single step, the rotor may oscillate around its new position. This is a small effect here as the gearbox and rotation stage tend to add additional frictional damping, thus reducing the amount of overshoot. An example of overshoot can be seen in the graph below.

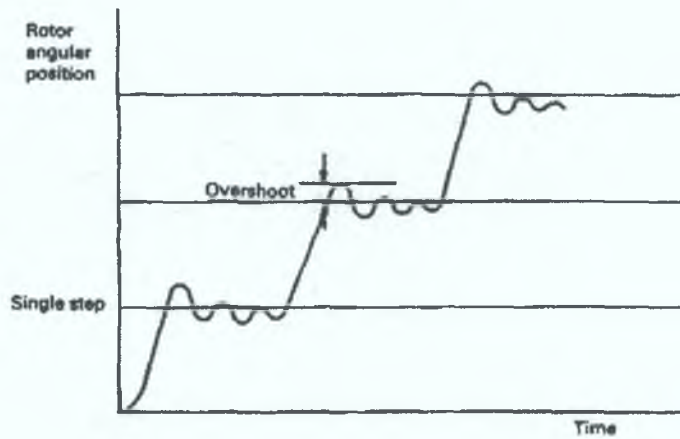


Figure 5.11

In this application by far the most critical property of the stepper motor was resonance. Certain operating frequencies cause resonance and the motor can lose track of the drive input causing the motor to act in an erratic manner. An audible vibration is the most common sign of resonance, although at some high frequencies the motor may just lock in one position causing a 'burn out'.

To activate the motor, i.e. energise the motors coils, some electronic equipment was required to produce the desired sequence of coil currents. This was achieved by using a 'off the shelf' stepper motor driver board. The board chosen was also capable of taking as an input a sequence of TTL level signals to cause the motor to step and change direction. A personal computer (PC) was used to signal the stepper motor when to turn and in which direction. A computer program was written to produce the necessary signals to cause the stepper motor to turn. The computer and stepper motor controller were interfaced using a Bitronic[®] interface card. This card also had a function to input to the computer a voltage signal in the region $\pm 10V$. This function was employed to capture the return signal from the photodiode amplifier circuit for each step of the filter. This combination gave us a fully functioning spectral analyser.

5.5 *The cantilever strain rig*

To expose the Bragg grating strain gauge to a range of variable strains both in compression ($\varepsilon < 0$) and extension ($\varepsilon > 0$) a metal cantilever rig was constructed consisting of a stainless steel 20x4mm cross-section bar in a constant temperature environment. The bar was clamped at one end ($x = L$) and could be moved vertically at the free end by a micrometer gauge. The free end displacement was known to 0.01 mm accuracy. The cantilever was sand blasted using 30 micron grit to create a surface to which the fibre carrying the active Bragg grating gauge could be bonded using epoxy resin.

The cantilever housing carried a 250W trace heating element in a sub floor which was controlled using a Eliwell controller, the cantilever temperature being monitored by a Eirlec MT140 type J thermocouple with digital display and 0.1°C accuracy. The cantilever environment could be varied from room temperature to 65°C with a stability of 1°C. An example of the temperature profile of the constant temperature environment is shown below.

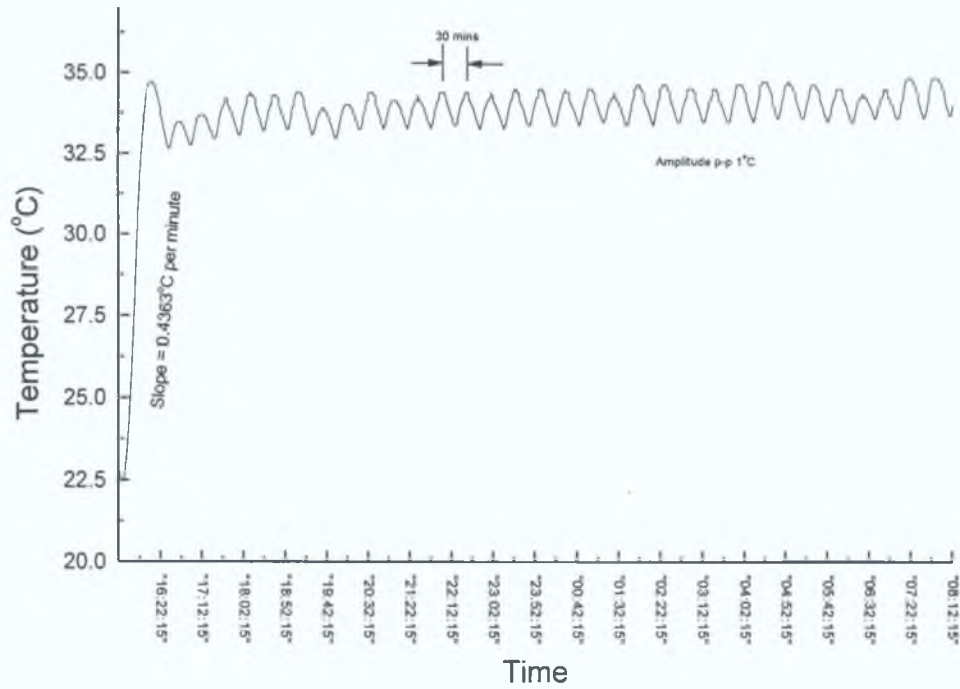


Figure 5.12

It can be seen from figure 5.12 that the cantilever stabilised to within $\pm 0.7^{\circ}C$ of the set point temperature.

For a cantilever of length L_c , free end depression d the strain $\varepsilon(x)$ on a plane of depth a from the neutral axis and a distance x from the free end is given by [11] [12],

$$\varepsilon(x) = \frac{-3dax}{L_c^3} \tag{E 5.12}$$

The strain gradient is constant at all points along the plane with a value of

$$g = \frac{-3ad}{L_c^3} \tag{E 5.13}$$

The strain range of the cantilever at $x = 355\text{mm}$, $L = 385\text{mm}$, and $a = 2.0\text{mm}$ was from approximately $-260\mu\epsilon$ to $500\mu\epsilon$ and the range of strain gradient was $-0.837\mu\epsilon/\text{mm}$ to $1.884\mu\epsilon/\text{mm}$. With a typical Bragg grating length of 3mm the system used created a strain differential from one edge of the grating to the other of about $-2\mu\epsilon$ to $4\mu\epsilon$. Over the range specified the radius of curvature of the cantilever varies from ∞ for no free-end deflection to approximately 4m for a free-end deflection of 12mm .

The full optical system used for wavelength and linewidth analysis is shown in figure 5.12 and the electronic system is shown schematically in figure 5.13.

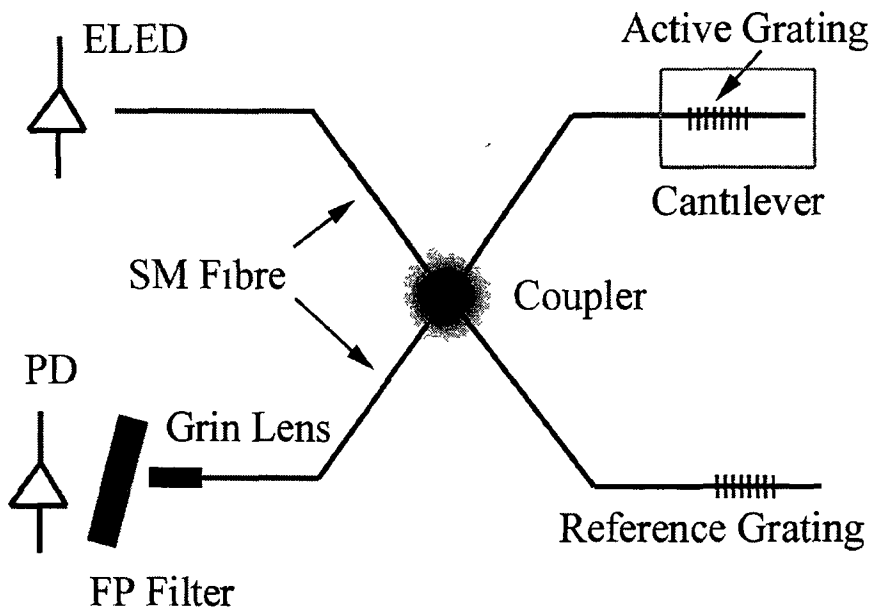


Figure 5.13 Schematic of optical system

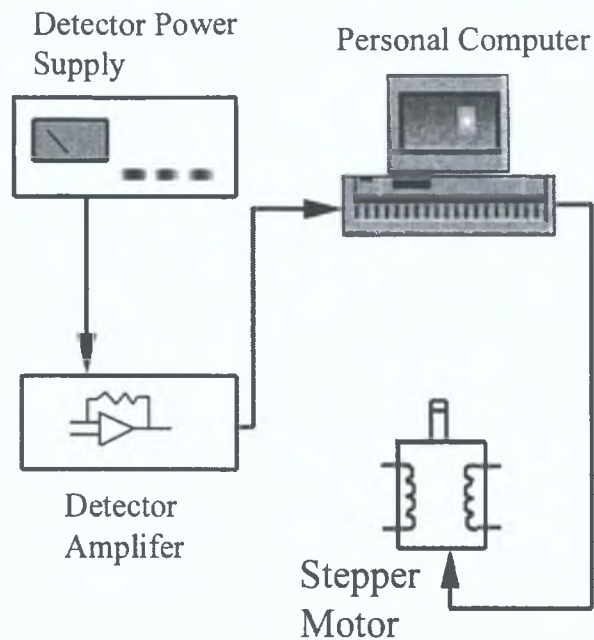
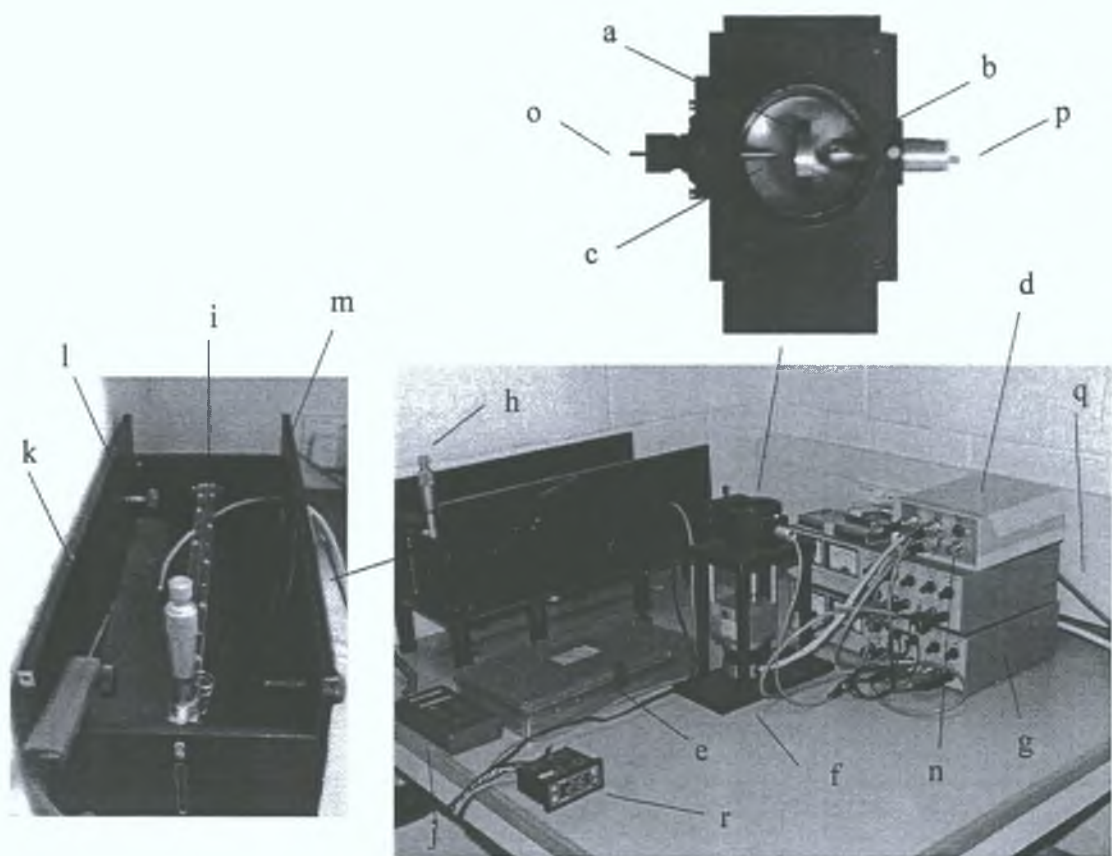


Figure 5.14 Schematic of electrical system

5.6 Conclusion

We have shown that a multilayer interference filter may be successfully employed as a spectrum analyser when used at oblique angles. The overall optical system is simple in nature and only requires the careful choice of optical components to function properly. A system to create a set of known strains in a fibre grating and then to interrogate the grating in wavelength using a rotating Fabry Perot interference filter has been discussed. The system was designed to have a strain range of approximately -200 to 500 microstrain with a strain gradient of approximately -0.7 to 1.5 microstrain per millimeter. A strain sensitivity of about 10 microstrain was the target of the strain measuring system. The full system as it is used is shown in the diagram below.



a	Interference filter	j	Thermocouple readout
b	Detector (Photodiode)	k	Thermocouple
c	Grin lens	l	Heater control probe
d	System Electronics	m	Reference grating
e	Fibre and coupler	n	LED Output
f	Stepper motor	o	Fibre alignment chuck
g	Power Supply	p	Cable to detector amplifier
h	Micrometer	q	Cable to PC interface
i	Cantilever and active grating	r	Heater controller

Figure 5.15

The system achieved resolutions in wavelength of approximately 3 pm , which is comparable to some of the best commercial systems available. This system is inexpensive to construct, but is limited in usefulness to small spectral ranges. The main drawback of this system is the large amount of convolution of the reflected

Bragg spectrum which takes place as predicted in chapter 2 This leads to the need for a software deconvolution system to remove the filter function from the spectrum

5.7 References

- [1] Rao Yun-Jiang, "In-Fibre Bragg grating sensors – review article", Measurement Science Technology, 8 (1997) Pg355-375
- [2] Infrared Engineering, "Optical Filters and Coatings", Product data sheet Pg3,4,27
- [3] Steven Poncelet, DiCon Fiberoptics, CA, U.S.A., personal communication
- [4] Scott Frank, Raynard Corporation, CA, U.S.A., personal communication
- [5] Driscoll W.G and Vaughan W., "*Handbook of Optics*", (1978), Chapter 8 Pg 86-88
- [6] Epitaxx Ltd., "Product sheet – 1300nm High Power ELED Modules"
- [7] Epitaxx Ltd., "Product sheet – Large area *InGaAs* Photodiodes"
- [8] NSG Europe, "Selfoc[®] Product Guide", Pg3-8
- [9] Snyder A.W. and Love J.D., "*Optical Waveguide Theory*", Chapman and Hall, London, Pg575-579 (1983)
- [10] Radionics, "Stepper motors – Data sheet", Number B8199, (1984)
- [11] Timoshenko S, "*Strength of Materials*", Van Nostrand N.Y., (1958)
- [12] Craig R.R., "*Mechanics of Materials*", Wiley N.Y., (1991), Eqn. 6.23
- [13] Blifford I.H. Jr., "Factors affecting the performance of commercial interferences filters", Applied Optics Vol 5, No 1 pg105-111 (1966)
- [14] Lissberger P.H., "Properties of all-dielectric interference filters", Journal of the Optical Society of America Vol 49, No 2 pg121-125 (1959)

- [15] Lissberger P H , “Effective refractive index as a criterion of performance of interference filters”, Journal of the Optical Society of America Vol 58, No 12 pg1586-1590 (1968)

- [16] Macleod H A , “*Thin Film Optical Filters*”, Hilger, Bristol U K (1985)

Chapter 6 Deconvolution of Spectra

6.1 Introduction

The effect of using a thin film interference filter to interrogate the back reflected light from the Bragg gratings is to produce a convoluted spectrum. Under normal circumstances the instrument used to interrogate a spectrum would be chosen to be of a linewidth which would be much smaller than that of the spectral lines to be detected. As the linewidth of the reflected signal from the Bragg gratings is of the order of 500 picometers and that of the interference filter is 1.5 nm (or three times larger the spectrum obtained) it is heavily convoluted, as shown below, and must be analysed to obtain the correct Bragg wavelength and linewidth.

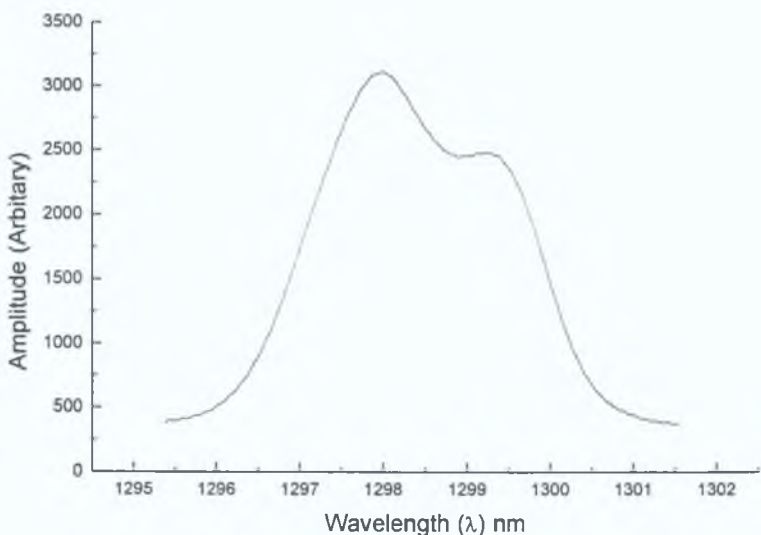


Figure 6.1

To successfully deconvolve the data a number of factors have to be taken into account:[8]

- Change of interference filter linewidth with angle
- Non-linearity, with respect to λ , of the central peak of the filter at arbitrary angles

- Transmittance reduction of the interference filter with angle

These effects can clearly be seen in the graph below,

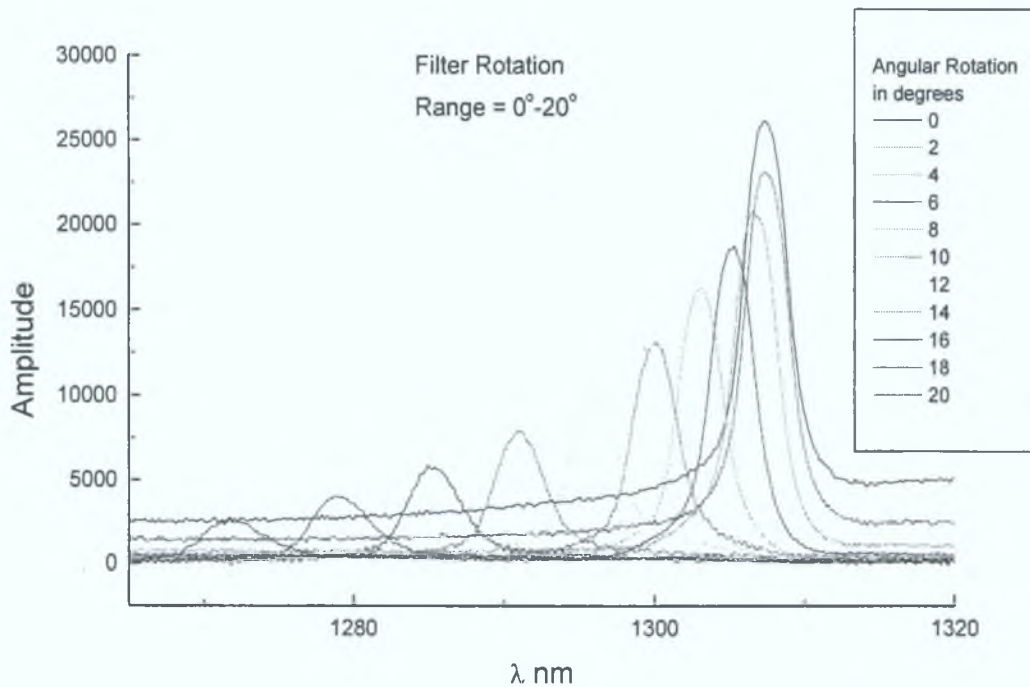


Figure 6.2

The fitting routine needed to deconvolve the spectra, would have to deal with at least ten variables, as the full system is described as the sum of the two Bragg grating reflections convolved with a rotating interference filter.

6.2 Genetic algorithm approach to find solution in large search space

With such a large number of variables most standard fitting schemes would be very slow to reach a minimum [6]. The use of genetic algorithms to find local minima in large search spaces has become more common in recent years. Genetic algorithms are heuristic search techniques that incorporate, in a computational setting, the biological notion of evolution by means of natural selection [5]. With genetic algorithms the problem of multiple local minima and non well behaved landscapes can easily be overcome. For example consider the following function of two variables:

$$f(x, y) = [16x(1-x)y(1-y) \sin(n\pi x) \sin(n\pi y)]^2$$

$$x, y \in [0, 1] \quad n = 1, 2, \dots$$

E 6.1

The optimising task in this case is to find the maximum evaluation of f . The figure below shows the surface plot of the above function for $n = 9$.

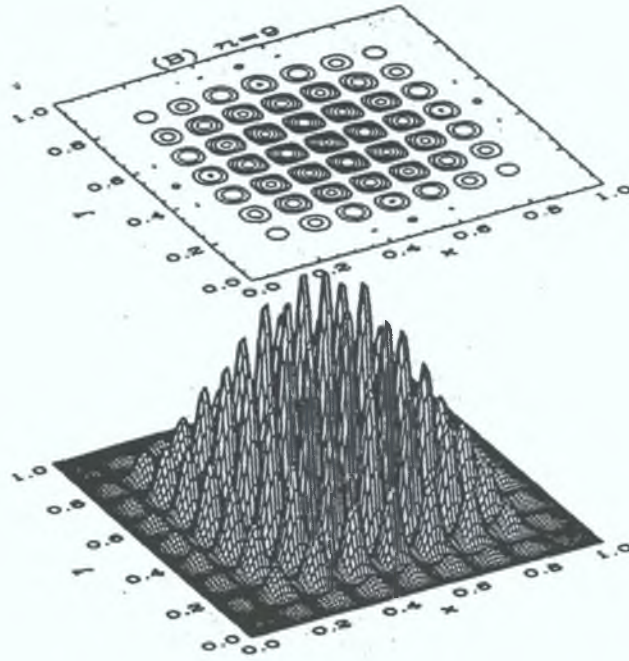


Figure 6.2 - Surface and Contour plots of function ^[1]

To find the maximum value of f by conventional methods for values of n which are large can be seen to be difficult, for example when $n = 9$ there are 81 local maxima.

If one is to imagine the above surface plot turned upside down and using a small ball to find the maximum the solution will only be found if the ball is to directly dropped

in the interval $\left(\frac{4}{9} \leq x \leq \frac{5}{9}, \frac{4}{9} \leq y \leq \frac{5}{9}\right)$ centered on $(x, y) = (0.5, 0.5)$. Any other

starting point will cause most standard methods such as *iterated hill climbing* [7] schemes to find a secondary maximum. Genetic algorithms by nature are global solution finders, because of their random nature they are not restricted to any one

section of the solution space. They have an equal probability of searching each point on the search space. Classical genetic algorithms employ an encoding scheme to describe the possible solutions in the gene pool, this is very much like the genetic encoding found in all biological species [6]. The difficulty with this method is that it requires that an encoding scheme to be developed for each problem encountered, which can be a very time consuming task.

A top-level view of a genetic algorithm is as follows;

- Construct a random initial population and evaluate the fitness of each member of the population.
- Construct a new population by breeding selected individuals from the old population, optionally one may randomly mutate the new population members.
- Evaluate the fitness of each member of the new population
- Replace the old population with the new population
- Test convergence, unless the fittest solution found matches the target within tolerance

Using this method for the above problem it can be seen from the diagrams below that the solution can be found in only 40 iterations of the algorithm.

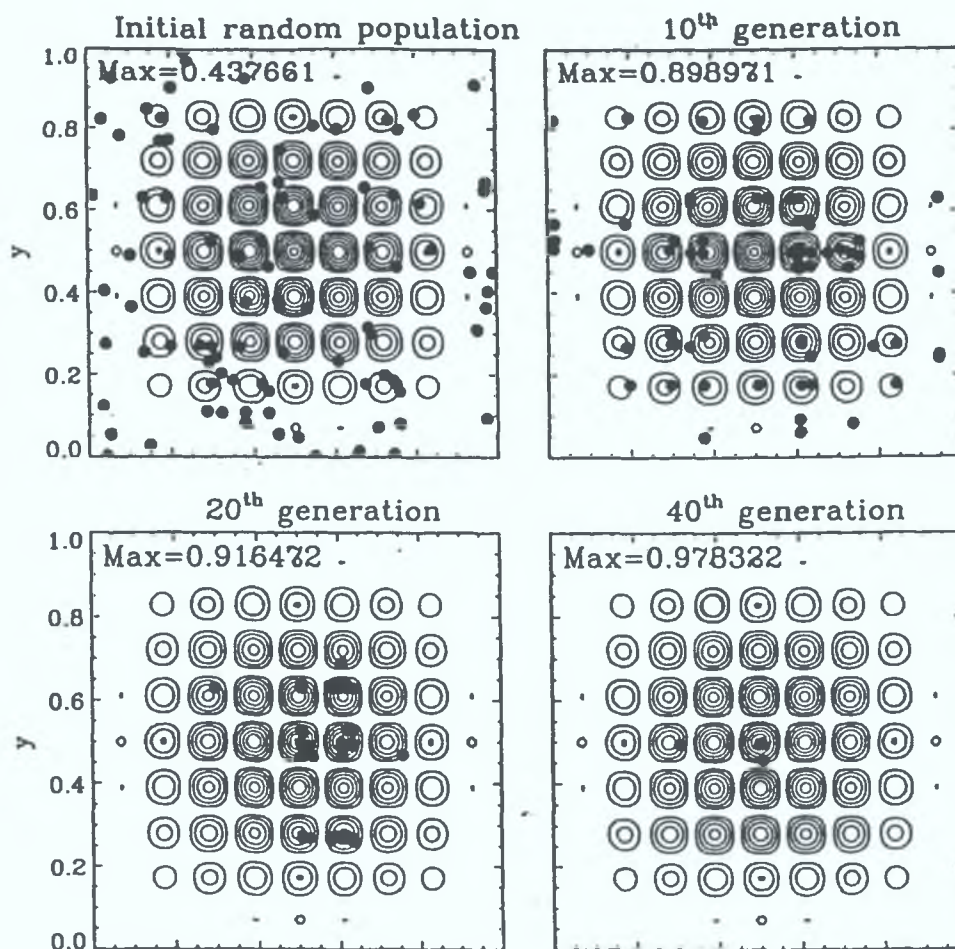


Figure 6.3

Other additional strategies and techniques may also be applied to reach convergence faster. These include [1];

Fitness Ranking

This reduces the effect of “inbreeding” within a population which causes subsequent populations to lose diversity. This is achieved by ranking the fitness of each member of the population. If for example one of the initial random population has a very good fitness, using normal methods it will breed with a considerable amount of the population to produce a secondary population of reduced diversity.

Elitism

This consists of copying, at least once, the fittest solutions to the next population.

Variable Mutation Rate

This is another useful method to decrease the chance of the population losing diversity. Once the difference in fitness between the median and fittest of the population falls below say 20% the mutation rate may be increased. This strategy should however be used in conjunction with elitism so as to avoid destroying the favorable solutions.

Reproduction plans

Two methods may be applied here, one is generational replacement which consists of a temporary population being produced and on completion this whole generation replaces the parent population. On the other hand steady-state reproduction may be employed, in this case as new members of the population are created they replace the parents immediately. With this method the choice of how these members are to be inserted also has to be made. The two most common methods are, direct replacement of the parent or replacement of the most unfit member of the population.

6.3 Directed evolution system

Directed evolution is a hybrid version of a classical genetic algorithm, its main advantage being that the necessity to encode the gene population is removed [2]. This method uses the normal floating point numbers needed by the problem to generate the solution. For the problem in equation 6.2 instead of encoding the (x, y) information

we directly use the x and y values in the population. Thus instead of having a population of say, $N = 100$, single genes we now have a population with each population member having the real x, y information. For a system of 100 genes and 10 variables the population will be as shown below,

$$\begin{bmatrix} x_{G_1, V_1} & \cdot & \cdot & x_{G_{100}, V_1} \\ \cdot & \cdot & \cdot & \cdot \\ \cdot & \cdot & \cdot & \cdot \\ x_{G_1, V_{10}} & \cdot & \cdot & x_{G_{100}, V_{10}} \end{bmatrix} \quad \text{E 6.2}$$

with the index (G_N, V_M) denoting the gene (G) number and the variable (V).

The other main difference between classical genetic algorithms and directed evolution is the adaptation of the breeding process. In directed evolution the crossover takes place between four members of the population. Each member in turn is selected and is crossed over with another vector (X'_c) which is made up of a combination of any three other randomly chosen vectors in the population. This vector is made up as follows, every pair of vectors (X_a, X_b) defines a vector differential i.e. $X_a - X_b$. When X_a and X_b are chosen randomly, their weighted difference can be used in place of Gaussian noise to perturb another vector X_c . This may be represented mathematically as follows,

$$X'_c = (X_a - X_b) \bullet F + X_c \quad \text{E 6.3}$$

The scaling factor F , is a user supplied constant [2].

The crossover coefficient (Cr) determines how the crossover takes place. Essentially the crossover coefficient is a number in the range 0-1 and a random number is chosen for each variable in the selected gene. If the randomly chosen number is less than the

crossover coefficient then crossover takes place. This scheme is represented mathematically below,

$$X_{final} = X_c \otimes X_{initial} \tag{E 6.4}$$

The only prerequisite is that the four genes chosen must be different. It may be also required that a random mutation take place in the child gene, this helps to keep the population diverse. The fitness of the vector, X_{final} , is calculated and compared to that of the initial population member, $X_{initial}$. The fitter of the two vectors is placed in the secondary population, and the other is discarded.

As a test of this system a lineshape was generated, which was the convolution of two Lorentzians and a Gaussian, as shown below,

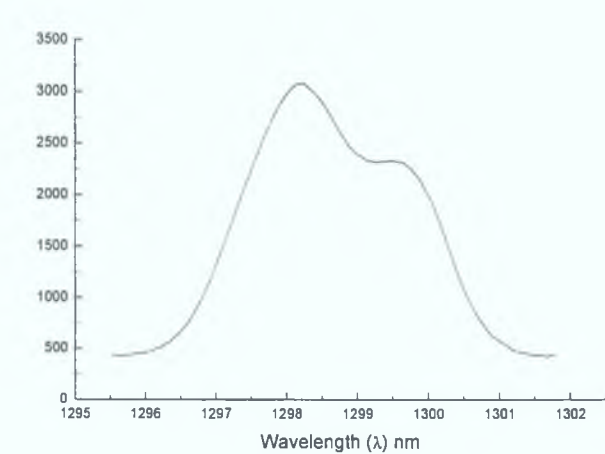


Figure 6.4

A directed evolution algorithm was generated to fit to this lineshape. As this lineshape was of a known form it was expected that the fitness of the solution from the genetic algorithm should be good. The genetic algorithm was run with a number of different values of Cr and f , the most efficient selection of these values was found to be

$Cr = 0.6$ and $f = 0.5$ Random mutation was not applied at this point. The plot below shows the best fitness in each population against the generation number.

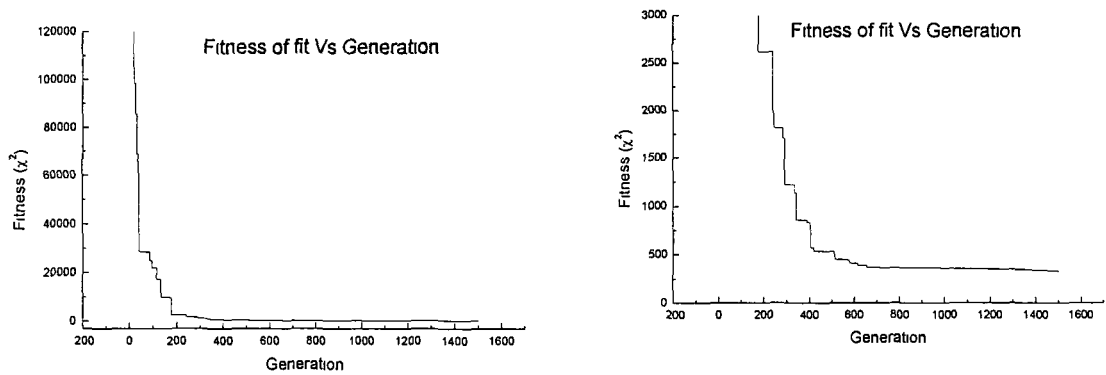


Figure 6.5 – Fitness is not normalised N = 100

The fitness was calculated as a $N\chi^2$ (chi squared), the smaller the fitness the closer the fitted curve is to the input data.

$$\chi^2 = \frac{\sum_N (\text{real data} - \text{fitted data})^2}{N}$$

E 6.5

As expected the algorithm quickly moves towards the minimum of the solution space and by 400 generations has reached a χ^2 of five but requires another 1200 generations to reach a χ^2 of 3. The graph below shows the fitted curve against the data for a χ^2 of 3 at 1600 generations.

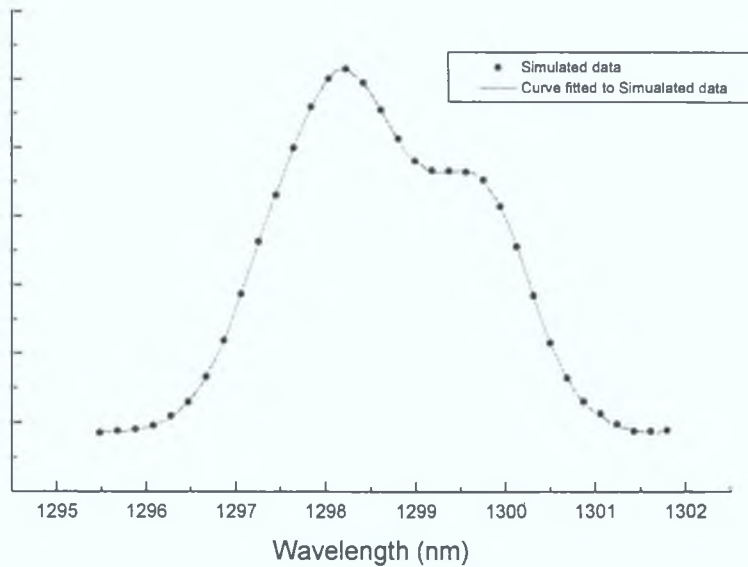


Figure 6.6

6.4 Using a Voigt function as the experimental lineshape

The Voigt function is widely used in the area of lineshape analysis. It can be generated by numerically by convolving a Lorentzian spectral lineshape with a Gaussian instrument function [3]. This method is numerically intensive and thus very time consuming, this type of computational work is normally only in the realm of high performance workstations. In recent years analytical approximations have been developed which have been proven to be efficient enough to make it possible to implement Voigt function generation on a standard desktop personal computer [4].

In papers by A.B. McLean et al [4] and A.W. Robinson et al [5] these techniques have been demonstrated. A similar technique was needed to fit to the convoluted Bragg grating data, the only difference being that in the case of the convoluted Bragg grating data the spectral lineshape was of a Gaussian form and the instrument, or interference filter in this case, was in the form of a Lorentzian.

For a Gaussian source of linewidth W_G (typically 0.37139 nm) and Lorentzian filter of straight through wavelength of λ_{\max} (typically 1308.5 nm) and linewidth W_L (= 2.537 nm) the transmission function is given by $1.866V(x, y)$. The Voigt function is given by,

$$V(x, y) = \sum_{i=1}^4 \frac{C_i(y - A_i) + D_i(x - B_i)}{(y - A_i)^2 + (x - B_i)^2} \tag{E 6.6}$$

and

$$y = \frac{W_L}{\sqrt{2}W_G}$$

$$x = \frac{2(1308.5) - 2\lambda_B - 2.6939 \times 10^{-6} N^2}{W_G \sqrt{2}} \tag{E 6.7}$$

where N is the number of stepping motor steps, λ_B is the Bragg wavelength and W_G is the Bragg linewidth. The coefficients (A_i, B_i, C_i, D_i) are given by the table below.

i	A_i	B_i	C_i	D_i
1	-1.2150	1.2359	-0.3085	0.0210
2	-1.3509	0.3786	0.5906	-1.1858
3	-1.2150	-1.2359	0.3085	-0.0210
4	-1.3509	-0.3786	-0.5906	1.1858

Table 6.1 – Parameters used to generate Voigt function [3]

This method was employed, in conjunction with the directed evolution technique shown above, to produce a fitting routine suited to the extraction of the Bragg wavelength λ_B and linewidth (W_G). An example of the spectrum returned from the system is shown in figure 6.7.

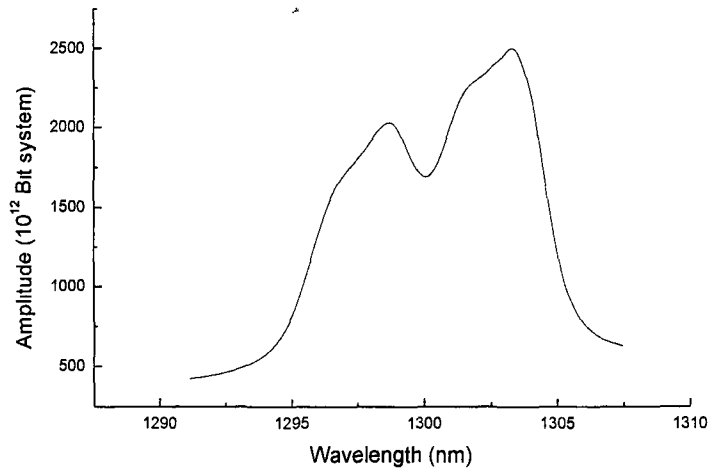


Figure 6 7

This data was passed to the fitting routine. The fitting routine was set to complete 1000 generations and returned a χ^2 of 11.75. The curve generated by the genetic algorithm is shown in figure 6 8.

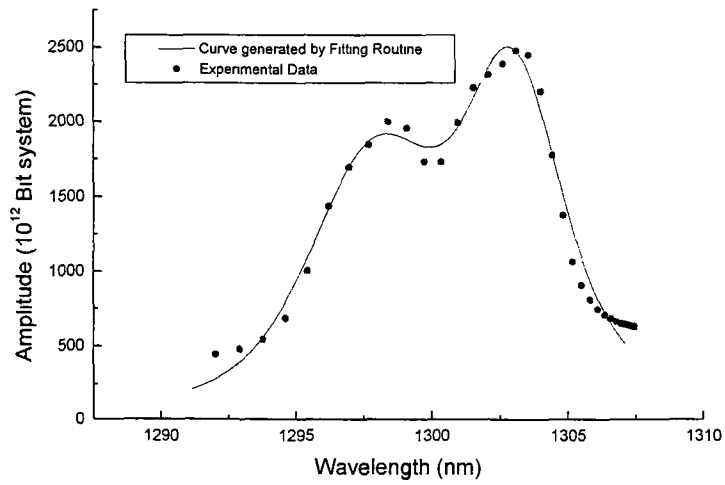


Figure 6 8

From the fitting routine the following data on the Bragg grating was extracted,

λ_{B_1} (nm)	W_{B_1} (nm)	λ_{B_2} (nm)	W_{B_2} (nm)
1304.19596	0.66903	1298.81241	0.52832

Table 6.2

6.5 Conclusion

It has been demonstrated that for a system such as that shown above which has a large number of variables, genetic algorithms can be a suitable solution. The basic genetic algorithm can allow a large solution space to be searched without the problem of finding a local minimum instead of the global minimum. This approach however does not guarantee to find the absolute solution, and it can be shown that even with the same input data, differing solutions can be found due to the random factor in the algorithm. However the solutions found are generally in such a small area of the solution space that they may be treated as the same.

The directed evolution approach allows us to disregard the problem of gene encoding from the genetic algorithm, and also improves on the efficiency of the overall system. It has been shown that this system has the ability to find solutions even in the ten variable problem in which it was tested. Like most genetic algorithms this technique approaches the solution quickly but as it attempts to find the solution in a smaller and smaller search space the convergence time increases. This may indicate that in some circumstances a normal fitting method may be employed after the genetic algorithm has found the basic area in which the solution lies.

The use of a Voigt function to fit to the experimental data, has proven to be very successful. The method, after adaptation, has proven to be fast and reliable thus reducing the time and complexity of numerically convolving the Lorentzian and Gaussian lineshapes.

The combination of these three operations has produced a successful and robust fitting system.

6.6 References

- [1] Charbonneau P., "Genetic algorithms in astronomy and astrophysics", The Astrophysical Journal Supplement Series, Vol 101 pg309-334 (1995).
- [2] Price K. and Storn R., "*Differential Evolution*", Dr. Dobbs Journal No. 264, Pg 18-24 (1997).
- [3] McLean A.B., Mitchell C.E.J. and Swanston D.M., "Implementation of an efficient analytical approximation to the Voigt function for photoemission lineshape analysis", Journal of Electron Spectroscopy, Vol 69 pg125-132 (1994).
- [4] Robinson A.W., Gardner P., Stampfl A.P.J, Martin R. and Nyberg G., "Error analysis in the fitting of photoemission lineshapes using the Levenberg-Marquardt method", Journal of Electron Spectroscopy, Manuscript version, July 1997.
- [5] Storn R., Price K., "Differential Evolution – A simple and efficient adaptive scheme for global optimization over continuous spaces", Technical Report TR-95-012 at ICSI, <ftp.icsi.berkeley.edu>, 1995.
- [6] Goldberg D.E., "*Genetic Algorithms in search, optimization and machine learning*", Addison-Wesley, 1989.
- [7] Press W.H., Teukolsky S.A., Vetterling W.T., and Flannery B.P., "*Numerical Recipes in C*", Cambridge University Press, 1992.
- [8] MacLeod H.A., "*Thin Film optical filters*", Hilger, Bristol U.K., 1985.
- [9] Voigt H.M., "Fuzzy Evolutionary Algorithms", Technical Report TR-92-038 at ICSI, <ftp.icsi.berkeley.edu>, 1992.

Chapter 7 Measurement of Strain and Strain Gradient using a pair of Bragg grating gauges

7.1 Introduction

Data on Bragg wavelength (λ_B) and Gaussian linewidth (W_G) are presented for a range of strain and strain gradients created on a cantilever strain rig. The variation of λ_B with both strain and temperature is quantified. The effect of strain gradient on linewidth is presented.

7.2 Calibration of cantilever using wire strain gauges

For any useable data to be extracted from the system it was important to calibrate the cantilever. The following method was used. Two wire strain gauges were used, the active one was bonded to the cantilever in the direction of the strain, the other, the dummy strain gauge, was attached perpendicular to the strain field so that it was not affected by it. This configuration was chosen because as in the case of the fibre strain gauges it allowed for the decoupling of the ambient temperature effects. This is achieved by having the active gauge sense the strain and temperature changes and the dummy gauge to sense only the temperature changes. A diagram of the half bridge configuration used is shown in figure 7.1.

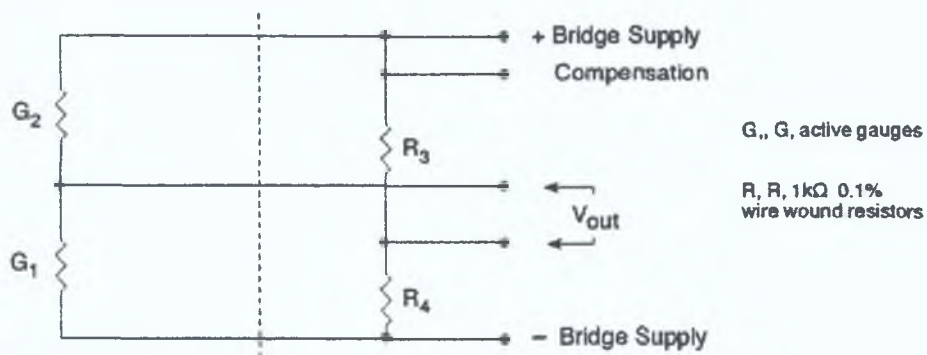


Figure 7.1

If the strain is ε then

$$\frac{\Delta R}{R} = g_s \varepsilon \quad \text{E 7.1}$$

where g_s is the gauge factor of the strain gauge. For a bridge of four equal resistors (R) powered by a supply of voltage of V_B .

$$\frac{\Delta V_B}{V_B} = \frac{\Delta R}{4R} = \frac{g_s \varepsilon}{4}$$

$$\therefore \varepsilon = \frac{4\Delta V_B}{g_s V_B} \quad \text{E 7.2}$$

It is important to note that the current drawn by the bridge circuit from the power supply must be kept to a minimum to prevent Joule heating of the strain gauges. A power of 8.25mW was dissipated in each of the 120 Ω (nominal) resistors in the bridge.

A standard strain gauge amplifier was employed (RS 435-692) which has a gain of 2000 therefore,

$$V_{out} = 2000(\Delta V_B) = \frac{(2000)V_B g_s \epsilon}{4} = 500 V_B g_s \epsilon$$

$$\epsilon = \frac{V_{out}}{500V_B g_s} \tag{E 7.3}$$

The wire strain gauges used were quoted as having a nominal gauge factor of 2.0 and the bridge voltage used was 1.992V. The theoretical strain of the cantilever was calculated using equation 5.12. A graph of strain versus cantilever deflection for both the wire strain gauge and cantilever formula is shown in figure 7.2.

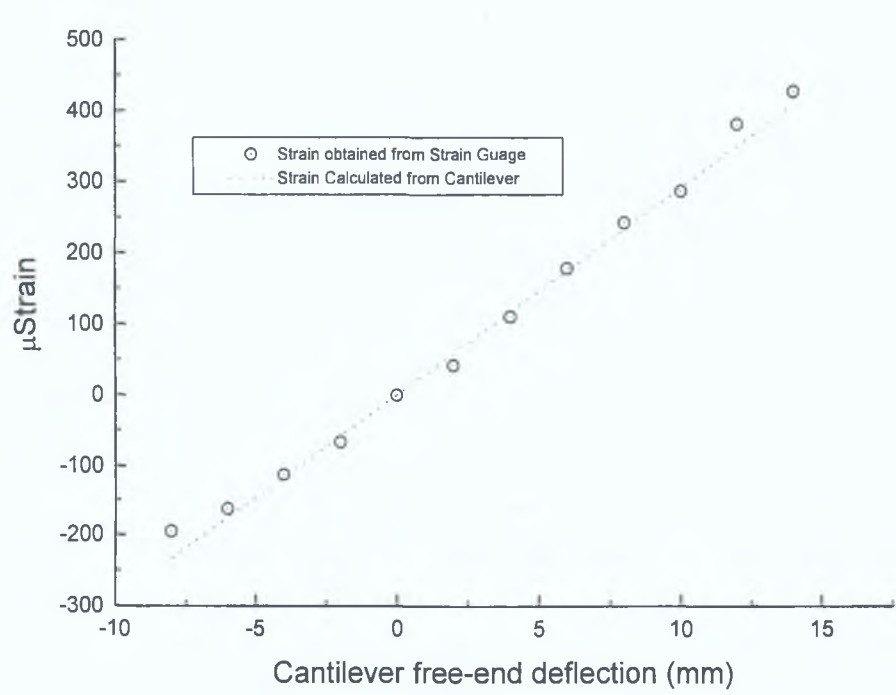


Figure 7.2

It can be seen that the two systems have a close correlation. If the strain for the wire strain gauge was plotted against the strain from the cantilever formula a straight line

of a slope of one should be obtained. This graph was drawn and is shown in figure 7.3.

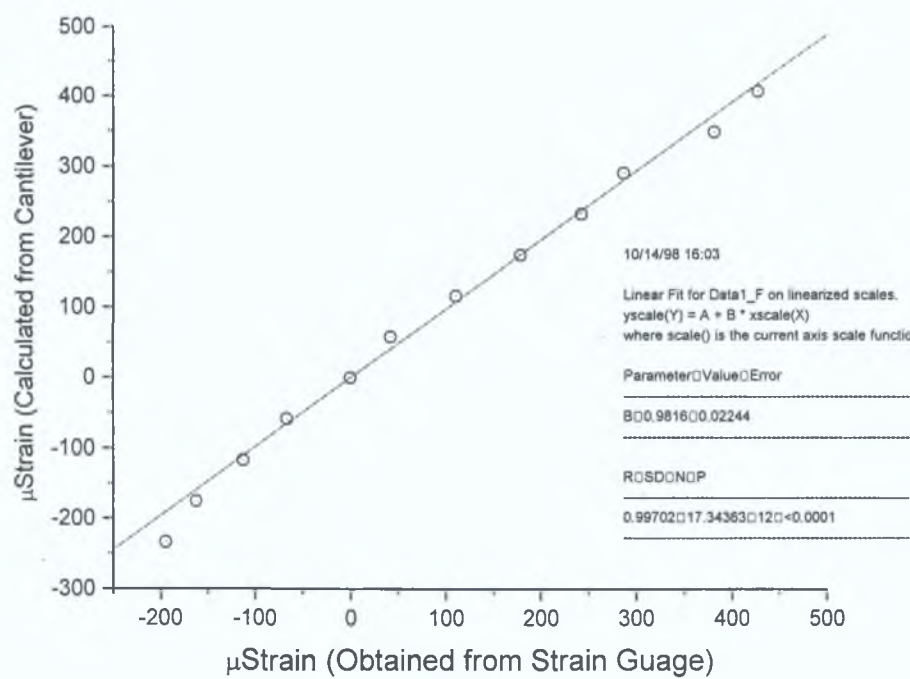


Figure 7.3

It can be seen that the calculated cantilever strain is ~2% smaller than the wire strain gauge estimate. As the wire strain gauge assumed a gauge factor of $g_s = 2.0$ it is probable that this is innacurate by a few percent. For example if $g_s = 2.05$ a slope of one is obtained, which is an exact correspondence between the two strain estimates. We may therefore assume that the cantilever equation is sufficiently accurate for the strain of the system.

7.3 Variation of Bragg wavelength with strain

Spectra of the back reflected light from the active and dummy Bragg gratings were recorded as a function of filter angle θ for a range of cantilever bending (i.e. strains) and deconvolved using the line fitting techniques to the Voigt profiles to extract the

line centers λ_{B1} and λ_{B2} . Multiple spectra at constant strain values were recorded and processed to yield an average value of λ_{B1} and λ_{B2} with a standard deviation of each mean of σ/\sqrt{n} , where σ is the standard deviation of the mean and n is the number of observations in each case.

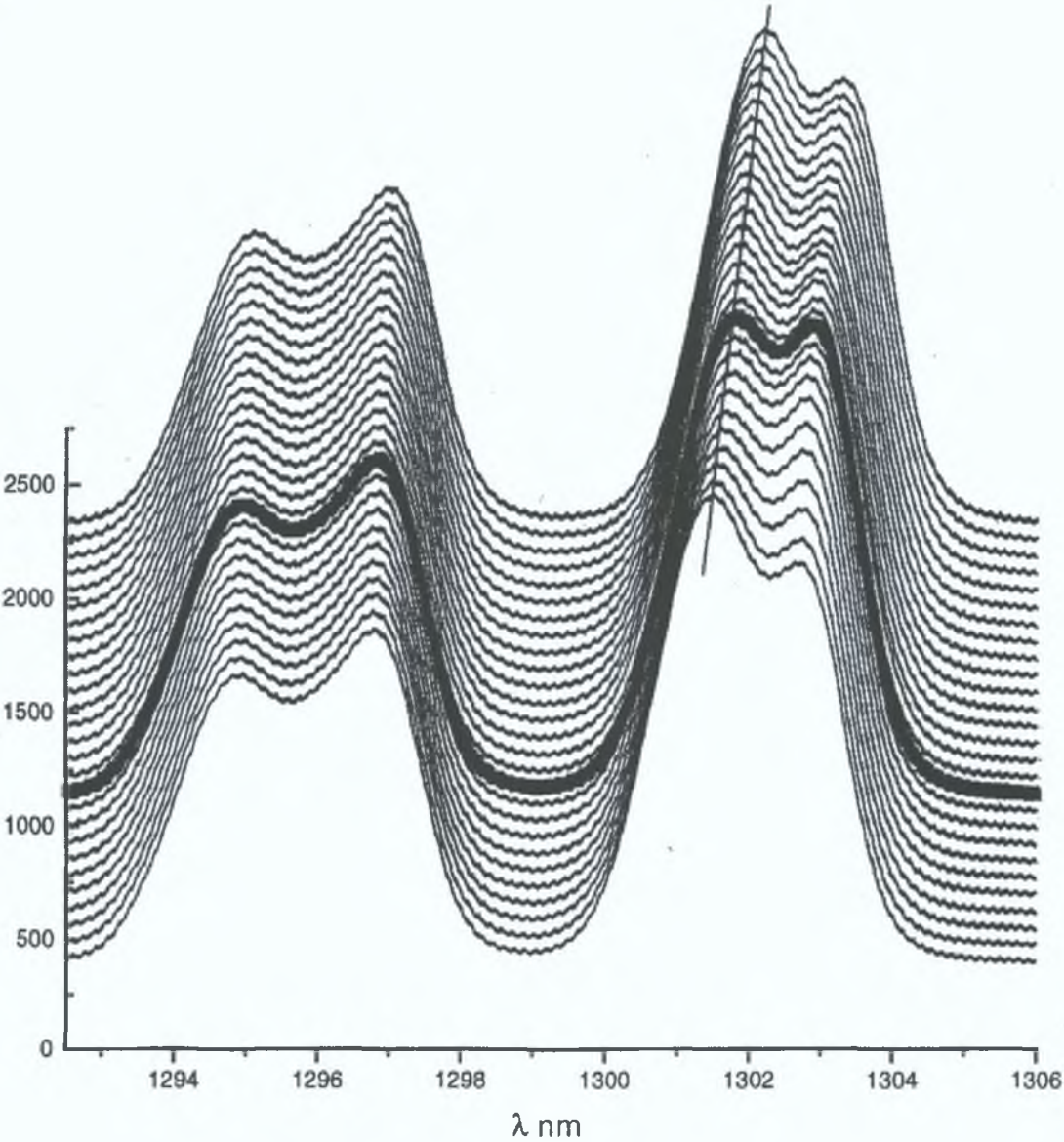


Figure 7.4

A set of spectra showing the shift in the active grating wavelength (at ~1302nm) and the constant value of the reference or dummy grating wavelength are shown in figure 7.4 as a function of the displacement of the cantilever free end. Compression ($\varepsilon < 0$)

and extension ($\varepsilon > 0$) are shown, the cantilever displacement between consecutive scans being constant. The differential wavelength shift $\delta\lambda$ between the active and dummy gauges is shown in figure 7.2.

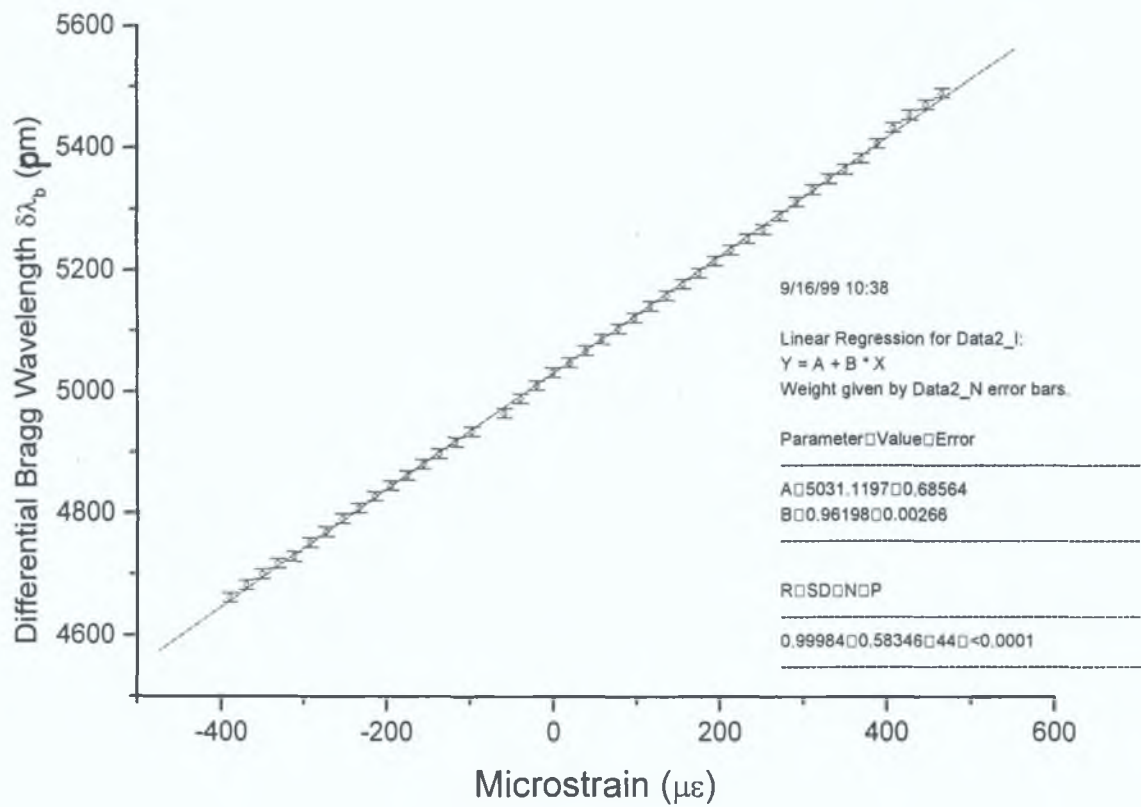


Figure 7.5

The vertical error bars are estimated to be

$$\pm 7.7\,pm$$

E 7.4

based upon the spread in the n estimates.

Cantilever free end displacement (mm)	Strain ($\mu\epsilon$)	λ_{B1} (nm)	W_1 (pm)	λ_{B2} (nm)	W_2 (pm)	$\delta(\lambda_{B1} - \lambda_{B2})$ (pm)
-12	466.82277	1298.36144	549.461	1303.85091	436.567	5489.472
-11.5	447.37182	1298.37998	550.431	1303.85038	437.0845	5470.406
-11	427.92087	1298.39327	550.118	1303.84665	436.8355	5453.383
-10.5	408.46992	1298.41804	549.6875	1303.85065	433.8305	5432.603
-10	389.01898	1298.44485	545.3235	1303.85151	429.7355	5406.656
-9.5	369.56803	1298.47599	543.693	1303.85853	426.805	5382.54
-9	350.11708	1298.50013	546.1395	1303.86521	425.6375	5365.083
-8.5	330.66613	1298.52173	527.7095	1303.87161	439.849	5349.88
-8	311.21518	1298.54799	560.855	1303.88025	431.525	5332.255
-7.5	291.76423	1298.57147	560.4265	1303.88367	430.2245	5312.197
-7	272.31328	1298.59879	560.511	1303.88847	427.067	5289.687
-6.5	252.86233	1298.62675	564.1635	1303.89407	425.338	5267.322
-6	233.41139	1298.64648	563.4465	1303.89819	426.2185	5251.718
-5.5	213.96044	1298.66882	568.5565	1303.90203	423.404	5233.21
-5	194.50949	1298.68551	569.054	1303.90056	422.647	5215.054
-4.5	175.05854	1298.70807	571.6505	1303.90369	421.4755	5195.624
-4	155.60759	1298.73171	575.108	1303.90917	420.995	5177.46
-3.5	136.15664	1298.7489	575.4425	1303.90731	419.579	5158.414
-3	116.70569	1298.767	579.497	1303.90849	420.101	5141.499
-2.5	97.25474	1298.79056	582.629	1303.91291	419.4025	5122.344
-2	77.8038	1298.80922	586.1595	1303.91337	417.703	5104.153
-1.5	58.35285	1298.82735	587.584	1303.91445	417.9295	5087.102
-1	38.9019	1298.84584	588.601	1303.91366	415.133	5067.823

-0.5	19 45095	1298 86587	592 2385	1303 91431	414 304	5048 448
0	0	1298 88424	596 538	1303 91659	414 9575	5032 351
0.5	-19 45095	1298 91038	598 5975	1303 92143	413 196	5011 047
1	-38 9019	1298 9318	598 172	1303 92076	410 2045	4988 955
1.5	-58 35285	1298 95655	597 529	1303 92145	408 6445	4964 899
2.5	-97 25474	1298 98961	609 4235	1303 92412	407 415	4934 506
3	-116 70569	1299 00875	611 769	1303 92554	407 8815	4916 79
3.5	-136 15664	1299 02894	614 325	1303 92661	406 4435	4897 672
4	-155 60759	1299 04781	619 4885	1303 92807	405 8995	4880 266
4.5	-175 05854	1299 06793	623 527	1303 92991	406 0345	4861 985
5	-194 50949	1299 08698	628 966	1303 93192	405 586	4844 934
5.5	-213 96044	1299 10622	633 58	1303 9339	405 7715	4827 682
6	-233 41139	1299 12635	636 5845	1303 93475	404 7695	4808 393
6.5	-252 86233	1299 14537	639 8705	1303 93677	404 179	4791 402
7	-272 31328	1299 16738	642 929	1303 9374	400 4945	4770 021
7.5	-291 76423	1299 18697	646 917	1303 93882	399 0205	4751 846
8	-311 21518	1299 20709	649 5575	1303 93604	404 124	4728 952
8.5	-330 66613	1299 22054	655 201	1303 93793	398 028	4717 384
9	-350 11708	1299 23989	659 7135	1303 94016	396 85	4700 263
9.5	-369 56803	1299 25979	666 121	1303 94219	396 188	4682 402
10	-389 01898	1299 28136	668 308	1303 94341	394 596	4662 053

Table 7.1

A least squares fit to the data yields a slope of $\frac{\delta\lambda_B}{\delta\varepsilon} = 0.96198 \pm 0.00266 \text{ pm}/\mu\varepsilon$,

from which $\frac{1}{\lambda_B} \left(\frac{\delta\lambda_B}{\delta\varepsilon} \right) = 0.740$ at $\lambda_B \approx 1300 \text{ nm}$

With an estimated resolution in wavelength of $\sim 7 \text{ pm}$ the corresponding resolution in strain is

$$\frac{7.7}{0.962} \cong 8 \mu\varepsilon \quad \text{E 7.5}$$

ie with the system used, strain can be determined optically over a -400 to $+600$ microstrain range with a resolution of approximately 8 microstrain. This resolution may be compared to the figure of Grooves-Kirby et al (1999) of one microstrain. This group use a set of 8 multiplexed Bragg gratings at $\sim 1550 \text{ nm}$ with a scanning Fabry-Perot filter demultiplexer.

7.4 Variation of Bragg wavelength with temperature

Using a constant temperature chamber with one Bragg grating located in it, the reference or dummy grating located outside the chamber at ambient temperature a range of reflection spectra were taken at a series of temperatures from 20 to 55°C . The variation of λ_B with temperature was found to be linear (see figure 7.8) with a slope of

$$\left(\frac{\partial\lambda_B}{\partial T} \right) = 8.47 \pm 0.2 \text{ pm}/^\circ \text{C}$$

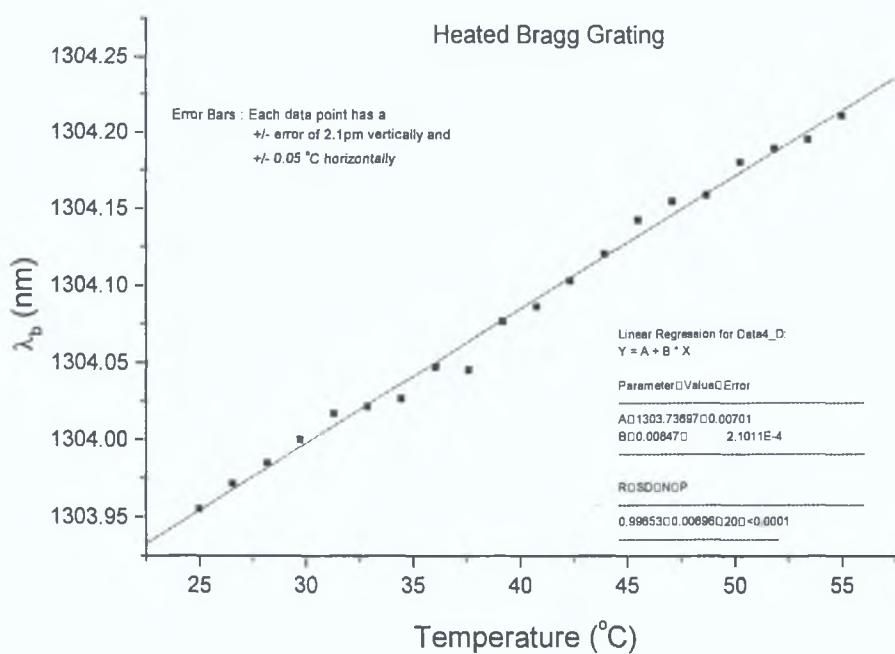


Figure 7.6

The data from which the graph is constructed is given in table 7.4.

Temperature in constant temperature environment	λ_{B1} (nm)	λ_{B2} (nm)	$\delta\lambda_B$ (nm)
25.0	1303.95533	1298.80459	5.15074
26.5	1303.97127	1298.80472	5.16655
28.1	1303.98487	1298.8162	5.16867
29.7	1303.99994	1298.81997	5.17997
31.3	1304.01718	1298.81466	5.20252
32.8	1304.02153	1298.81291	5.20862
34.4	1304.02656	1298.81232	5.21424
36.0	1304.0474	1298.8103	5.2371
37.6	1304.04539	1298.81383	5.23156

39.2	1304.07654	1298.81473	5.26181
40.7	1304.0863	1298.80795	5.27835
42.3	1304.10331	1298.81154	5.29177
43.9	1304.12064	1298.82003	5.30061
45.5	1304.1428	1298.81174	5.33106
47.1	1304.15513	1298.82219	5.33294
48.6	1304.15915	1298.82502	5.33413
50.2	1304.18079	1298.8235	5.35729
51.8	1304.18993	1298.82072	5.36921
53.4	1304.19596	1298.81241	5.38355
55.1	1304.21199	1298.82548	5.38651

Table 7.2

With a strain sensitivity of $\partial\lambda/\partial T \cong 8.5 \text{ pm}/^\circ\text{C}$ a temperature variation of 1°C creates a wavelength shift equivalent to that of a strain change of ~ 9 microstrain which in turn is about the system resolution (see equation 7.5).

7.5 Variation of linewidth with strain gradient

A series of spectra were taken for the grating on the cantilever with the active gauge exposed to a strain gradient (positive and negative of magnitude $-3ad/L_c^3$, as defined in equation 5.12) over a strain gradient range of approximately -1.0 to $+1.2 \text{ } \mu\epsilon/\text{mm}$. The Gaussian width W_G of the spectrum of the active grating was subtracted from the width of the reference grating to yield

$$\delta W = (W_G)_{\text{active}} - (W_G)_{\text{Reference}} \tag{E 7.6}$$

A graph of δW versus strain gradient was plotted; the data for this graph is shown in table 7.5.

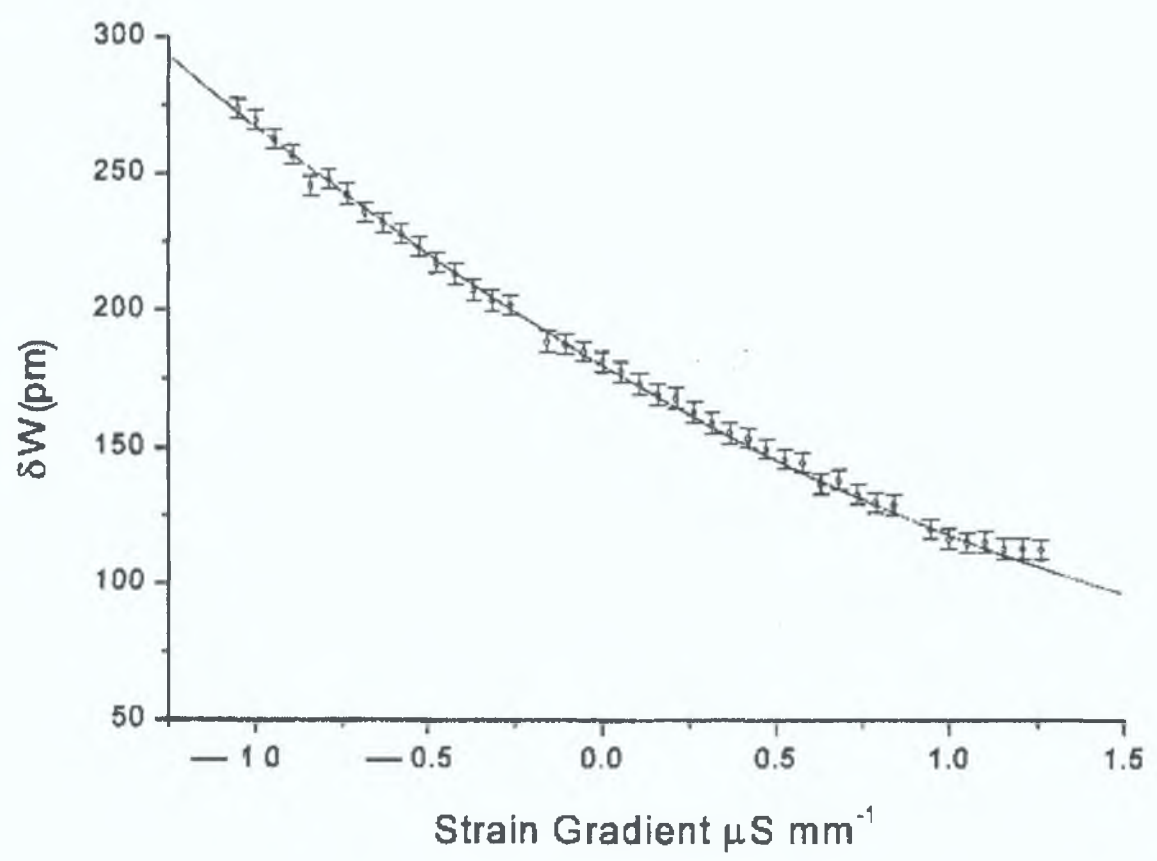


Figure 7.7

Cantilever free-end depression (mm)	W_{Active} (nm)	W_{ref} (nm)	δW (pm)
-12	0.43657	0.54946	112.894
-11.5	0.43708	0.55043	113.3465
-11	0.43684	0.55012	113.2825
-10.5	0.43383	0.54969	115.857

-10	0.42974	0.54532	115.588
-9.5	0.4268	0.54369	116.888
-9	0.42564	0.54614	120.502
-8.5	0.43985	0.52771	87.8605
-8	0.43152	0.56085	129.33
-7.5	0.43022	0.56043	130.202
-7	0.42707	0.56051	133.444
-6.5	0.42534	0.56416	138.8255
-6	0.42622	0.56345	137.228
-5.5	0.4234	0.56856	145.1525
-5	0.42265	0.56905	146.407
-4.5	0.42148	0.57165	150.175
-4	0.421	0.57511	154.113
-3.5	0.41958	0.57544	155.8635
-3	0.4201	0.5795	159.396
-2.5	0.4194	0.58263	163.2265
-2	0.4177	0.58616	168.4565
-1.5	0.41793	0.58758	169.6545
-1	0.41513	0.5886	173.468
-0.5	0.4143	0.59224	177.9345

0	0.41496	0.59654	181.5805
0.5	0.4132	0.5986	185.4015
1	0.4102	0.59817	187.9675
1.5	0.40864	0.59753	188.8845
2.5	0.40742	0.60942	202.0085
3	0.40788	0.61177	203.8875
3.5	0.40644	0.61433	207.8815
4	0.4059	0.61949	213.589
4.5	0.40603	0.62353	217.4925
5	0.40559	0.62897	223.38
5.5	0.40577	0.63358	227.8085
6	0.40477	0.63658	231.815
6.5	0.40418	0.63987	235.6915
7	0.40049	0.64293	242.4345
7.5	0.39902	0.64692	247.8965
8	0.40412	0.64956	245.4335
8.5	0.39803	0.6552	257.173
9	0.39685	0.65971	262.8635
9.5	0.39619	0.66612	269.933
10	0.3946	0.66831	273.712

Table 7.3

A second order polynomial was fitted to the data to give

$$\delta W = -74.486g + 12.519g^2 \quad \text{E 7.7}$$

, where g is expressed in microstrain per millimeter and δW is given in picometers.

7.6 Conclusion

The variation of the Bragg wavelength of a Gaussian apodised Bragg grating and its linewidth were measured as a function of both applied strain and strain gradient with ambient temperature compensation using a dummy grating.

7.7 References

- [1] Groves-Kirby C J , Wilson F J , Glynn G J , Henderson P , Jackson D A , Webb D J , Brennain J , Zhang L , Knight I , Latchen J and Woodward R ,
“Field-deployable system for structural health monitoring of concrete bridges using fiber Bragg grating sensors”, Institute of Physics meeting on In-Fibre Bragg Gratings and Special Fibres, 64 Portland Place, London 12th May (1999)

Chapter 8 Discussion of experimental results and conclusions

8.1 Introduction

The experimental results reported in chapter 7 are discussed in terms of published work of other groups and compared to the models developed in chapter 2.

8.2 Variation of Bragg wavelength with strain

Listed in table 8.1 are wavelength versus strain coefficients quoted by other groups at a selection of Bragg wavelengths from 780 to 1550nm in chronological order.

Experimental Group	Operating Bragg wavelength (nm)	$\frac{\delta\lambda_B}{\delta\epsilon}$ (pm / $\mu\epsilon$)	$\frac{1}{\lambda_B}\left(\frac{\delta\lambda_B}{\delta\epsilon}\right)$
Morley et al (1989)	830	0.64	0.77108
Morley et al (1991)	1550		0.74
Kalli et al (1991)	789	$0.585 \pm 3 \times 10^{-3}$	0.7414
Xu et al (1994a)	850	$0.59 \pm 3.4 \times 10^{-3}$	0.694
	1300	$0.96 \pm 6.5 \times 10^{-3}$	0.738
Xu et al (1994b)	1310	1.0287	0.785
Xu et al (1994c)	848	$0.59 \pm 3.45 \times 10^{-3}$	0.6957
	1298	$0.96 \pm 6.5 \times 10^{-3}$	0.7395

Arya et al (1995)	1550	1 2	0 774
Liu et al (1997)	827	0 64	0 7739
Brady et al (1997)	789	$0\ 603 \pm 26 \times 10^{-3}$	0 7642
This work	1300	$0.96198 \pm 2.66 \times 10^{-3}$	0.740

Table 8 1

Grouping the data in order of ascending wavelength the mean value of $\frac{1}{\lambda_B} \left(\frac{\delta \lambda_B}{\delta \epsilon} \right)$ are as follows,

λ_B (nm)	Mean Value of $\frac{1}{\lambda_B} \left(\frac{\delta \lambda_B}{\delta \epsilon} \right)$
~800	0 74926
~1300	0 75063
~1550	0 774

Table 8 2

These data points shown graphically in figure 7 3

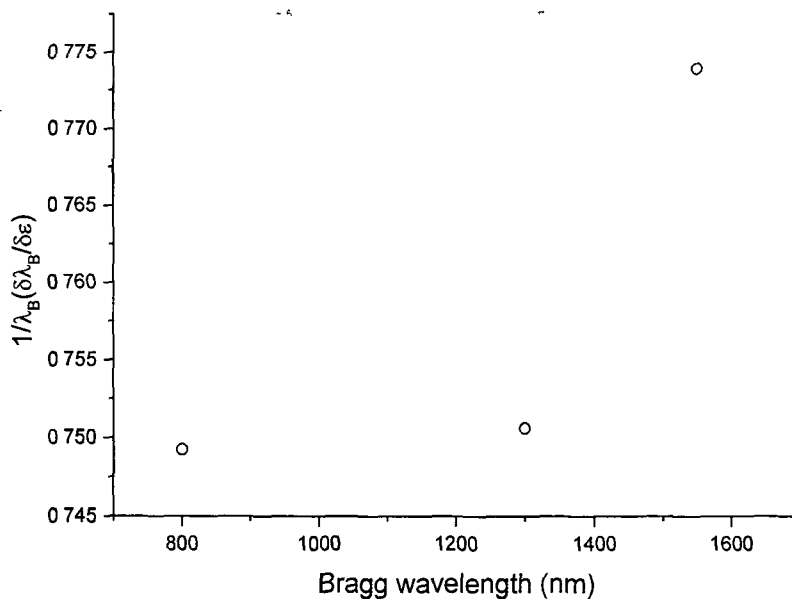


Figure 8.1

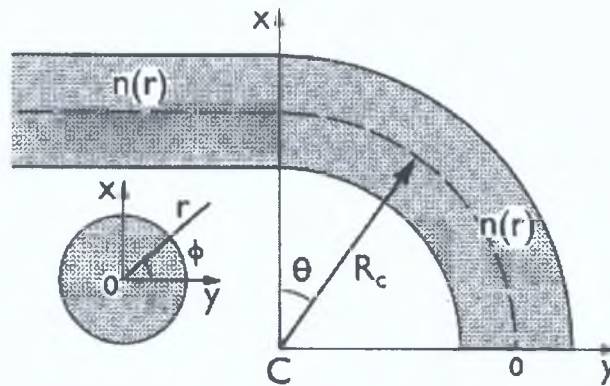
We saw in section 2.5.2 that

$$\frac{1}{\lambda_B} \left(\frac{\delta\lambda_B}{\delta\epsilon} \right) = 1 - p_e \quad \text{E 8.1}$$

where $p_e = \left(\frac{n^2}{2} \right) [p_{12} - \nu(p_{11} + p_{12})]$. From figure 8.1 it can be concluded that the coefficient p_e for silica glass decreases with increasing wavelength.

The measurements made of the Bragg wavelength of a fibre grating as a function of strain involved bonding of the fibre on a cantilever. Measurements were made of the Bragg wavelength of the active gauge as a function of curvature with the fibre resting on the bent cantilever but not epoxied to it. No wavelength shifts were detectable for the range of the curvature used. The radius of curvature of the cantilever ranged from ∞ to a minimum of approximately four metres.

As derived by Snyder and Love (1983) [12] the propagation constant of a mode in a fibre of bend radius R_c varies across the fibre cross section in (r, ϕ) , $\phi = 0$ is the plane of the fibre bend.



A fiber of refractive-index profile $n(r)$ is bent into an arc of constant radius R_c . Polar coordinates (r, ϕ) describe the fiber cross-section relative to 0, where the C0y-axis is parallel to the plane of the bend.

Figure 8.2 Snyder & Love Pg.706

The variation in β from its axial ($r = 0$) value $\hat{\beta}$ is given by them to be

$$\hat{\beta} \equiv \beta \left\{ 1 - \frac{r \cos \phi}{R_c} \right\} \quad \text{E 8.2}$$

Since $\beta = 2\pi n_{eff} / \lambda$ the variation of β across the core cross section is, at most,

$$\Delta \hat{\beta} \approx \frac{\beta a}{R_c} \quad \text{E 8.3}$$

,where a is the core radius. This equation then predicts a wavelength shift $\delta\lambda$ given

by

$$(\delta\lambda)_{\max} \approx \lambda_B \left(\frac{a}{R_c} \right) \quad \text{E 8.4}$$

For the system used $\lambda_B \sim 1300\text{nm}$, $a = 5 \times 10^{-6}\text{ m}$ and a cantilever radius of curvature of 4.01 meters minimum the predicted maximum wavelength shift is $\sim 1.5\text{pm}$. This is a factor of about five times smaller than the wavelength resolution of the measurement system used and accordingly any curvature effect was not detectable.

8.3 Variation of Bragg wavelength with temperature

Table 8.3 shows values of $(\partial\lambda_B/\partial T)$ and $1/\lambda_B (\partial\lambda_B/\partial T)$ quoted by various authors and the Bragg wavelengths at which the measurements were made. It can be seen that $1/\lambda_B (\partial\lambda_B/\partial T)$ decreases with increasing wavelength up to $\sim 1200\text{nm}$ and then begins to increase with increasing wavelength.

Experimental Group	Operating Bragg wavelength (nm)	$\frac{\delta\lambda_B}{\delta T}$ (pm/°C)	$\frac{1}{\lambda_B} \left(\frac{\delta\lambda_B}{\delta T} \right)$ °C ⁻¹ x10 ⁻⁶
Morley et al (1989)	830	6.8	8.193
Morley et al (1991)	1560	12.4	7.949
Kalli et al (1991)	789	$6.39 \pm 4.2 \times 10^{-2}$	8.10 ± 0.05
Xu et al (1994a)	850	$6.30 \pm 3.7 \times 10^{-2}$	7.41 ± 0.04
	1300	$8.72 \pm 7.7 \times 10^{-2}$	6.71 ± 0.06
Arya et al (1995)	1560	12.4	7.95
Liu et al (1997)	827	7.5	9.06

Brady et al (1997)	789	6.604 ± 0.031	8.37 ± 0.04
Kersey et al (1997)	1300	8.67	6.669
This work	1300	8.47	6.515

Table 8.3

The value of $1/\lambda_B (\partial \lambda_B / \partial T)$ is then $6.515 \pm 0.154 \times 10^{-6} \text{ } ^\circ\text{C}^{-1}$. This may be compared to a value of $6.67 \times 10^{-6} \text{ } ^\circ\text{C}^{-1}$ quoted by Kersey et al (1997).

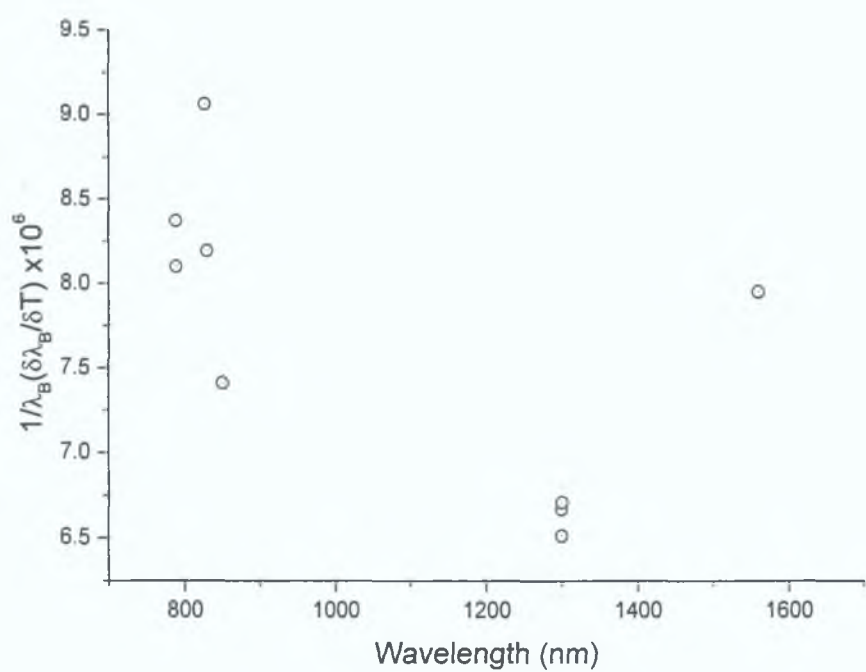


Figure 8.3

It appears that the temperature sensitivity of the Bragg wavelength reduces with increasing wavelength from 800 to 1300nm and then begins to increase with increasing wavelength.

8.4 Variation of linewidth with strain gradient

It was seen in figure 7.7 that the linewidth of the back reflected light as a function of strain could be fitted to a quadratic of the form

$$\delta\omega = A - Bg + Cg^2 \quad \text{E 8.5}$$

where A, B and C are positive constants. This is consistent with the model predictions of equation 2.78 for a Gaussian apodised grating.

These results may be compared to those of Huang et al (1995), the only published work on strain gradient that the author could locate. That group used a Gaussian apodised grating of 7mm length and apodisation coefficient $\alpha = 9 \times 10^4 \text{ m}^{-2}$. Their spectrum analyser has a resolution of 0.1nm (100 pm). Their strain gradients were about 30 times larger than used in this work and they found “the expected tendencies of wavelength broadening with increasing gradient in either a positive or negative direction”. In other words their spectrum broadening was independent of the polarity of the strain gradient g . This is in contrast to the results found in this work. The difference, it is felt, lies in the range of strain gradients measured. In the model predictions of equation 2.78 the linewidth will be dependant on g^2 rather than g when

$$\begin{aligned} B_2 g &\gg B_1 \\ \text{or } g &\gg \frac{B_1}{B_2} \end{aligned} \quad \text{E 8.6}$$

In our case the quadratic term will dominate for strain gradients much greater than about “six microstrain per millimeter”. This in fact smaller than the minimum strain gradient measured by Huang et al (1995). Obviously if the second term in equation 2.78 dominates the broadening will no longer reflect the polarity of the strain gradient as observed by that group. Huang et al postulated that “*The overall reflective spectrum (from tail to tail) $\Delta\lambda$ can be estimated as*”

$$\Delta\lambda \approx \lambda_B gL$$

This was based on eight measurements, four of positive strain gradient and four of negative strain gradient evenly spaced over the range -140 to $+140$ microstrain per millimeter. These strain gradients were approximately two orders of magnitude greater than used in this work but the measured resolution was 150pm or a factor of about 50 times larger than used here.

8.5 *Further Work*

The full system could provide more precision through the following improvements

- The use of an interference filter with a narrower linewidth would provide data that would be considerably less convoluted, making the necessary deconvolution less complicated and numerically intense.
- The rotation stage used provides step sizes of the order of 3.6×10^{-3} ; this could be improved by the use of a larger gearbox ratio. This would increase the time taken to scan across the two Bragg gratings and may prove to be unsuitable as the factors affecting the gratings may change during a single scan, thus reducing the reliability of the system.
- The software written to control the system and deconvolute the data was written with a DOS interface. This makes it user unfriendly in this age of graphical user interfaces (GUI) such as Microsoft Windows or Unix. A simpler interface may be obtained if the code was written for a windowed operating system. This leads to many complications such as “*interrupt use*” (stopping all computer operations to execute each step of the rotation) to control the speed of the rotation stage, which would make the software much

more, complicated and time consuming to write, thus it was beyond the scope of this work.

The sensitivity of a Bragg grating to temperature as well as strain suggests that the linewidth of a back reflected spectrum should vary with a temperature gradient along the grating. It should be possible to measure such a temperature gradient in an analogous fashion to the strain gradient work reported here. This is hoped to form the basis of future work.

8.6 Global Conclusion

An innovative spectrum analyzer based upon a rotating Fabry Perot interference filter with a variable instrument function was used in analysing the spectrum of light back reflected from in fibre Bragg gratings. Curve fitting using genetic algorithms was used to extract spectral information, line positions and linewidths. Wavelength resolutions of approximately 7pm were achieved. The spectral line center locations were correlated to the strain across the grating and the linewidths were identified with the strain gradients across the Bragg gratings. For the mean strain measurement a strain sensitivity of $0.96198 \pm 0.00266 \text{ pm} / \mu\epsilon$ was measured – over a range of approximately –400 to +450 microstrain. A temperature sensitivity of $8.47 \pm 0.2 \text{ pm} / ^\circ\text{C}$ - over a range of +20 to +55 $^\circ\text{C}$ - was observed. These sensitivity values are consistent with published work. Linewidth was found to follow a second order polynomial in strain gradient. This was in agreement with a model developed in chapter 2 for a Gaussian apodised grating exposed to a strain field. The latter work has only been briefly mentioned in the literature and our model predictions may be interpreted to explain the albeit few observations of another group.

8.7 References

- [1] Morley W.W., Meltz G and Glenn W.H., "Fiber optic Bragg grating sensors", Proc. S.P.I.E. Vol 1169, pg 98-107 (1989)
- [2] Kersey A.D., Berkoff T.A. and Morley W.W., "Fiber optic Bragg grating strain sensor with drift compensated high resolution interferometric wavelength shift detection", Optics Letters Vol 18 No. 1, Pg 72-74 (1993)
- [3] Xu M.G., Archanbault L, Reekie L and Dakin J.P. "Discrimination between strain and temperature effects using dual wavelength fibre grating sensors." Electronics Letters Vol 30 No. 13, Pg 1085-1087 (1994a)
- [4] Xu M.G., Archanbault L, Reekie L and Dakin J.P. "Thermally compensated bending guage using surface mounted fibre gratings", International Journal of Optoelectronics Vol 9 No. 3, Pg 281-283 (1994b)
- [5] Xu M.G., Archanbault L, Reekie L and Dakin J.P. "Simultaneous measurement of strain and temperature using fibre grating sensors", Tenth International Conference on Optical Fibre Sensors, Glasgow Scotland, Oct 1994 (1994c)
- [6] Arya V, Sherrer W, Wang A and Claus R.O., "Temperature compensated scheme for refractive index grating based optical fiber devices", Proceedings S.P.I.E., International Society Optical Engineers, U.S.A. Vol 2594, Pg 52-59, Self calibrated intellegent optical sensors and systems, Philadelphia Oct (1995)
- [7] Kalli K., Brady G., Webb D.J., Jackson D.A., Reekie L and Archambault L., "Possible approach for the simultaneous measurement of temperature and

- strain via first and second order diffraction from Bragg grating sensors”,
S P I E Vol 2507, Pg 190-198, Munich (1995)
- [8] Liu T , Fernando G F , Rao Y J , Jackson D A , Zhang L and Benmian I ,
“Simultaneous strain and temperature measurements in composites using a
multiplexed fibre Bragg grating sensor and extrinsic Fabry-Perot sensor”,
Institute of Physics meeting on Bragg gratings and Special Fibres, London
(1997)
- [9] Brady G P , Kalli K , Webb D J , Jackson D A , Reekie L and Archambault
J L , “Simultaneous measurement of strain and temperature using the first and
second order diffraction wavelengths of Bragg gratings”, I E E Proceedings –
Optoelectronics Vol 144 No 3, Pg 156-161 (1997)
- [10] Morley W W , Dunphy J R and Meltz G , Proceedings Society Photo-optic
Instrument Engineers Vol 1586, Pg 216 (1991)
- [11] Kersey A D , Davis M A , Patrick H J , LeBlanc M , Koo K P , Askins C J ,
Putnam M A and Friebele E J , “Fiber grating sensors”, Journal of Lightwave
Technology Vol 15 No 8, Pg 1442-1463 (aug 1997)
- [12] Snyder A W , Love J D , “*Optical Waveguide Theory*”, Chapman and Hall,
London (1983), Section 36-14
- [13] Huang S , LeBlanc M , Ohn M M and Measures R M , “Bragg intragrating
structural sensing”, Applied Optics No 34 pg5003-5009 (1995)

Appendix A

A.1 *Hyperbolic functions of complex variables*

$$\begin{aligned}\sinh(A + iB) &= \sinh(A) \cdot \cos(B) + i \cosh(A) \cdot \sin(B) \\ \cosh(A + iB) &= \cosh(A) \cdot \cos(B) + i \sinh(A) \cdot \sin(B)\end{aligned}$$

A.2 *Inverse trigonometric functions*

The FORTRAN function

$$\text{DANTAN2(R1,R2)}$$

calculates the function $\arctan(R1/R2)$, taking into account the polarity of the complex numbers R1 and R2 i.e. in what quadrant of the complex plane in which each resides.

A.3 *Useful complex number relations*

If $z = r \cdot \exp(i\theta)$ is a complex number with real part x and imaginary part y then

\sqrt{z} is given by

$$\sqrt{r} \cdot [\cos(\theta/2) + i \sin(\theta/2)], \quad \text{where} \quad \tan(\theta) = y/x.$$

$$\sqrt{-i} = (1 - i) / \sqrt{2}$$

Appendix B System Specification Sheets

B.1 Fibre Specifications

Fiber Bragg Grating
DATA SHEET

Grating type	FBGCP-1300/1305-90-0.5	
Grating number	TEC-7198-1	
Center wavelength (nm)	1300.3	1305.2
Bandwidth (nm)	0.47	0.48
Reflectivity (%)	99.0	99.0
Fiber color	Blue	Bare
Fiber type	SMF-28	
Fiber pigtails (m)	2 m from coupler, >1 m from fiber end	




TECOS™

Telecommunication
Systems GmbH

Scheibenstraße 47 • D-40475 Düsseldorf/Germany
Tel.: +49-211-49258-0 • Fax: +49-211-49258-10
E-mail: TECOS@t-online.de • Internet: <http://www.tecos.de>

Verified by:


Bernard Malo
V.P. Production



**ETX 500T, ETX 1000T
ETX 2000T5, ETX 3000T5**

Large Area InGaAs Photodiodes

Features

- High responsivity at 1300, 1550, and 850 nm.
- Low dark current for high accuracy
- High shunt resistance for low noise
- Linear over wide range of input optical power
- 0.5, 1, 2, and 3 mm active diameters

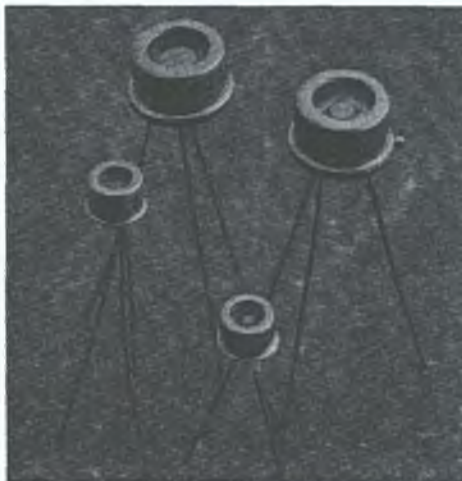
Applications

- Optical power meters
- Optical fiber identifiers
- Optical attenuation test sets
- Near infrared spectroscopy
- Infrared rangefinders

Description

The EPITAXX series of large area Indium Gallium Arsenide (InGaAs) photodetectors consists of PIN diodes that have photosensitive areas with diameters of 500 μm , 1000 μm , 2000 μm , and 3000 μm . These photodiodes have high spectral responsivity in the near infrared range, between 800 and 1700 nanometers. They are designed with large active areas so they can be used for instrumentation, sensing and rangefinding applications.

These detectors feature high sensitivity to low level signals and spectral responsivity that is linear over a wide dynamic range of input optical power. In an unbiased mode, these large area photodiodes have high sensitivity because InGaAs exhibits higher shunt resistance than other near infrared detection materials. When reverse biased for greater bandwidth, their sensitivity stems from the diodes' low dark current. Since shunt resistance decreases and dark current increases with junction area, the smallest area ETX 500T has the highest sensitivity (lowest noise current density): at room temperature, 10 fA/Hz^{1/2} at 0V and 60 fA/Hz^{1/2} at -5V are typical. Highly linear spectral response results from the low series resistance of the large area photodiodes. For the ETX 3000T5, linearity is typically $\pm 0.15\text{dB}$ to $+7\text{dBm}$.



EPITAXX large area detectors are recommended for near infrared instrumentation applications that require low photodiode noise. The ETX 500T and ETX 1000T are well suited for high speed, differential mode measurements. Such measurements are common in precision optical power meters, optical fiber identifiers, and optical loss test sets. The ETX 2000T5 and ETX 3000T5 are optimal for field instruments, as the diodes' large diameters simplify coupling incident radiation into their photosensitive areas. These instruments include attenuation sets and the above mentioned meters and identifiers. In addition, the high linearity of the ETX 2000T5 and ETX 3000T5 makes these detectors appropriate for measuring signals that vary over a wide dynamic range. Such signals are frequent in local area networks and in high fan-out systems.

The ETX 500T and ETX 1000T are available in a single grade. There are two grades of ETX 2000T5 and ETX 3000T5: the economical J Grade and the standard K Grade, which has a higher shunt resistance. The package for the ETX 500T and ETX 1000T is a hermetically sealed TO-46 can; the ETX 2000T5 and ETX 3000T5 are packaged in hermetically sealed TO-5 cans. All EPITAXX large area photodiodes are also available mounted on standard or custom ceramic subcarriers.

Specifications

MODEL	ETX 500T			ETX 1000T			ETX 2000T5			ETX 3000T5			Units
Conditions (unless noted)	25°C, $V_R = 5V$			25°C, $V_R = 5V$			25°C, $V_R = 0V$			25°C, $V_R = 0V$			
Parameter	Min.	Typ.	Max.	Min.	Typ.	Max.	Min.	Typ.	Max.	Min.	Typ.	Max.	
Active Diameter		0.5			1.0			2.0			3.0		mm
Responsivity @ 850 nm	0.10	0.20		0.10	0.20		0.10	0.20		0.10	0.20		A/W
Responsivity @ 1300 nm	0.80	0.90		0.80	0.90		0.80	0.90		0.80	0.90		A/W
Responsivity @ 1550 nm		0.95			0.95			0.95			0.95		A/W
Dark Current ¹		12	100		50	400		900			2000		nA
Shunt Resistance ²													
J (Economy)	5.0	250		2.0	50		0.8	3.0		0.1	0.4		MΩ
K (Standard)							10	25		1.0	10.0		MΩ
Linearity ³		± 0.15			± 0.15			± 0.15			± 0.15		dB
Total Capacitance ⁴		35	50		100	150		400	600		800	1300	pF
Bandwidth ⁵		140			35			5.3			2.6		MHz

Notes: 1) $V_R = 1V$ for ETX 2000T5 and ETX 3000T5
2) $V_R = 10\text{ mV}$
3) For ETX 500T and ETX 1000T, to +9 dBm;
for ETX 2000T5 and ETX 3000T5, to +7 dBm
4) For ETX 500T and ETX 1000T, $V_R = 0\text{ V}$
5) -3dB point into a 50Ω load

Maximum Ratings

MODEL	ETX 500T		ETX 1000T		ETX 2000T5		ETX 3000T5		Units
Reverse Voltage	20		20		2		2		V
Reverse Current ^A	10		10		10		10		mA
Forward Current ^B	10		10		10		10		mA
Power Dissipation	100		100		50		50		mW
Operating Temperature	-40	+85	-40	+85	-40	+85	-40	+85	°C
Storage Temperature	-40	+85	-40	+85	-40	+85	-40	+85	°C

Notes: A) Under reverse bias, current at which device may be damaged.
B) Under forward bias, current at which device may be damaged.

Figure 1

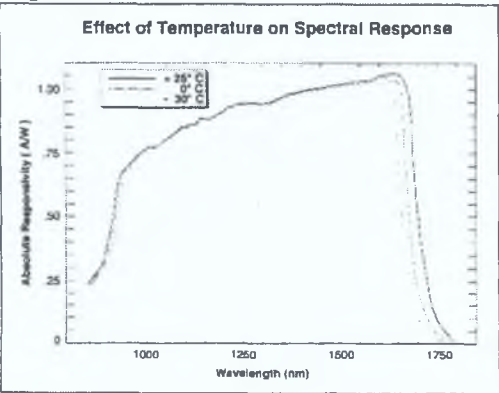


Figure 2

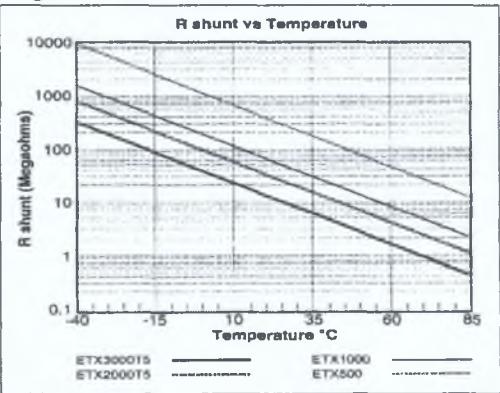


Figure 3

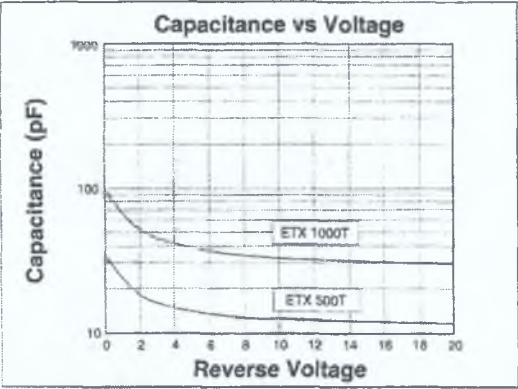


Figure 4

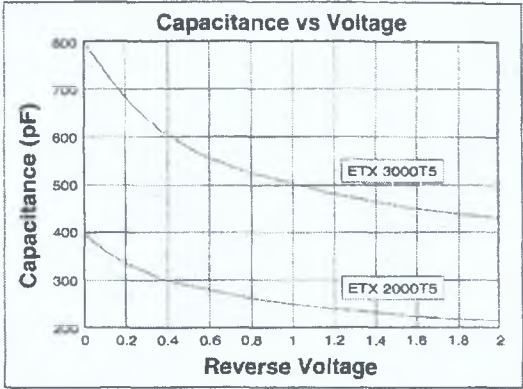


Figure 5

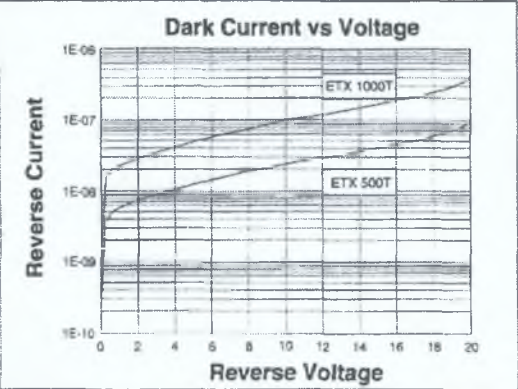


Figure 6

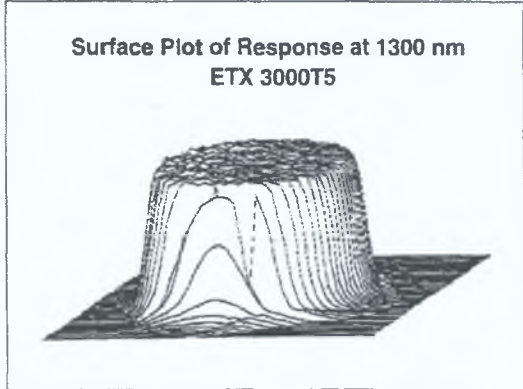
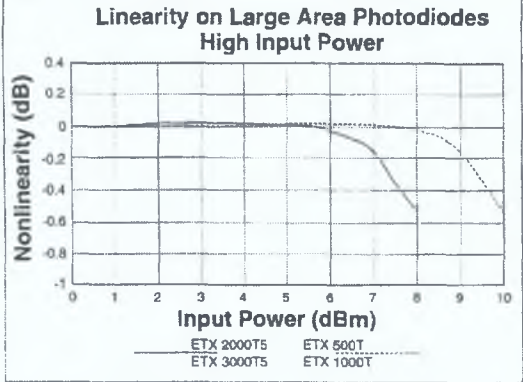
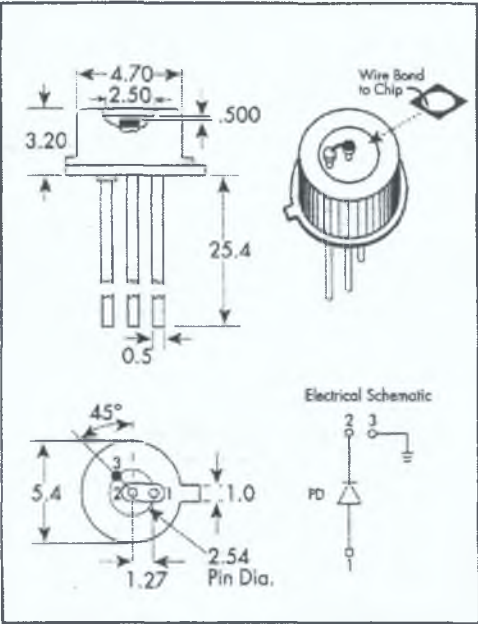


Figure 7

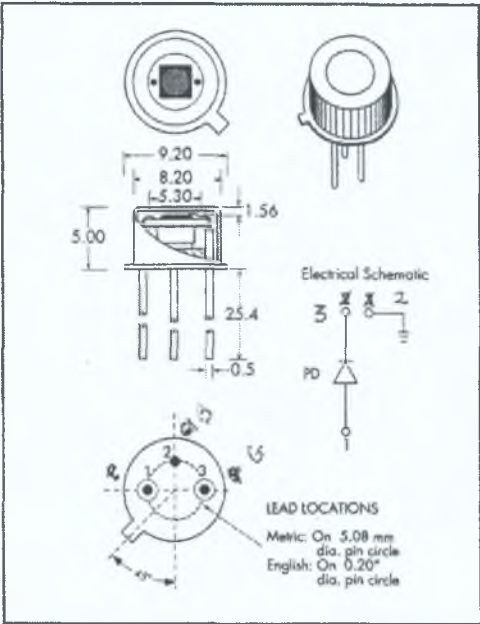


Mechanical Dimensions

ETX 500T, ETX 1000T
All dimensions in mm



ETX 2000T5, ETX 3000T5
All dimensions in mm



EPITAXX, Inc. believes the information contained in this document to be accurate. However, no responsibility is assumed for its use nor for any infringement of the rights of third parties. EPITAXX, Inc. reserves the right to introduce changes without notice.



Corporate Headquarters
7 Graphics Drive • West Trenton, NJ 08628
TEL (609) 538-1800 • FAX (609) 538-1684

West Coast Sales Office
2121 Avenue of the Stars, 6th Floor • Los Angeles, CA 90067
TEL (310) 551-6507 • FAX (310) 551-6577

B.3 ELED



**ETX 1300RFC, ETX 1300RST
ETX 1300FJ, ETX 1300FC**

1300 nm High Power ELED Modules

Features

- High coupled power (75 μ W typical into multimode)
- High speed response (3.5 ns typical)
- Narrow emission spectrum (60 nm typ.)
- Singlemode and multimode versions

RFC/RST Series:

- Receptacle mount for FC and ST

FJ/FC Series:

- Compact coaxial package
- Wide choice of fiber pigtails

Applications

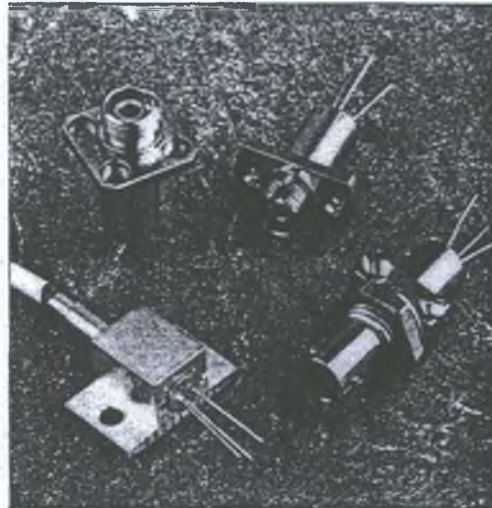
- Fiber optic transmitters for medium to low data rates and distances
- Light sources for test and measurement instrumentation

Description

EPITAXX 1300 nm high power ELED modules are edge-emitting LEDs made of Indium Gallium Arsenide Phosphide (InGaAsP). The modules are optically terminated with a permanent coaxial pigtail or within an FC or ST receptacle that can be mated repeatedly with its complementary connector.

These ELED modules provide high coupled power into singlemode or multimode fiber. The LEDs have fast response and a narrow emission spectrum. Each module configuration provides high performance and reliability, as the diodes are hermetically sealed in TO-18 cans.

For applications demanding more power than surface-emitting LEDs provide, but requiring components less expensive than injection laser diodes, EPITAXX ELED modules offer an economical solution. Common to such applications are optical links that span short to moderate distances and transmission systems operating to 200 Mbps. Examples include local area networks, video surveillance systems, and point-to-point communication links. In such applications, these modules offer a cost effective, high performance solution.



Two grades of EPITAXX ELED modules are available: the economy J grade and the standard K grade, which has higher coupled power. Modules are available in fiber optic receptacles and in pigtailed versions.

Standard receptacle choices are FC connectors (RFC) and ST connectors (RST). DIN and other special connector receptacle versions are available by special order. When ordering a pigtailed version, the customer can select between a jacketed fiber pigtail (FJ) and a cabled fiber pigtail (FC). The customer can also designate the pigtail to be singlemode or multimode. Standard fiber sizes are 8.7/125 μ m (SM) and 50/125 μ m (MM). In addition, other fiber pigtails are available by special order. All pigtailed versions are available with any industry standard connector termination.

Specifications

Model	ETX 1300RFC RST			ETX 1300FJ-M			ETX 1300FJ-S			
Parameter	Min.	Typ.	Max.	Min.	Typ.	Max.	Min.	Typ.	Max.	Units
Fiber Type	(8.7/125 SM)			(50/125 MM)			(8.7/125 SM)			μm
Optical Power										
J (Economy)	8	15		35	75		8	15		μW
K (Standard)	20	30 ¹					20	30		μW
Forward Voltage ²		1.5	2		1.5	2		1.5	2	V
Peak Wavelength	1270	1300	1330	1270	1300	1330	1270	1300	1330	nm
Spectral FWHM		60	100		60	100		60	100	nm
Rise Time ³		2.5	5		2.5	5		2.5	5	nS
Fall Time ³		3.5	5		3.5	5		3.5	5	nS
Cutoff Frequency ⁴		150			150			150		MHz
Wavel. Temp. Coeff.		+0.7			+0.7			+0.7		nm/°C

Maximum Ratings

Model	ETX 1300RFC,RST	ETX 1300FJ-M	ETX 1300FJ-S	Units
Parameter				
Coupled Power ⁵	100	250	100	μW
Reverse Voltage	1	1	1	V
Forward Current	150	150	150	mA
Operating Temp.	-20 /+65	-20 /+65	-20 /+65	°C
Storage Temp.	-40 / +85	-40 / +85	-40 / +85	°C

Notes:

All data at 25°C, unless noted.

1) For singlemode. With multimode, Min.=50 μW, Typ. = 80 μW.

No J-grade ETX1300Rxx available for multimode.

2) @ I_f = 100 mA.

3) R_s = 50 Ω.

4) I_f = 100 mA + 20 mA p-p, -1.5 dB point.

5) Or I_f = 150 mA, whichever occurs first.

Figure 1

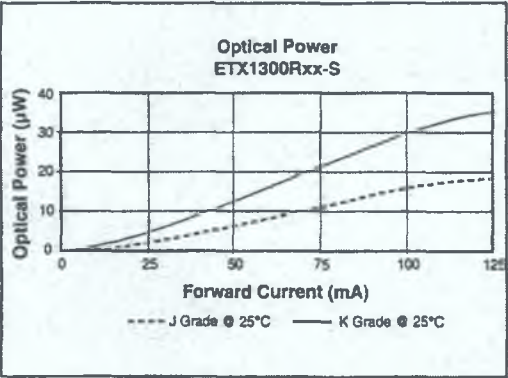


Figure 2

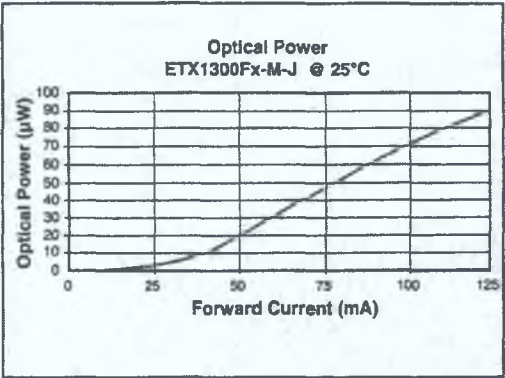


Figure 3

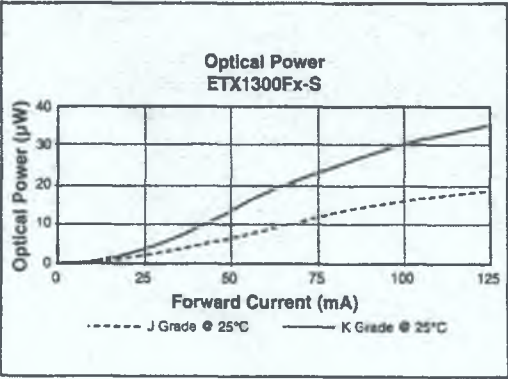


Figure 4

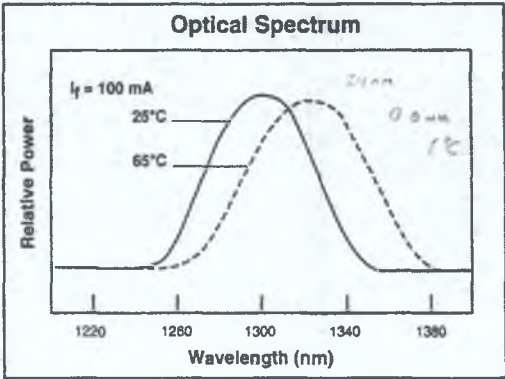


Figure 5

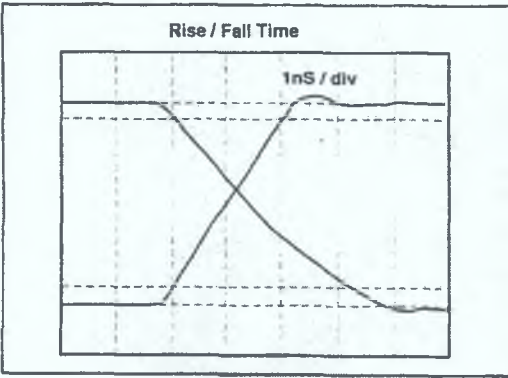
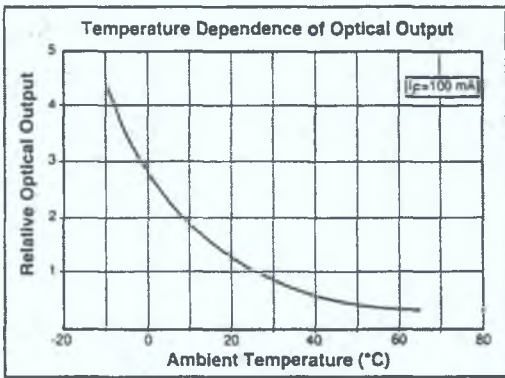


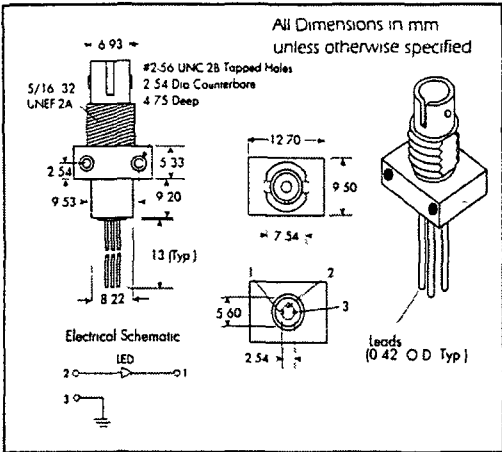
Figure 6



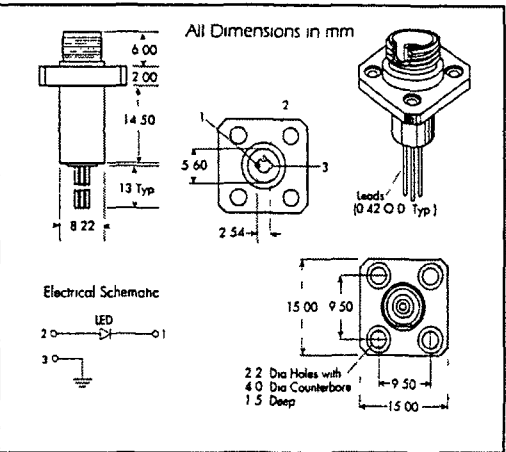
1300 nm High Power ELED Modules

ETX 1300RFC ETX 1300RST, ETX 1300FJ, ETX 1300FC

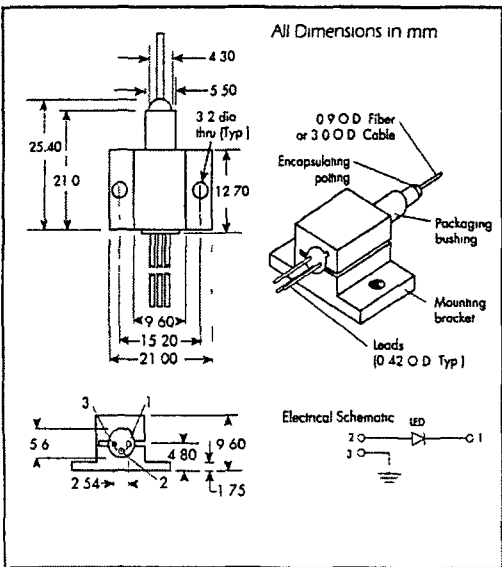
ETX 1300RST



ETX 1300RFC



ETX 1300FJ-S, FJ-M ETX 1300FC-M, FC-S



B.4 Electronics

B.4.1 Photodiode Amplifier Circuit

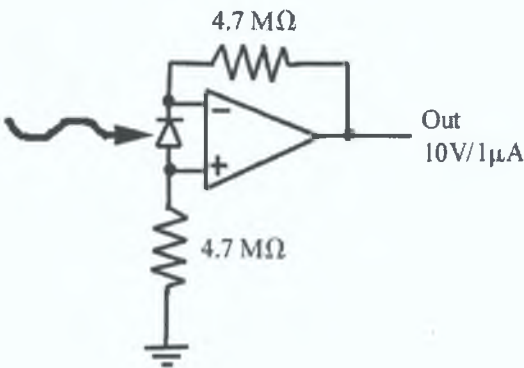


Figure B.1: Photodiode amplifier

B.4.2 ELED Driver Circuit

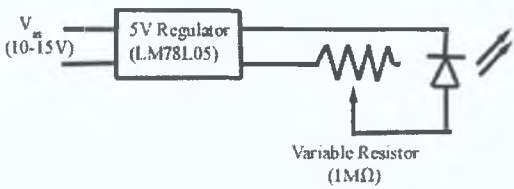


Figure B.2: Eled driver

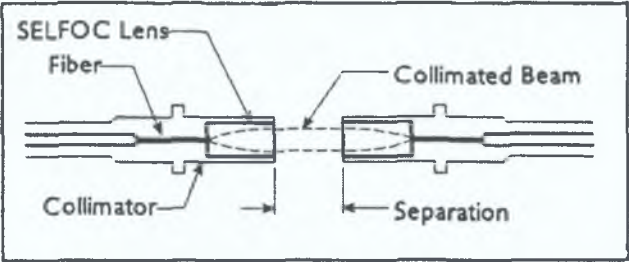
B.5 Grin Lens

SELFOC® Product Guide

SELFOC® Fiber Collimators

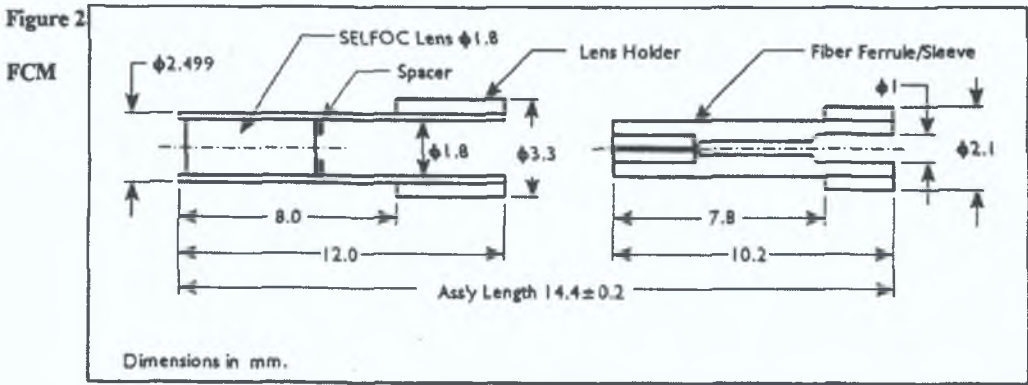
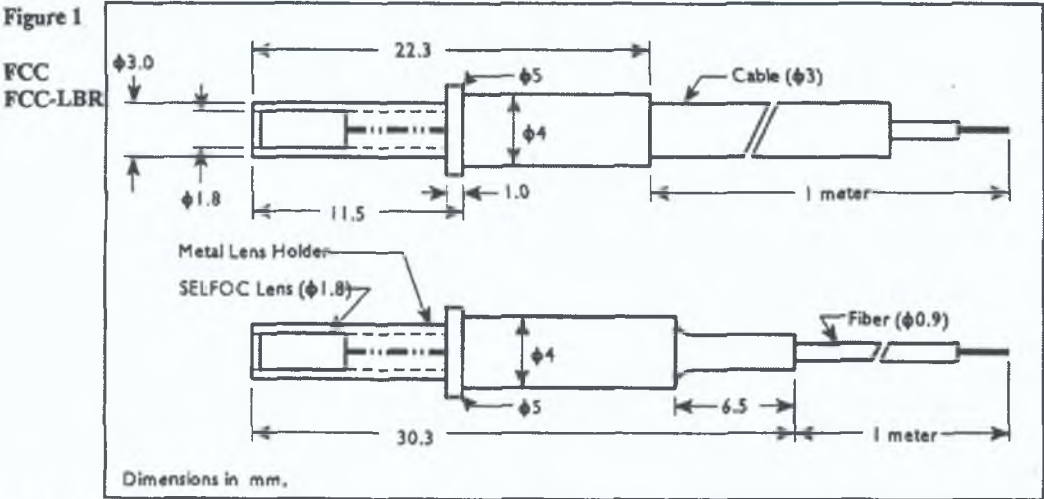
Applications:

- Expanded Beam Connectors
- Telecom Test Equipment
- Fiberoptic Sensors
- Signal Processing
- Light Source to Fiber Coupling



A SELFOC® Fiber Collimator is comprised of a 0.25 pitch SELFOC® lens and a housing to align with a fiber. Its functions are to produce a collimated beam from the fiber output, or to receive a collimated beam and focus the light into the fiber. The C-type (FCC) is the standard type assembled with one meter of fiber, singlemode (SMF) or multimode(MMF). The FCC-LBR is a special singlemode version with lower back reflection (-40dB or better) at both 1300 and 1550 nm. The M-type (FCM) comes unassembled and without fiber from NSG. The user inserts his own fiber into the ferrule (sleeve), a piece then fits into the lens holder to form an assembled unit.

Mechanical Diagram



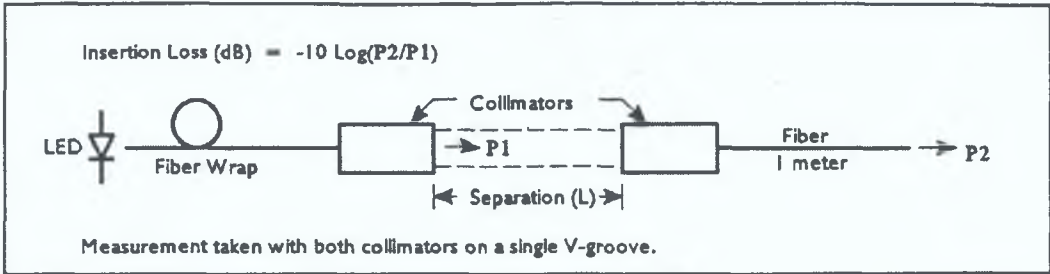


Figure 3 Insertion loss measurement setup for collimators

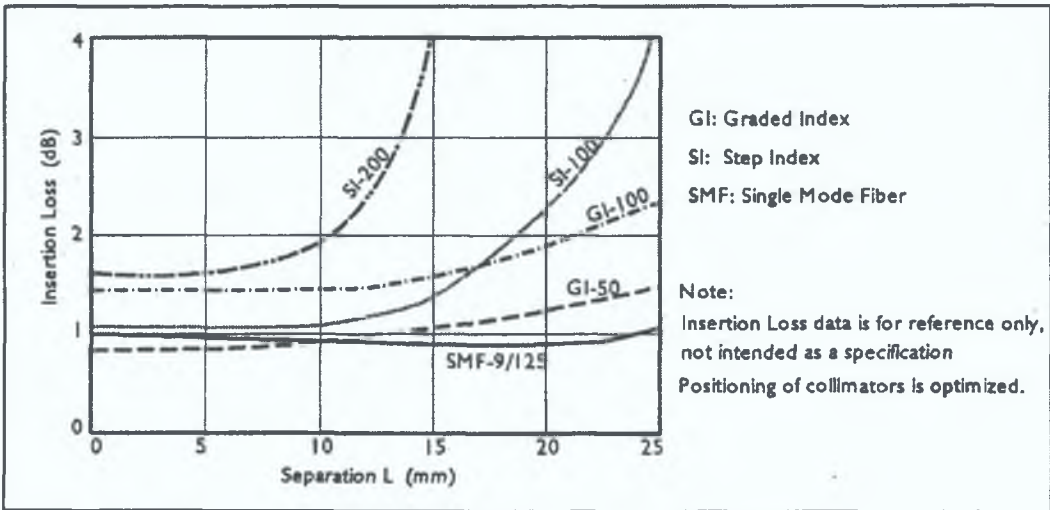


Figure 4 Typical insertion loss vs. separation distance

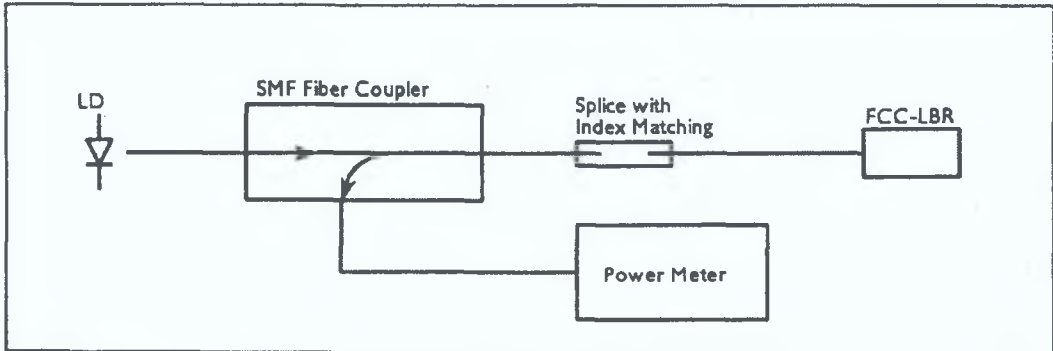


Figure 5 Back reflection measurement setup for fiber collimators

Table 1 Comparison of the 3 Types of Collimators

FEATURE / TYPE	FCC	FCC-LBR	FCM
Assembly	Assembled	Assembled	Unassembled
Fiber Type	MMF or SMF	SMF	MMF
Lens Holder O.D.	3.0 mm	3.0 mm	2.5 mm
Lens Holder Mat'l	Stainless Steel	Stainless Steel	Stainless Steel
Fiber Sleeve Mat'l	Stainless Steel	Stainless Steel	Stainless Steel
AR Coating on Lens	A-Grade (SMF) C-Grade (MMF)	W-Grade*	C-Grade

* See page 14 for reflection data.

Table 2 Optical Specifications for FCC

Type/Fiber	Insertion Loss**	Wavelength
SMF-LBR*	2.5 dB	1300 & 1550 nm
SMF	1.0 dB	1300 or 1550 nm
	1.5 dB	630 or 830 nm
All MMF	2.0 dB	All Wavelengths

* Back reflection specs for FCC-LBR is -40 dB or better at both 1300 and 1550 nm wavelengths
** 10 mm distance between two collimators.

Table 3 Standard Fiber Types, N.A., and Beam Divergence Angle

Fiber Code	Core / Cladding Size (µm)	Fiber N.A.	Beam Divergence Angle (2θ)
SMF	*125 core size varies with wavelength	---	0.3°
050	Graded Index 50/125	0.21	2.0°
062	Graded Index 62.5/125	0.29	2.5°
100GI	Graded Index 100/140	0.29	3.5°
100SI	Step Index 100/140	0.25	3.5°
200	Step Index 200/250	0.50	6.5°

Table 4 Reliability Specifications

TEMPERATURE RANGE	
Operation	0° ~ 60°C
Storage	-40° ~ 85°C
HUMIDITY	
85%RH - 60°C Max. Non-Condensing	

Table 5 Availability

Type	Fiber Type & Size	Standard Wavelength (nm)
FCC	SMF for specified wavelength MMF: 50/125, 62.5/125 100/140, 200/250	630, 830, 1300, 1550
FCC-LBR	SMF (9/125)	1300/1550
FCM	Cladding Size: 125, 140, 250µm	630, 830, 1300, 1550

Table 6 FCM ordering code/sleeve Size

Fiber Cladding Size	Fiber Sleeve I.D.	Ordering Code
125 µm	128 µm	FCM-00F-050-...
140 µm	144 µm	FCM-00F-100-...
250 µm	256 µm	FCM-00F-200-...

Ordering Information: X X X X X X X X X X X X X X X
Collimator Type: * ** Fiber Code Wavelength ***
FCC or FCM 050, 062, etc. 063, 130, etc. (Special Features)

- * Fiber Length (m): Standard 01 (1 meter). Extra cable length can be ordered at additional cost,
- ** Fiber Jacket:
 - F = Fiber (0.9 mm O.D. nylon jacket)
 - C = Cable (3 mm O.D. plastic/Kevlar/nylon jacket)
 - (For FCM, use 00F only, no fiber/cable supplied by NSG)
- *** Special Features:
 - LBR = Low Back Reflection (for FCC)
 - FC = FC connector on fiber end
 - FCPC = FCPC (Physical Contact) connector on fiber end
 - (Special features are subject to factory approval and may require additional process time)

RS Data Sheet

Hybrid stepper motors

Size	Rear shaft	No. of wires	RS stock no.
17	No	8	440-420
	Yes		440-430
	No		191-8399
	No		191-8306
23	No	8	440-442
	Yes	8	440-455
	No	6	191-8328
	No	6	191-8334
	No	6	191-8343
	No	6	191-8338
	No	8	101-8382
	No	8	181-8378
34	Yes	8	440-464
	No	8	440-470

These 4 phase hybrid stepper motors are capable of delivering much higher working torques and stepping rates than permanent magnet (7.5° and 15°) types. Whilst at the same time maintaining a high detent torque even when not energised. This feature is particularly important for positional integrity. Many of the motors are directly compatible with the RS stepper motor drive boards (RS stock nos. 332-066, 342-051 and 440-240).

Size 34 motors and a number of size 23 motors are supplied in 8-lead configuration which allows the maximum flexibility when connecting to the drive boards.

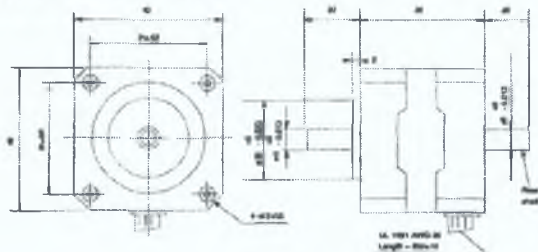
Rear extension shafts are provided on three of the motors to enable connection of other drive requirements and feedback devices.

1.8° step angle



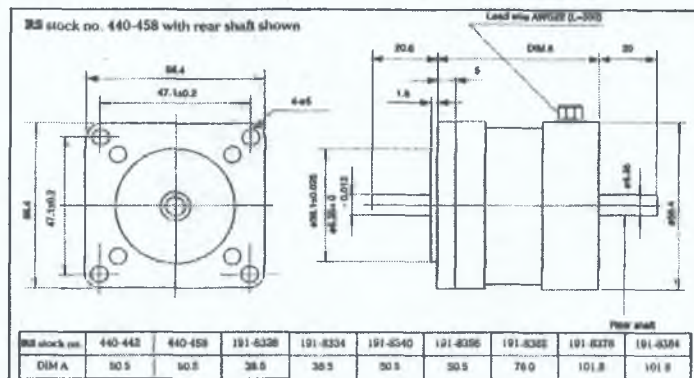
Size 17

RS stock no. 440-436 with rear shaft shown

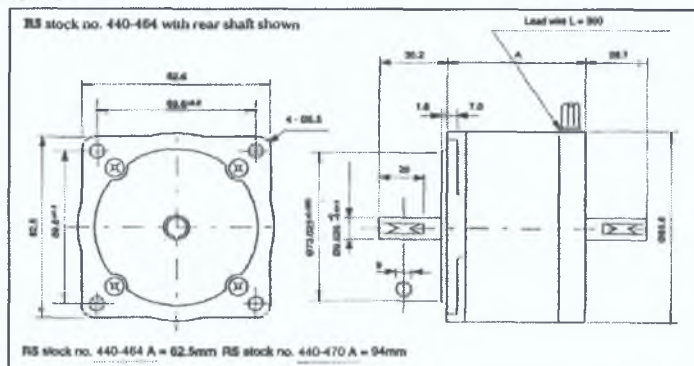


232-5749

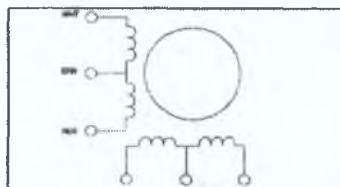
Size 23



Size 34

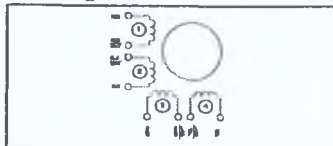


6 Wire configuration



Exciting sequence and direction of rotation when facing mounting flange end.						
Step	White	Blue	Red	Yellow	Brown	CW
1	On	On				+dir/V
2		On	On			
3			On	On		
4	On			On		

8 Wire configuration



Exciting sequence and direction of rotation when facing mounting flange end

Step	Red	Green	Black	Yellow	Com	CW
1	On	On				
2		On	On			
3			On	On		
4	On			On		

Technical specification

Stock no.	440-420	440-438	440-442	440-458	440-464	440-470
Rated voltage (V)	5	12	5	12	3	2.5
Rated current (I)	0.5	0.16	1	0.6	2	4.5
Resistance (Ω)	10	75	5	20	1.5	0.66
Inductance (mH)	6	36	9	32	4.5	2.8
Detent torque (mNm)	5	4	30	30	40	100
Holding torque (mNm)	70	70	500	600	1200	2200
Step angle accuracy (%)	5	5	5	5	5	5
Step angle	1.8	1.8	1.8	1.8	1.8	1.8
Insulation class	B	B	B	B	B	B

Stock no.	191-8290	191-8306	191-8328	191-8334	191-8340	191-8356	191-8362	191-8378	191-8384
Rated voltage (V)	12	15	5	12	12	12	5.4	3.4	6
Rated current (I)	0.4	0.4	1	0.4	0.48	0.6	1.4	2.85	1.8
Resistance (Ω)	30	45	5	40	25	20	3.8	1.2	3.5
Inductance (mH)	14	22	5.7	40	33	32	6.8	1.5	7.3
Detent torque (mNm)	3.5	3.5	14.8	14.8	29.6	29.6	56.5	77.6	77.6
Holding torque (mNm)	100	100	260	260	494	494	882	1200	1200
Step angle accuracy (%)	5	5	5	5	5	5	5	5	5
Step angle	1.8	1.8	1.8	1.8	1.8	1.8	1.8	1.8	1.8
Insulation class	B	B	B	B	B	B	B	B	B

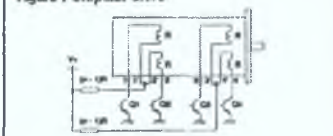
Resonance

Certain operating frequencies cause resonance and the motor loses track of the drive input. Audible vibration may accompany resonance conditions. These frequencies should be avoided if possible. Driving the motor on the half step mode (see motor drive methods) greatly reduces the effect of resonance. Alternatively extra load inertia and external damping may be added to shift resonance regions away from the operating frequency.

Motor drive methods

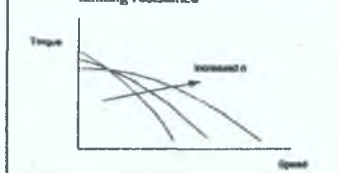
The normal way of driving a 4-phase stepper motor is shown in Figure 1.

Figure 1 Unipolar drive



This is commonly known as the 'Unipolar L/nr drive'. Here the current in each winding, when energised, flows in one direction only 'n', value is 21 (but not necessarily an integer) and nR is the sum of the external resistance plus the winding resistance (R). By selecting a higher value for n (i.e. larger external resistance) and using a higher dc supply to maintain the rated voltage and current for each winding, improved torque speed characteristics can be obtained. Thus a 6V, 60 motor (1A per phase) can be driven from a 6Vdc supply without any series resistor, in the L/R mode. Alternatively it can be driven from a 24Vdc supply using 180 series resistance in the L/4R mode with much improved performance.

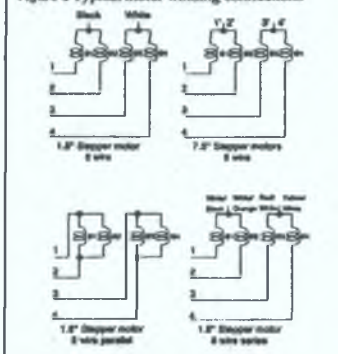
Figure 2 Effect on motor performance of higher supply voltages and larger series limiting resistance



Connection to RS bipolar stepper motor board

When the windings of the RS stepper motors are assigned (Q1-Q4) as shown in Figure 3, they can be connected to the board according to Figure 1.

Figure 3 Typical motor winding connections



When using 8 lead motors with coils in parallel the motor current should be set no greater than:

$$I \text{ per phase} \times \sqrt{2}$$

When using 6 lead or 8 lead motors with coils in series the motor current should be set no greater than:

$$I \text{ per phase} \times \frac{1}{\sqrt{2}}$$

Motors with 4 leads have a bipolar rating and can be used according to manufacturer's specification.

To step a motor in a particular direction a specific switching sequence for the drive transistors Q1-Q4 needs to be followed. If this sequence is in Table 1 (known as the unipolar full step mode) it results in the rotor advancing through one complete step at a time.

Table 1 Full step mode

Step No.	Q1	Q2	Q3	Q4
1	ON	OFF	OFF	ON
2	ON	OFF	ON	OFF
3	OFF	ON	OFF	ON
4	ON	OFF	OFF	ON
5	ON	OFF	ON	OFF

Start position (arbitrary) → Above sequence repeating

↑ Auto direction
↓ Clockwise

Table 2 Half step mode

Step No.	Q1	Q2	Q3	Q4
1	ON	OFF	ON	OFF
2	ON	OFF	OFF	ON
3	OFF	OFF	OFF	ON
4	OFF	ON	OFF	ON
5	OFF	ON	OFF	OFF
6	OFF	ON	ON	OFF
7	OFF	OFF	ON	OFF
8	ON	OFF	ON	OFF
9				

Start position → Above sequence repeating

↑ Auto direction
↓ Clockwise

Typical stepper motor control system

The operation of a stepper motor requires the presence of the following elements:



1. A control unit. Usually a microprocessor based unit which gives step and direction signals to the drive card. RS stepper motor control board (RS stock no. 440-098) is ideally suited for this function.
2. Power supply. Giving the required voltage and current for the drive card using a linear power supply.
3. Drive card. This converts the signals from the control unit in to the required stepper motor sequence. RS stock nos. 332-098, 342-081 and 440-240 are designed for the function.
4. Stepper motor.

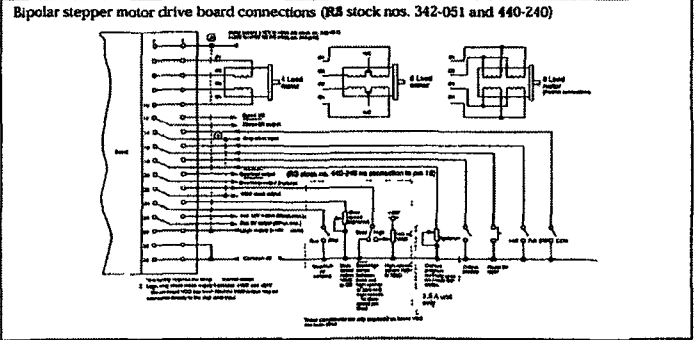
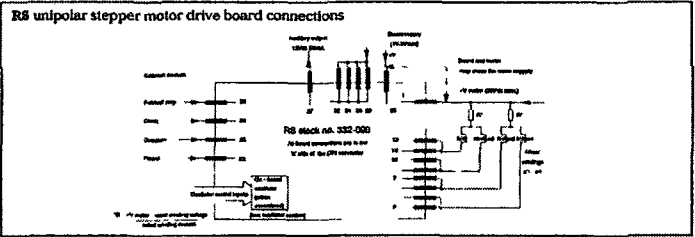
Stepper motor drive boards

For control of stepper motors RS has three types of stepper drive board which are suitable to drive stepper motors of various current ranges.

Drive board	RS stock nos	Suitable stepper motors	Suggested wiring configuration
Unipolar 2A (RS stock no. 332-098) This drive is only suitable for applications where low speeds and low torques are required	440-420 440-436 191-8299 191-8306 440-442 440-458 191-8328 191-8334 191-8340 191-8355 191-8362 191-8384	Size 17 Size 17 Size 17 Size 17 Size 23 Size 23 Size 23 Size 23 Size 23 Size 23 Size 23 Size 23	N/A
Bipolar 3 5A (RS stock no. 342-051) Suitable for medium current, medium torque applications	440-443 440-455 191-8328 191-8382 191-8378 191-8384 440-464 440-470	Size 23 Size 23 Size 23 Size 23 Size 23 Size 23 Size 34 Size 34	Series or parallel Parallel connection Series Series Series or parallel Series or parallel Series or parallel connection Series or parallel connection
Bipolar 6A (RS stock no. 440-240) Suitable for high current, high torque applications	191-8378 191-8384 440-464 440-470	Size 23 Size 23 Size 34 Size 34	Series or parallel Parallel Parallel connection Series or parallel connection

Note: Connecting a stepper motor in series will give a good low speed high torque performance.
Connecting a stepper motor in parallel will give a good high speed lower torque performance.

Drive board connections





Data Sheet

Multi-purpose gearbox (4Nm)

Ratio	RS stock no.	Ratio	RS stock no.
5:1	718-882	100:1	718-886
25:2	718-888	125:1	718-903
25:1	718-974	250:1	718-919
80:1	718-880	500:1	718-925

These gearboxes can be fitted to a range of RS motors with a particular adaptor kit.

Motors type	Motor RS stock no.	Adaptor kit	Adaptor kit RS stock no.	Mounting style
Hybrid stepper motor	440-420	A	718-931	2
	440-436	A	718-931	2
	440-442	C	718-953	1
	440-458	C	718-953	1
Tin can stepper motors	440-264	B	718-947	1A
	440-290	B	718-947	1A
	440-307	C	718-953	1A
	332-853	B	718-947	1A
Synchronous motors	440-391	B	718-947	1A
	440-408	B	718-947	1A
	440-414	C	718-953	1A

Adaptor	RS stock no.
A	718-931
B	718-947
C	718-953

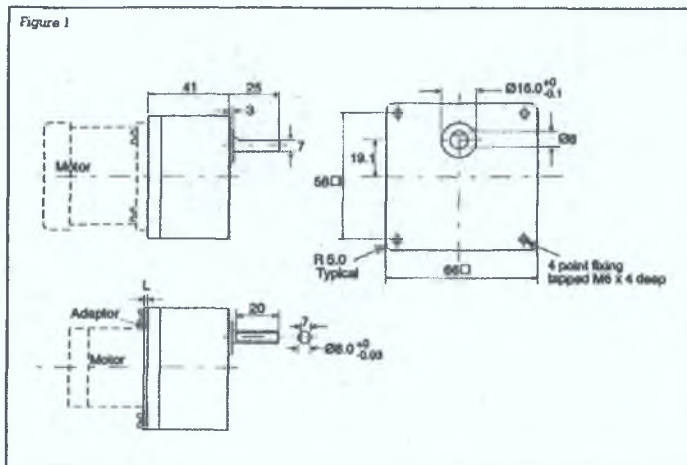
The multi-purpose design concept is based on being able to fit a wide variety of standard motors to the gear-head without special adapting or tooling. This approach has been achieved as a result of special attention to the mounting arrangement and careful consideration of the manner that fitting is carried out together with the adaptors necessary to maximise the number of motors that can be used.

The use of high strength metal spur gears throughout, coupled with a precision die-cast housing ensures that the multi-purpose gearbox provides a robust high torque, state of the art, design ideally suited to a wide range of applications including:

- CCTV camera pan and tilt mechanisms
- Medical drives for sampling tables and peristaltic pumps
- Industrial water and hydraulic valve actuation
- Small component conveyor drives
- Special effects drives
- Research and development motion control systems

Max. continuous output torque	4Nm
Max. continuous output power	15 Watts
Max. radial load on output shaft	25N
Max. axial load on output shaft	20N
Max. diameter of motor input shaft	8.35mm
Motor mounting	Via adaptor
Suitable motors	ac synchronous motors, stepper motors
Max. available gear ratio	800:1
Gear material	Metal throughout
Housing	Precision metal die-casting
Bearings	Sintered bronze
Dimensions	See following drawing

Figure 1



Gear ratio options

A wide choice of gear ratios is available as shown below.

In many cases 250rpm ac synchronous motors, 1.8 and 7.5 degree stepper motors may be used when the following speeds and steps/revolution will be obtained at the output of the gearhead.

Gear ratio	Output speed using 250rpm synchronous motor	Number of steps/rev using	
		7.5 degree stepper motors	1.8 degree stepper motors
8:1	50rpm	240	1000
25:2	20rpm	600	2500
25:1	10rpm	1200	5000
50:1	5rpm	2400	10,000
100:1	2.5rpm	4800	20,000
125:1	2rpm	6000	25,000
250:1	1rpm	12,000	50,000
500:1	0.5rpm	24,000	100,000

Using hybrid stepper motors

The number of steps/rev quoted above assumes the motor is used in full step. In most cases, it is recommended to drive the hybrid motor in half step drive when the above resolution will be doubled for each gear ratio.

Direction of rotation and efficiency

While the direction of rotation at the output is reversible its relationship to that of the input (motor) together with the efficiency, will depend on the number of gear stages within the multi-purpose gearhead as shown below.

Also, because the maximum output torque will be dependent, not only on the peak capability of 4Nm, but also on the maximum power transmission capability (15 Watts), in practice, the maximum recommended torque will be dependent on the gear ratio employed as shown below:

Gear ratio	No. of stages	Direction of rotation with respect to input	Efficiency	Max. output torque
5:1	3	Opposite	72%	1.5Nm
25:2	3	Opposite	72%	2.5Nm
25:1	4	Same	65%	4.0Nm
50:1	4	Same	65%	4.0Nm
100:1	5	Opposite	56%	4.0Nm
125:1	5	Opposite	56%	4.0Nm
250:1	6	Same	52%	4.0Nm
500:1	6	Same	52%	4.0Nm

Calculating output torque of geared motor combination:

Example 1

Motor torque: 0.25Nm at 600rpm (2000 steps/sec)

Gear ratio: 5:1 Efficiency: 72%

$$\text{Gearhead output torque} = 0.25 \times \frac{5 \times 72}{100} = 0.9\text{Nm at } 120\text{rpm}$$

Example 2

Motor torque: 0.07Nm at 260rpm

Gear ratio: 125:1 Efficiency: 58%

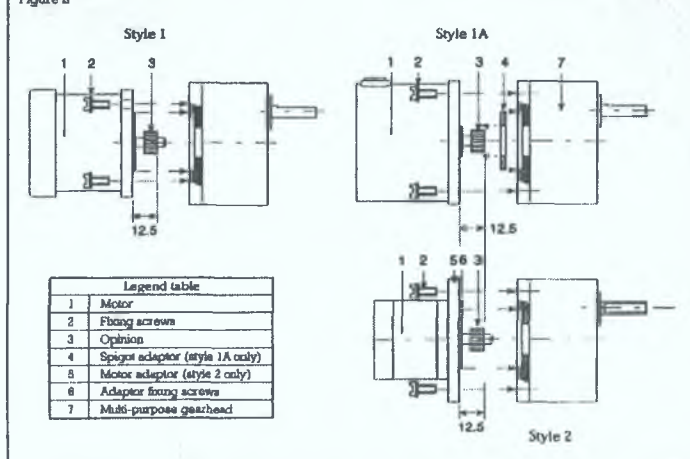
$$\text{Theoretical output torque} = 0.07 \times \frac{125 \times 58}{100} = 5.075\text{Nm}$$

Available output torque = 4.0Nm (see table on page 2).

Output torque using RS synchronous motors

Gear ratio	5:1	25:2	25:1	50:1	100:1	125:1	250:1	500:1
Output speed (rpm)	80	20	10	5	2.5	2	1	0.5
Typical torque (Nm) using motors:								
RS stock no.								
440-391	0.1	0.27	0.48	0.97	1.7	2.1	3.9	4.0
440-408	0.18	0.48	0.86	1.78	3.1	3.9	4.0	4.0
440-414	0.38	0.95	1.7	3.4	4.0	4.0	4.0	4.0

Figure 2



Motor fitting instructions

Motors are either fitted directly to the rear plate of the multi-purpose gearhead (Style 1 and 1A) or by means of a motor mounting adaptor (Style 2) as shown in the above drawings.

The appropriate motor pinions, adaptors and fixing screws are provided in three mounting kits which should be selected according to the motor to be used detailed opposite:

Assembly kit consisting:

	Screws	Pinion bore	Suitable motors RS stock no.
A	2 pieces M3 x 8mm	5mm	440-420
	4 pieces M4 x 8mm		440-436
B	4 pieces M4 washers	4mm	332-953
	2 pieces M4 x 8mm + washers	4mm	440-290
	2 pieces M3 x 4mm + washers	2mm	440-284
	2 pieces M3 x 4mm + washers	2mm	440-381
C	2 pieces M3 x 4mm + washers	2mm	440-408
	4 pieces M4 x 8mm + washers	6mm	440-307
	4 pieces M4 x 8mm + washers	6.35mm	440-414
	4 pieces M4 x 8mm + washers	6.35mm	332-052
		6.35mm	440-442
			440-458

General fitting instructions

The motor pinion is retained on the motor shaft using high strength retainer (RS stock no. 514-843). The application of the adhesive to the shaft should be done with care since it is important to ensure that a good bond is achieved.

Lightly rub the motor shaft with emery paper to provide a keyed surface, and ensure that the shaft and the pinion bore is clean and free of grease. Apply high strength adhesive to the shaft and slide the pinion into position, rotating it on the shaft to ensure a good spread of adhesive in the shaft/pinion joint. Always carry out this operation with the motor shaft horizontal and observe the adhesive manufacturer's instructions. Ensure that:

1. No adhesive comes in contact with the motor bearings.
2. All excessive adhesive is removed prior to fitting motor.

Fitting instructions using assembly kit A

Mounting style	Motors RS stock no.
2	440-420 440-436

Using the fitting components shown in the table carry out the following procedure:

1. Fit the motor adaptor (Item 5 on attached drawing) to the motor using the two M3 screws provided, one screw being fitted to each corner of the motor.
2. Fit the pinion to the shaft using the high strength adhesive as described, positioning the pinion so that it is 12.5mm ± 0.1 from the adaptor mounting face as shown in the attached drawing.
3. Fit the motor, adaptor assembly, directly to the back of the gearhead, taking care that the pinion slips freely back into mesh with the first gearwheel in the gearhead.

Note: The gearhead back plate is provided with two recesses in the casting to enable the heads of the motor retaining screws to be accommodated.

4. Secure using the four M4 screws as shown.

Fitting instructions using assembly kit B

Mounting style	Motors RS stock no.
1A	332-953 440-280 440-284 440-391

It should be noted that two adaptors are provided with the kit with bore sizes of either 9 or 12mm diameter to suit the alternative motor spigots provided. It is particularly important to ensure that, in the case of the motors which require the 9mm bore adaptor, that this is fitted as the first step in the motor fitting procedure.

2. Fit the pinion to the shaft using high strength adhesive as described, positioning the pinion so that it is 12.5mm ± 0.1 from the motor mounting face as shown in the drawing.
3. Fit the motor directly to the back of the gearhead, taking care that the pinion slips freely into mesh with the first gearwheel in the gearhead.
4. Secure using the four screws as shown in the table.

Fitting instructions using assembly kit C

Mounting style	Motors RS stock no.
1	440-442 440-458

Using the fitting components shown in the table carry out the following procedure:

1. Fit the pinion to the shaft using high strength adhesive as described, positioning the pinion so that it is 12.5mm ± 0.1 from the motor mounting face as shown in the drawing.
2. Fit the motor directly to the back of the gearhead, taking care that the pinion slips freely into mesh with the first gearwheel in the gearhead.
3. Secure using the four screws as shown in the table.

Mounting style	Motors RS stock no.
1A	440-307 440-414

Using the fitting components shown in the table carry out the following procedure:

1. Fit the circular motor spigot adaptor (Item 4 on attached drawing) to the motor.
2. Fit the pinion to the shaft using high strength adhesive as described, positioning the pinion so that it is 12.5mm ± 0.1 from the motor mounting face as shown in the drawing.
3. Fit the motor directly to the back of the gearhead, taking care that the pinion slips freely into mesh with the first gearwheel in the gearhead.
4. Secure using the four screws as shown in the table.

The information provided by RS Technical literature is intended to be accurate and reliable. However, RS Components assumes no responsibility for inaccuracies or omissions, as far as the use of this information, and all use of such information shall be entirely at the user's own risk. No responsibility is assumed by RS Components for any infringement of patents or other rights of third parties which may result from its use. Specifications shown in RS Components technical literature are subject to change without notice.

RS

Data Sheet

Strain gauges and load cells

Strain gauges

Two ranges of foil strain gauges to cover general engineering requirements for strain analysis. All gauges have 30mm integral leads to alleviate damage to the gauges due to excessive heat being applied during soldering and installation.

Miniature gauges can be used for precise point measurement of instrumentation of small components. The polyimide backing of the gauges can withstand temperatures up to 180°C making them ideal for higher temperature applications.

The larger size of the standard gauges will not only make these gauges suitable for larger components, but is useful to assess the average strain over the area covered by the gauge thus reducing the possibility of incorrect readings due to stress concentrations.

Gauges temperature compensated for aluminium match materials with a coefficient of thermal expansion of $23.4 \times 10^{-6}/^{\circ}\text{C}$ and are indicated by blue colour coding of the backing material.

Gauges temperature compensated for mild steel match materials with a coefficient of thermal expansion of $10.8 \times 10^{-6}/^{\circ}\text{C}$ and are indicated by red colour coding of the backing material.

All gauges are intended for uniaxial strain measurements only.

General specification (all types)

Measurable strain _____ 2 to 4% max.

Thermal output 20 to 160°C _____ ± 2 micro strain/ $^{\circ}\text{C}$ *

160°C to 180°C _____ ± 5 micro strain/ $^{\circ}\text{C}$ *

Gauge factor change _____ $\pm 0.015\%/^{\circ}\text{C}$ max.

Gauge resistance _____ 120 Ω

Gauge resistance tolerance _____ $\pm 0.5\%$

Fatigue life _____ $> 10^6$ reversals @ 100 micro strain*

Foil material _____ copper nickel alloy

* 1 micro strain is equivalent to an extension of 0.0001%

Specification

(Standard polyester backed types)

Temperature range _____ -30°C to +180°C

Gauge length _____ 8 mm

Gauge width _____ 2 mm

Gauge factor _____ 2.1

Base length (single types) _____ 13.0 mm

Base width (single types) _____ 4.0 mm

Base diameter (rosettes) _____ 21.0 mm

Specification

(Miniature polyimide backed type)

Temperature range _____ -30°C to +180°C

Gauge length _____ 2 mm

Gauge width _____ 1.8 mm

Gauge factor _____ 2.0

Base length (single types) _____ 6.0 mm

Base width (single types) _____ 2.5 mm

Base diameter (rosettes) _____ 7.5 x 7.5 mm

_____ 12 x 12 mm

Construction and principle of operation

The strain gauge measuring grid is manufactured from a copper nickel alloy which has a low and controllable temperature coefficient. The actual form of the grid is accurately produced by photo-etching techniques. Thermoplastic film is used to encapsulate the grid, which helps to protect the gauge from mechanical and environmental damage and also acts as a medium to transmit the strain from the test object to the gauge material.

The principle of operation of the device is based on the fact that the resistance of an electrical conductor changes with a ratio of $\Delta R/R$ as a stress is applied such that its length changes by a factor $\Delta L/L$. Where ΔR is change in resistance from unstressed value, and ΔL is change in length from original unstressed length.

The change in resistance is brought about mainly by the physical size of the conductor changing and an alteration of the conductivity of the material, due to changes in the materials structure.

Copper nickel alloy is commonly used in strain gauge construction because the resistance change of the foil is virtually proportional to the applied strain i.e.

$$\Delta R/R = K \epsilon$$

where K is a constant known as a gauge factor,

$$K = \frac{\Delta R/R}{\Delta L/L}$$

$$= \frac{\Delta R}{\Delta L}$$

$$\text{And } \epsilon = \text{strain} = \frac{\Delta L}{L} \therefore K = \frac{\Delta R/R}{\epsilon}$$

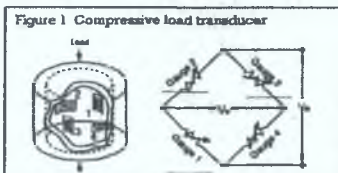
The change in resistance of the strain gauge can therefore be utilised to measure strain accurately when connected to an appropriate measuring and indicating circuit e.g. Strain gain amplifier RS stock no. 846-171 detailed later in this data sheet.

232-5957

Applications

When strain gauges are used in compressive load transducer applications, which normally require more stringent accuracy requirements, a full bridge circuit is used with active gauges in all four arms of the bridge, (Figure 1).

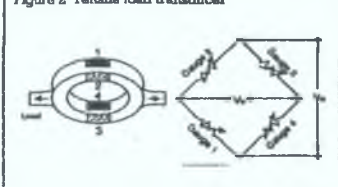
The load transducer shown in Figure 1 utilises four strain gauges attached to the cylinder. The gauges are connected into the bridge circuitry in such a manner as to make use of Poisson's ratio i.e. the ratio between the relative expansion in the direction of force applied and the relative contraction perpendicular to the force, to increase the effective gauge factor and thus the sensitivity.



To measure tensile loads, a ring with gauges attached as shown in Figure 2 may be used.

Under the action of a tensile load, the curvature of the ring in Figure 2 is deformed such that the inner gauges undergo tension while the outer gauges experience compressive forces.

Figure 2 Tensile load transducer



Instructions for mounting of strain gauges

In order to obtain the best possible results from a strain gauge, it is important to thoroughly prepare the gauge and the surface of the specimen to which the gauge is to be attached, prior to bonding with the adhesives recommended in paragraph 3 below.

1. Specimen surface preparation

An area larger than the installation should be cleared of all paint, rust etc., and finally smoothed with a fine grade emery paper or fine sand blasting to provide a sound bonding surface.

The area should now be degreased with a solvent such as RS PCB solvent cleaner, RS stock no. 496-883, and finally neutralised with a weak detergent solution. Tissues or lint free cloth should be used for this operation, wetting the surface and wiping off the clean tissues or cloth until the final tissue used is stain free. Care must be taken not to wipe grease from a surrounding area onto the prepared area or to touch the surface with the fingers.

This final cleaning should take place immediately prior to installation of the gauge.

2. Strain gauge preparation

By sticking a short length of adhesive tape along the upper face of the gauge it may be picked up from a flat clean surface. Holding both ends of the tape, orientate the gauge in the desired location and stick the end of the tape furthestmost from the tags to the specimen. Bend the other end of the tape back on itself thereby exposing the back of the gauge.

3. Adhesives and strain gauge installation

Two basic types of adhesive are recommended:

- RS cyanoacrylate
- RS 'quick-set' epoxy

When using epoxy adhesive coat the back of the gauge with adhesive and gently push down into position, wiping excess adhesive to the two outside edges of the gauge, to leave a thin film of adhesive between gauge and sample. Stick the whole length of tape to hold the gauge in position. Care should be taken that there is an even layer of adhesive and no air bubbles are left under the grid. Cover the gauge with cellophane or polyethylene etc., and apply a light weight or clamp as required until adhesive has set. Remove tape by slowly and very carefully pulling it back over itself, starting at the end furthestmost from the tags. Do not pull upwards.

If cyanoacrylate adhesive is to be used stick one end of the tape down to the specimen completely up to the gauge. Drop a fillet of adhesive in the 'hinge' point formed by the gauge and the specimen. Starting at the fixed end, with one finger push the gauge down at the same time pushing the adhesive along the gauge in a single wiping motion until the whole gauge is stuck down. Apply pressure with one finger over the whole length of the gauge for approximately one minute. Leave for a further three minutes before removing tape.

4. Wiring

The RS strain gauges are fitted with 30 mm leads to enable the gauge to be soldered. The lead out wires are fragile and should be handled with care.

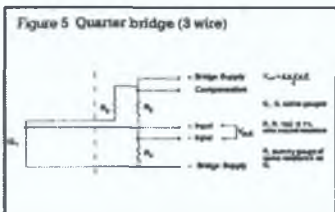
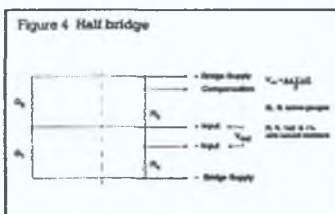
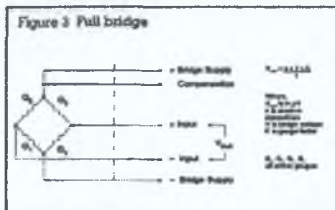
Installation protection

RS strain gauges are encapsulated and therefore are protected from dust and draughts etc. If however, additional protection from humidity, moisture, and mechanical damage is required RS silicone rubber compound, RS stock no. 555-588, may be used. This should be carefully spread over the installation using a spatula.

Connecting to strain gauges

The following bridge circuits are shown with connection referring to the basic amplifier circuit, Figure 7. All resistors, precision wire wound 0.1% 5 ppm. (For precision resistors see current RS Catalogue).

Note: The expressions are assuming that all gauges are subjected to the same strain. Some configurations produce different strain in different gauges, and allowance must be made.



Strain gauge amplifier (RS stock no. 848-171) and printed circuit board (RS stock no. 435-692)

Description and operation

The strain gauge amplifier is a purpose designed hybrid, low noise, low drift, linear dc amplifier in a 24 pin DIL package, specifically configured for resistive bridge measurement and in particular the strain gauges detailed earlier in this data sheet.

Foil strain gauges when attached to a specimen, produce very small changes in resistance (typically 0.2Ω in 120Ω per microstrain), and are thus normally connected in a Wheatstone bridge. Overall outputs of less than $1mV$ on a common mode voltage of 5 volts may be encountered, requiring exceptional common mode rejection which cannot be provided by conventional means.

The strain gauge amplifier overcomes the problem of common mode rejection by removing the common mode voltages. This is achieved by controlling the negative bridge supply voltage in such a manner that the voltage at the negative input terminal is always zero. Thus for a symmetrical bridge, a negative bridge supply is generated equal and opposite to the positive bridge supply, hence zero common mode voltage.

The advantages of such a system are:

- No floating power supply needed.
- Bridge supply easily varied with remote sense if necessary.
- Wire remote sense system.
- Freedom from common mode effects.
- Very high stability dc amplifier enables numerous configurations to be assembled.
- Low noise.
- High speed (at low gains).

Figure 5 Pin connections

Bridge Voltage	1	24	+ V_B
Bridge Supply Compensation	2	23	NC
NC	3	22	+ V_B
NC	4	21	NC
NC	5	20	Bridge Ref Input
+ Input	6	19	NC
NC	7	18	Feedback
NC	8	17	NC
NC	9	16	Output
- Input	10	15	NC
NC	11	14	NC
- Bridge Voltage	12	13	Zero Adjust

Top view

Specification(At 25°C ambient and $\pm 12V$ supply unless otherwise stated.)

Supply voltage	± 2 to $\pm 20V$ dc
Input offset voltage	200 μV max.
Input offset voltage/temperature	0.5 $\mu V/^\circ C$ max.
Input offset voltage/supply	3 $\mu V/V$ max.
Input offset voltage/time	0.3 $\mu V/month$ max.
Input impedance	> 5M Ω min.
Input noise voltage	0.9 $\mu V/p$ p max.
Band width (unity gain)	450kHz

Output current	5mA
Output voltage span	$\pm (V-2)V$
Closed loop gain (adjustable)	3 to 60,000
Open loop gain	> 120dB
Common mode rejection ratio	> 120dB
Bridge supply voltage/temperature	20 $\mu V/^\circ C$
Maximum bridge supply current	12mA
Power dissipation	0.5W
Warm up time	5 min
Operating temperature range	-25°C to +85°C

Figure 7 Basic circuit for printed circuit board 232 stock no. 435-692 (gain approx. 1000)

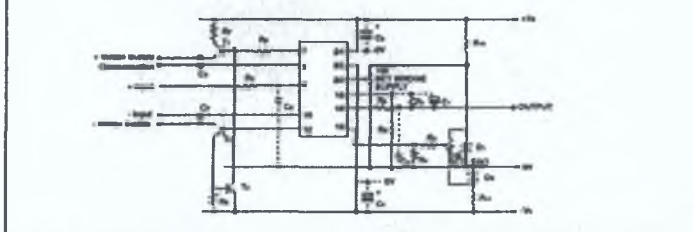
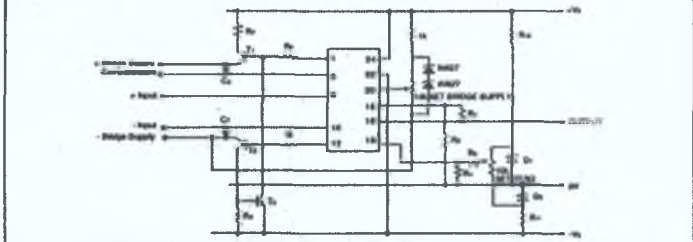


Figure 8 Circuit for semiconductor gauges and transducers

**Component values (Figures 7 and 8)**

R, 100k	R, 47R	C, C, 10n (typ.)
R, 100R	R, 10R	C, C, 10 μ (anal.)
R, 100k*	R, 1k Ω	T, BD 138
R, 68R*	R, 680R	T, BD 136
R, 10R	R, 680R	T, BC 108
R, 100R (typ.)	C, C, C, 100n (typ.)	D, D, 1N827

A glass fibre printed circuit board, RS stock no. 435-692 is available for the basic circuit as given in Figure 7.

The board is 46 x 98 mm in size and is complete with screen printed component identification and a solder mask.

Only typical values are given for certain components.

as adjustment of these values may be necessary in specific applications to obtain optimum noise reduction (see Minimisation of Noise later in data sheet).

*R₁ and R₂ values may be adjusted to alter the zero adjustment range when compensating for bridge imbalance.

Notes: 1. Gain is defined as $1 + \frac{R_1}{R_2}$

2. Zero adjustment range $\pm 6.2 \times \frac{R_1}{R_2 + R_1}$ Volts

Total bridge supply = $2 \times$ bridge ref input (pin 20)

C₁ may be omitted for input lead lengths of less than 10 metres

T_1 and T_2 provide bridge currents up to 60mA and should be kept away from amplifier.

T_3 and T_4 provide stability power supplies are being used zero and bridge supply reference may be taken direct from the power rails.

The high output of some semiconductor strain gauges may cause large amounts of asymmetry to the bridge. In correcting for the common mode change, the negative bridge voltage will change, causing a span error. This may be calibrated out or the arrangement above used to eliminate the cause of the error. Some semiconductor strain gauge transducers are temperature compensated by the use of series arm compensation. Thus the common mode voltage changes the with temperature, and hence the arrangement above should be used. This operates by referencing the positive bridge supply to the negative supply, thus varying the common mode but not the overall bridge supply.

Minimisation of noise

1. Inherent white/flicker noise in amplifier.

To keep this to a minimum use high quality (metal film) resistors and protect the amplifier from excessively high temperatures. The inherent noise level may be further reduced from its already low value by fitting C_1 and C_2 to reduce the operating bandwidth.

2. Supply frequency (or harmonics) interference.

If at 100Hz then the cause is almost likely to be from power supply rails, so use stabilised lines. If at 50Hz then it is generally caused by the location of the supply transformer, and/or the wiring. Relocate the supply transformer, screen and input leads to the amplifier, and if possible reduce the operating bandwidth by fitting C_1 and C_2 .

3. Power supply transient interference.

It is good practice to decouple the supply lines to the amplifier, by fitting C_3 and C_4 , as close to it as possible. If a particular nuisance then fit a mains suppressor.

4. Electromagnetic interference

This may be picked up by input leads, output leads, supply leads or direct into the circuit. Minimisation involves a combination of screening, decoupling and reducing operating bandwidth. Screening. The shield should be connected to only one earth potential at the receiving monitoring equipment end. Try not to earth any of the dc power lines (e.g. 0V). If the shield at the sensor end is earthed then earth the shield at the receiving end and if possible connect this earth potential to the strain gauge amplifier circuit shield. Decouple the power supply leads by fitting C_3 and C_4 , decouple the input leads with R_6 and C_5 (note a similar action on the input is not possible). Remove any pickup from the output leads by fitting R_8 and C_7 . Fit C_6 if input leads are more than 10m long and fit C_8 if remote sense is longer than 10m. Reduce the operating bandwidth by fitting C_1 and C_2 .

Appendix C C Code listings

C.1 Program 1: Control rotation stage and sample data from photodiode amplifier

```
// Scan      - Bragg grating Interigation

// Header    - Program to scan wavelength 1330 - 1270
//

// Version   - 3.0

// Author    - mck@physics.dcu.ie

// Date      - 23/06/98

#include <stdio.h>
#include <stdlib.h>
#include <conio.h>
#include <math.h>
#include <graphics.h>

/* Addresses */

#define BASE      640
#define start     BASE + 16
#define eoc       BASE + 20
#define LS_data   BASE + 19
#define MS_data   BASE + 18
#define const     1.253314137

int tot_loop=1000;
int i,j,ja,k,msamp,loop,no_scan;
int data[97],temp,midpoint;
float chitemp;
float tempt,tempb,value;
float chi[4167];
float far scant[8283];
float far scandata[8333];
float far lamda[8333],angle;
char buffer[80];
double a,w;
float lhalf,lc1,lc2;
int lc1i,lc2i,lm;
float hw1,hw2;

// File Handles
FILE *data_out;
FILE *data_out1;
FILE *data_outf;
FILE *mid;
FILE *chia;

void main()
{
```

```

/* request auto detection */
int gdriver = DETECT, gmode, errorcode;

/* initialize graphics mode */
initgraph(&gdriver, &gmode, "");

/* read result of initialization */
errorcode = graphresult();

if (errorcode != grOk) /* an error occurred */
{
printf("Graphics error: %s\n", grapherrormsg(errorcode));
printf("Press any key to halt:");
getch();
exit(1); /* return with error code */
}

// setup screen
// Viewport1
setviewport(20,20,120,210,1);
lineto(100,0);
lineto(100,190);
lineto(0,190);
lineto(0,0);

// Viewport2
setviewport(130,20,620,210,1);
lineto(490,0);
lineto(490,190);
lineto(0,190);
lineto(0,0);

// Viewport3
setviewport(20,220,295,460,1);
lineto(275,0);
lineto(275,240);
lineto(0,240);
lineto(0,0);

// Viewport4
setviewport(305,220,620,460,1);
lineto(315,0);
lineto(315,240);
lineto(0,240);
lineto(0,0);

//Initialise acd/io board

outportb(647,128);

// Find out how many scans to do
setviewport(21,21,119,209,1);
clearviewport();
moveto(2,4);
outtext("# Scans?");
//scanf("%d",&no_scan);
no_scan=1;

```

```

for(loop=0;loop<no_scan;loop++)
{

buffer[0]=NULL;

for(i=0;i<8333;i++)
{
    for(temp=0;temp<3000;temp++);
    outportb(644,1);

    for(msamp=0;msamp<47;msamp++)
    {

        outportb(start,7);
        while((inportb(eoc) && 1) != 1);
        for(temp=0;temp<2000;temp++);
        temp=(inportb(LS_data)/16);
        data[msamp]=(inportb(MS_data)*16)+temp;

    }

    // calculate average

    tempt=0.0;

    for(msamp=0;msamp<47;msamp++)
    {
        tempt=tempt+(float) data[msamp];
    }

    value=tempt/47;

    scandata[i]=value;
    outportb(644,3);
}

// Reverse spin direction

for(i=0;i<8333;i++)
{
    outportb(644,0);
    for(j=0;j<30000;j++);
    outportb(644,2);
    for(j=0;j<30000;j++);
}

// rearrange data
// Find Basepoint
tempt=0.0;
for(i=0;i<8333;i++)
{
    tempt=tempt+scandata[i];
}
tempt=tempt/8333;

```

```

for(i=0;i<8333;i++)
{
    scandata[i]=scandata[i]-0.3*tempt;
}

// Find Midpoint
for(i=2083;i<6251;i++)
{
    k=0;
    j=0;
    ja=0;
    chitemp=0;
    while(j>-1 && ja<8333)
    {
        chitemp=chitemp+((scandata[i+k]-scandata[i-
k]))*(scandata[i+k]-scandata[i-k]));
        k++;
        j=i-k;
        ja=i+k;
    }

    if(j<ja) chi[i-2083]=chitemp/k;
    if(ja<j) chi[i-2083]=chitemp/k;

}

chia=fopen("c:\\scan\\data\\chi.dat","w");
chitemp=999999;
for(i=1;i<4167;i++)
{
    fprintf(chia,"%d %f \n",i,chi[i]);
    if(chitemp>chi[i])
    {
        midpoint=i+2083;
        chitemp=chi[i];
    }
}
fclose(chia);

mid=fopen("c:\\scan\\data\\mids.dat","a");
fprintf(mid,"%d \n",midpoint);
fclose(mid);

// Plot scandata
msamp=21;
setviewport(131,21,619,209,1);
clearviewport();
for(i=0;i<8333;i=i+17)
{
    putpixel(500-msamp,(180-(scandata[i]/24)),14);
    msamp++;
}

//convert index to angles
for(i=0;i<8333;i++)
{
    angle=(float)(i-midpoint)*6.2834e-5;
    angle=sin(angle);
    lamda[i]=1307.45576*sqrt(1.0-(0.52146587*angle*angle));
}

```

```

}

setviewport(21,21,119,209,1);
clearviewport();
moveto(2,4);
outtext("Fitting ");

// Averageing routine
printf("1");
for(i=25;i<8308;i++)
{
    tempt=0.0;
    for(j=-25;j<25;j++)
    {
        tempt=tempt+scandata[i+j]/10.0;
    }
    tempt=tempt/5;
    scant[i-25]=tempt;
}

for(i=25;i<8308;i++)
{
    scandata[i]=scant[i-25];
}

printf("2");

data_outf=fopen("c:\\scan\\data\\fullstel.dat","a");
for(i=0;i<8333;i++)
{
    fprintf(data_outf,"%f %f \n",lamda[i],scandata[i]);
}
fclose(data_outf);

//Remove instrument function
tempt=0;
tempb=65000;
for(i=8332;i>=midpoint;i--)
{
    a=((1.45118e-28)*exp(0.0579*lamda[i]))/(114516);
    scandata[i]=scandata[i]/a;
    if(scandata[i]>tempt)
    {
        tempt=scandata[i];
        temp=i;
    }
    if(scandata[i]<tempb)
    {
        tempb=scandata[i];
    }
}

lhalf=(tempt-tempb)/2.0+scandata[8300];

// Find Centers
i=midpoint;
lcl=0;
lc2=0;
while(scandata[i]<0.6*tempt)

```

```

{
    i++;
}
while(scandata[i]>0.55*tempt)
{
    if(scandata[i]>lc1)
    {
        lc1=scandata[i];
        lc1i=i;
    }
    i++;
}

i=8332;
while(scandata[i]<0.5*tempt)
{
    i--;
}
while(scandata[i]>0.50*tempt)
{
    if(scandata[i]>lc2)
    {
        lc2=scandata[i];
        lc2i=i;
    }
    i--;
}

tempb=65000;
for(i=lc1i;i<lc2i;i++)
{
    if(scandata[i]<tempb)
    {
        tempb=scandata[i];
        lm=i;
    }
}

//Calculate HalfWidths

i=lc1i;
lhalf=scandata[lc1i]/2.0;
while(scandata[i]>lhalf)
{
    i--;
}

hw1=((lamda[i]-lamda[lc1i])*2.0)-2.75;

i=lc2i;
lhalf=scandata[lc2i]/2.0;
while(scandata[i]>lhalf)
{
    i++;
}

hw2=((lamda[lc2i]-lamda[i])*2.0)-2.75;

// Find Turning points

```



```

data_outf=fopen("c:\\scan\\data\\fullstep.dat","w");
for(i=0;i<8333;i++)
{
    fprintf(data_outf,"%f %f \n",lamda[i],scandata[i]);
}
fclose(data_outf);

data_out1=fopen("c:\\scan\\data\\datasm.dat","a");
fprintf(data_out1,"%f %f %f
%f\n",lamda[lc1i],hw1,lamda[lc2i],hw2);
fclose(data_out1);

}
}

```

C.2 Program 2: Convert multi-scan datafile into single scan data files

```

#include <stdio.h>
#include <stdlib.h>
#include <conio.h>
#include <math.h>
#include <string.h>

int i,j;
float value,lamda;
char filename[80],dummy[20];

FILE *input;
FILE *output;

void main(void)
{
    input=fopen("fullstel.dat","r");
    //output=fopen("3d.dat","w");
    for(i=0;i<30;i++)
    {
        filename[0]=NULL;
        dummy[0]=NULL;
        itoa(i,dummy,10);
        strcpy(filename,dummy);
        strcat(filename,".dat");
        output=fopen(filename,"w");

        for(j=0;j<8333;j++)
        {
            fscanf(input,"%f %f\n",&lamda,&value);
            /*if(fmod(j,25)==0)
            { */

```

```

        fprintf(output,"%f %f\n",lamda,value);
    /*
        */
    }

    fclose(output);
}

/*fclose(output);*/
fclose(input);
}

```

C.3 Program 3: Genetic Algorithm for deconvolution of spectra

```

/*****
/* Title : Program to find centers and FWHM for scanned */
/* data.
*/
/* Author : Michael Kennedy Version : 1.1
*/
/* Date : 12/12/1998
*/
*****/

#include <stdio.h>
#include <dos.h>
#include <stdlib.h>
#include <math.h>
#include <conio.h>
#include <string.h>

/* Addresses */

#define BASE 640
#define start BASE + 16
#define eoc BASE + 20
#define LS_data BASE + 19
#define MS_data BASE + 18

/*****
/* Function : Declare global variables
*/
*****/

int i, oloop;
double lamda1, lamda2, dlamda1, dlamda2;
double amp1, amp2;
double cost[100];
double cutdata[2][3500];
double population[6][21];

void preprocess(void);
double sosplv(double fx, double br, double sos, double lor1, double
lor2, double gauss, double amp, double pos, int n);
double callsolsos(int posit, int yes_no);
void gen_pop(void);
double D_Evolution(void);

```

```

void preprocess(void)

{
/*****
/* Function : Declare variables for estimation routine */
*****/
int i,midpoint;
int k,j,ja;
float scandata[8000],temp,chi[3500];
double chitemp,angle,diffdata[3500];
double center[20],lamdamax;
float smooth;
char buffer[80];

FILE *input;
FILE *output;
FILE *chif;

/*****
/* Function : Open input/output files
*/
*****/

buffer[0]=NULL;
itoa(oloop,buffer,10);
strcat(buffer,".dat");

input=fopen(buffer,"r");
output=fopen("out.dat","w");

/*****
/* Function : Read data from file into array scandata */
*****/

    for(i=0;i<8000;i++)
    {
        fscanf(input,"%f %f",&temp,&scandata[i]);
    }
    fclose(input);

    for(i=0;i<8000;i++)
    {
        fprintf(output,"%d %f\n",i,scandata[i]);
    }
    fclose(output);

/*****
/* Function : Find middle of data structure, full array */
/*           is a mirror image of itself */
/*           Place chi^2 in an array so it may be
*/
/*           written to a file later
*/
*****/

    for(i=2000;i<6000;i++)
    {
        k=0;

```



```

    }

/*****
/* Function : Remove filter transmittance function from */
/*                               data                               */
/*                               */
/* Note : Function was generated from data on filter */
/*****
/*
    for(i=0;i<3500;i++)
    {
        chitemp=((1.45118e-28)*exp(0.0579*cutdata[0][i]))/(114516);
        cutdata[1][i]=cutdata[1][i]/chitemp;
    }
*/
/*****
/* Function : We attempt to find the transmission peaks */
/*
                               */
/* This involves differentiation of the data and */
/* detection of the zero crossing points. Care has to be */
/* taken to account for the possibility of noisy crossing */
/* points.
                               */
/*****
/*****
/* Function : Differentiate Data
                               */
/*****

    for(i=0;i<3999;i++)
    {
        diffdata[i]=
                                (cutdata[1][i]-
cutdata[1][i+1])/(cutdata[0][i]-cutdata[0][i+1]);
    }

/*****
/* Function : Smooth diff. data using nearest neighbour */
/*                               averaging                               */
/*                               */
/*****

    for(i=5;i<3995;i++)
    {
        smooth=0.0;
        for(j=-4;j<5;j++)
        {
            smooth+=diffdata[i+j];
        }
        diffdata[i]=smooth/9.0;
    }

/*****
/* Function : Output diff. data to file "diff.dat" */
/*****

    output=fopen("diff.dat","w");
    for(i=0;i<3500;i++)
    {

```

```

        fprintf(output, "%lf %lf\n", cutdata[0][i], diffdata[i]);
    }
    fclose(output);

/*****
/* Function : Find zero crossing points and store in      */
/*                               array                      */
/*                               */
*****/

j=0;
for(i=0; i<3990; i++)
{
    if(cutdata[0][i]<1305.0 && cutdata[0][i]>1295.0)
    {
        if(((diffdata[i]<0.0) && (diffdata[i+1]>0.0))
            || ((diffdata[i]>0.0) && (diffdata[i+1]<0.0)))
        {
            center[j]=(cutdata[0][i]+cutdata[0][i+1])/2.0;
            j++;
        }
    }
}

/*****
/* Function : From crossing points found above find      */
/*                               central lamdas.          */
/*                               */
/* Note : Remember three crossing points will be found   */
/*                               2 lamdas and the turning  */
/*                               between them.             */
*****/

j=0;
temp=0;
while(temp<0.1)
{
    temp=center[j]-center[j+1];
    if(temp<0.1)
    {
        center[j+1]=(center[j]+center[j+1])/2;
    }
    j++;
}
lamda1=center[j-1];
temp=0;

while(temp<0.1)
{
    temp=center[j]-center[j+1];
    j++;
}
temp=0;

while(temp<0.1)
{
    temp=center[j]-center[j+1];
    if(temp<0.1)
    {
        center[j+1]=(center[j]+center[j+1])/2;
    }
}

```

```

        j++;
    }
    lamda2=center[j-1];

    /**/
/* Find Amplitudes */

    for(i=0;i<3500;i++)
    {
        if(pow((cutdata[0][i]-lamda1),2)<0.01) amp1=cutdata[1][i];
        if(pow((cutdata[0][i]-lamda2),2)<0.01) amp2=cutdata[1][i];
    }

/*****
/* Function : Find Combined FWHM
        */
/*
        Using similar system to centers
        */
/* Note : This is done using the normal data not the */
/* diff. data
        */
/*****/

    for(i=0;i<20;i++)
    {
        center[i]=0.0;
    }

    i=0;

    while(cutdata[0][i]>lamda1)
    {
        lamdamax=cutdata[1][i]/2.0;
        i++;
    }
    j=0;

    while(i>0)
    {
        if(((cutdata[1][i]<lamdamax) && (cutdata[1][i+1]>lamdamax))
            || ((cutdata[1][i]>lamdamax) &&
(cutdata[1][i+1]<lamdamax)))
        {
            center[j]=(cutdata[0][i]+cutdata[0][i+1])/2.0;
            j++;
        }
        i--;
    }

    i=3500;
    while(cutdata[0][i]<lamda2)
    {
        lamdamax=cutdata[1][i]/2.0;
        i--;
    }

    while(i<3500)
    {
        if(((cutdata[1][i]<lamdamax) && (cutdata[1][i+1]>lamdamax))

```

```

        || ((cutdata[1][i]>lamdamax) &&
(cutdata[1][i+1]<lamdamax)))
    {
        center[j]=(cutdata[0][i]+cutdata[0][i+1])/2.0;
        j++;
    }
    i++;
}

dlamda1=center[0]-lamda1;
dlamda2=lamda2-center[1];

/*****
/* Function : Write scan data to file "cutdata.dat" */
*****/

output=fopen("cutdata.dat","w");
for(i=0;i<3500;i++)
{
    fprintf(output,"%lf %lf\n",cutdata[0][i],cutdata[1][i]);
}
fclose(output);
}

double callsolsos(int posit,int yes_no)
{
    double fx,br,sos,gauss,amp,pos;
    double lor1,lor2;
    double cutdata_new[3500];
    double chi_sq,cutdata_min;
    FILE *test_outa;

    br=(population[0][posit]/population[1][posit]);
    sos=population[2][posit]-population[3][posit];
    amp=population[0][posit];
    pos=population[2][posit];
    lor1=population[4][posit];
    lor2=population[5][posit];

    cutdata_min=1e64;
    for(i=3499;i>=0;i--)
    {
        fx=cutdata[0][i];
        //gauss=((fx*-0.04242)+58.42694);
        gauss=3.0;
        cutdata_new[i]=sosplv(fx,br,sos,lor1,lor2,gauss,amp,pos,i);
        if(cutdata_new[i]<cutdata_min) cutdata_min=cutdata_new[i];
    }

    if(yes_no==1)
    {
        test_outa=fopen("vdata.dat","w");
        for(i=0;i<3500;i++)
        {
            //cutdata_new[i]=cutdata_new[i]-cutdata_min;
            fprintf(test_outa,"%lf
%lf\n",cutdata[0][i],cutdata_new[i]);
        }
        fclose(test_outa);
    }
}

```



```

/*****
/* Procedure : Calculate chi squared
*/
*****/

chi_sq=0.0;
for(i=0;i<3500;i++)
{
    chi_sq+=pow((cutdata[1][i]-cutdata_new[i]),2)/cutdata[1][i];
}
chi_sq=chi_sq;
return(chi_sq);
}

double sosplv(double fx,double br,double sos, double lor1,double
lor2, double gauss, double amp,double pos,int n)
{
    int j;
    static double sqrt2=2.051;
    static double con=2.6939e-6;
    static double A[4]={-1.2150,-1.3509,-1.2150,-1.3509};
    static double B[4]={1.2359,0.3786,-1.2359,-0.3786};
    static double C[4]={-0.3085,0.5906,-0.3085,0.5906};
    static double D[4]={0.0210,-1.1858,-0.0210,1.1858};
    double al[4],be[4];
    double y,V,X,Y,constant;

    y=0;
    V=0;
    X=((2617)-(2*pos)-(con*n*n))/(lor1*sqrt2);
    Y=sqrt2/lor1;
    constant=amp;

    for(j=0;j<=3;j++)
    {
        al[j]=C[j]*(Y-A[j])+D[j]*(X-B[j]);
        be[j]=(Y-A[j])*(Y-A[j])+(X-B[j])*(X-B[j]);
        V+=al[j]/be[j];
    }

    y+=constant*V;
    X=((2617)-(2*pos-sos)-(con*n*n))/(lor2*sqrt2);
    Y=sqrt2/lor2;
    constant=amp/br;
    V=0.0;

    for(j=0;j<=3;j++)
    {
        al[j]=C[j]*(Y-A[j])+D[j]*(X-B[j]);
        be[j]=(Y-A[j])*(Y-A[j])+(X-B[j])*(X-B[j]);
        V+=al[j]/be[j];
    }

    y+=constant*V;
    return(y);
}

void gen_pop(void)
{

```

```

        int i;
        /*FILE *pop_in;

        pop_in=fopen("popdata.dat","r");
        for(i=0;i<20;i++)
        {
            fscanf(pop_in,"%lf %lf %lf %lf %lf
%lf\n",&population[0][i],&population[1][i],&population[2][i],&populat
ion[3][i],&population[4][i],&population[5][i]);
        }
        fclose(pop_in);
        */
        for(i=0;i<20;i++)
        {
            population[0][i]=amp1+(float)(rand()%1000)-
500;/// $((float)(rand()\%50000)/10.0)+16000$ ;/// $amp1+(((float)(rand()\%100)/100.0)-0.5)*amp1/2$ ;
            population[1][i]=amp2+(float)(rand()%1000)-
500;/// $((float)(rand()\%50000)/10.0)+16000$ ;/// $amp2+(((float)(rand()\%100)/100.0)-0.5)*amp2/2$ ;
            population[2][i]=lamda1+(((float)(rand()%1000)/1000.0)-0.05);
            population[3][i]=lamda2+(((float)(rand()%1000)/1000.0)-0.05);
            population[4][i]=0.3+(float)(rand()%2000)/10000;
            population[5][i]=0.3+(float)(rand()%2000)/10000;
        }
    }

double D_Evolution(void)
{

    int i,k,vec_1,vec_2,vec_3;
    double sec_pop[6][20];
    double cost_vec_pri,cost_vec_tri;
    double min_cost;

    /******
    /* Function : Differential Evolution algorithm
    /* Loop through all 100 members of the population
    /******

    for(i=0;i<20;i++)
    {

        min_cost=1e63;

        /******
        /* Choose three random Vectors from the primary pop.
        /* All three must be different but may include the
        /* selected vector for comparison later if I choose
        /******

        do(vec_1=rand()%20; while(vec_1==i);
        do(vec_2=rand()%20; while(vec_2==vec_1 || vec_2==i);
        do(vec_3=rand()%20; while(vec_3==vec_1 || vec_3==vec_2 ||
vec_3==i);

```

```

/*****
/* Function : Generate trail vector, 0.5 is the F value */
/*****
    for(k=0;k<6;k++)
    {

        population[k][20]=population[k][vec_1]+0.9*(population[k][vec_2
]-population[k][vec_3]);
    }

/*****
/* Function : Check which vector is better
*/
/*****

    cost_vec_pri=callsolsos(i,0);
    cost_vec_tri=callsolsos(20,0);

    if(min_cost>cost_vec_pri) min_cost=cost_vec_pri;

    if((cost_vec_pri>cost_vec_tri) && (population[4][20] < 1) &&
(population[4][20] > 0.3) && (population[5][20] < 1) &&
(population[5][20] > 0.3) && (population[0][20]/population[1][20] < 3
&& population[0][20]/population[1][20] > 0.33))
    {
        //printf("%d %lf %lf Swaping\n",i,cost_vec_pri,cost_vec_tri);
        for(k=0;k<6;k++)
        {
            sec_pop[k][i]=population[k][20];
        }
    }
    else
    {
        //printf("%d %lf %lf Not
Swaping\n",i,cost_vec_pri,cost_vec_tri);
        for(k=0;k<6;k++)
        {
            sec_pop[k][i]=population[k][i];
        }
    }
}
/*****
/* Function : Swap secondary and primary
*/
/*****

for(i=0;i<20;i++)
{
    for(k=0;k<6;k++)
    {
        population[k][i]=sec_pop[k][i];
    }
}

return(min_cost);
}

void main(void)
{
    double lam_min,dummy;
    int j,i,i_min;

```

```

FILE *pop_out;
FILE *result;

for(oloop=0;oloop<1;oloop++)
{
    preprocess();

    /* Generate first population */
    gen_pop();

    /* Start Genetic algor. */

    for(i=0;i<200;i++)
    {
        dummy=D_Evolution();
        //printf(".");
        printf("%d %lf %lf %lf %lf
%lf\n",i,dummy,population[0][20],population[1][20],population[4][20],
population[5][20]);
    }
    printf("\n");

    /* Find Minimum chi squared */
    lam_min=1e64;
    for(i=0;i<20;i++)
    {
        dummy=callsolsos(i,0);
        if(lam_min>dummy)
        {
            lam_min=dummy;
            i_min=i;
        }
    }
    dummy=callsolsos(i_min,1);

    pop_out=fopen("popdata.dat","w");
    //dummy=dummy/3500;
    //fprintf(pop_out,"Population data min %d at chi_sqr
%lf\n",i_min,dummy);
    for(j=0;j<20;j++)
    {
        for(i=0;i<6;i++)
        {
            fprintf(pop_out,"%lf ",population[i][j]);
        }
        fprintf(pop_out,"\n");
    }
    fclose(pop_out);
    printf("Loop %d chi sqrd=%lf @ %d\n",oloop,dummy,i_min);
    result=fopen("result.dat","a");
    fprintf(result,"%lf ",dummy);
    for(i=0;i<6;i++)
    {
        fprintf(result,"%lf ",population[i][i_min]);
    }
    fprintf(result,"\n");
    fclose(result);
}

```

```

    getch();
}

```

C.4 Program 4: Routines to test viability of deconvolution system

Voigt function test code

```

#include <stdio.h>
#include <stdlib.h>
#include <conio.h>
#include <math.h>

float pri_pop[16][21], sec_pop[16][20];
float input_dat[101][100];

FILE *input;

void read_data(void)
{
    int i,j;
    float t1,t2;

    input=fopen("mkvo.dat", "r");
    for(i=0;i<101;i++)
    {
        for(j=0;j<100;j++)
        {
            fscanf(input, "%f %f %f\n", &t1, &t2, &input_dat[i][j]);
        }
    }
}

void gen_pop(void)
{
    int i,j;

    for(i=0;i<20;i++)
    {
        for(j=0;j<16;j=j+4)
        {
            pri_pop[j][i]=((float) (rand()%30000)/10000.0)-1.5;
        }
        for(j=1;j<16;j=j+4)
        {
            pri_pop[j][i]=((float) (rand()%30000)/10000.0)-1.5;
        }
        pri_pop[2][i]=pri_pop[0][i];
        pri_pop[3][i]=pri_pop[1][i];
        pri_pop[6][i]=-1*pri_pop[4][i];
        pri_pop[7][i]=-1*pri_pop[5][i];
        pri_pop[10][i]=pri_pop[8][i];
        pri_pop[11][i]=pri_pop[9][i];
        pri_pop[14][i]=-1*pri_pop[12][i];
        pri_pop[15][i]=-1*pri_pop[13][i];
    }
    pri_pop[0][0]=-1.2150;
    pri_pop[1][0]=-1.3509;
}

```

```

pri_pop[2][0]=-1.2150;
pri_pop[3][0]=-1.3509;
pri_pop[4][0]=1.2359;
pri_pop[5][0]=0.3786;
pri_pop[6][0]=-1.2359;
pri_pop[7][0]=-0.3786;
pri_pop[8][0]=-0.3085;
pri_pop[9][0]=0.5906;
pri_pop[10][0]=-0.3085;
pri_pop[11][0]=0.5906;
pri_pop[12][0]=0.0210;
pri_pop[13][0]=-1.1858;
pri_pop[14][0]=-0.0210;
pri_pop[15][0]=1.1858;

```

```

}

```

```

float sosplv(float x,float y,int posit)
{
    int i;
    float v,top,bottom;

    v=0.0;

    for(i=0;i<4;i++)
    {
        top=(pri_pop[8+i][posit]*(y-
pri_pop[0+i][posit]))+(pri_pop[12+i][posit]*(x-pri_pop[4+i][posit]));
        bottom=pow((y-pri_pop[0+i][posit]),2)+pow((x-
pri_pop[4+i][posit]),2);
        v+=top/bottom;
    }
    return(v);
}

```

```

float callsolsos(int posit,int yes_no)
{
    int i,j;
    float cutdata_new[101][100];
    float x,y;
    float chi_sq;
    FILE *output;

    for(i=0;i<101;i++)
    {
        for(j=0;j<100;j++)
        {
            x=-4.0+(0.08*(float)i);
            y=0.104+(0.004*(float)j);
            cutdata_new[i][j]=sosplv(x,y,posit);
        }
    }

    chi_sq=0.0;
    for(i=0;i<101;i++)
    {
        for(j=0;j<100;j++)
        {

```

```

        chi_sq+=pow((input_dat[i][j]-
cutdata_new[i][j]),2)/input_dat[i][j];
    }
}
if(yes_no==1)
{
    output=fopen("fitted.dat", "w");
    for(j=0;j<16;j++)
    {
        fprintf(output,"%f ",pri_pop[j][posit]);

    }
    printf("\n");
    for(i=0;i<101;i++)
    {
        for(j=0;j<100;j++)
        {
            x=-4.0+(0.08*(float)i);
            y=0.104+(0.004*(float)j);
            fprintf(output,"%f %f %f\n",x,y,cutdata_new[i][j]);
        }
    }
}

return(chi_sq);
}

double D_Evolution(void)
{

int i,k,vec_1,vec_2,vec_3;
float cost_vec_pri,cost_vec_tri;
float min_cost;

/*****
/* Function : Differential Evolution algorithm
/* Loop through all 100 members of the population
*****/

for(i=0;i<20;i++)
{

min_cost=1e63;

/*****
/* Choose three random Vectors from the primary pop.
/* All three must be different but may include the
/* selected vector for comparison later if I choose
*****/

        do(vec_1=rand()%20); while(vec_1==i);
        do(vec_2=rand()%20); while(vec_2==vec_1 || vec_2==i);
        do(vec_3=rand()%20); while(vec_3==vec_1 || vec_3==vec_2 ||
vec_3==i);

/*****
/* Function : Generate trail vector, 0.5 is the F value
*****/

```

```

        for(k=0;k<16;k++)
        {
            pri_pop[k][20]=pri_pop[k][vec_1]+0.5*(pri_pop[k][vec_2]-
pri_pop[k][vec_3]);
        }

/*****
/* Function : Check which vector is better
*/
*****/

        cost_vec_pri=callsolsos(i,0);
        cost_vec_tri=callsolsos(20,0);

        if(min_cost>cost_vec_pri) min_cost=cost_vec_pri;
        if(min_cost>cost_vec_tri) min_cost=cost_vec_tri;

        if(cost_vec_pri>cost_vec_tri)
        {
            for(k=0;k<16;k++)
            {
                sec_pop[k][i]=pri_pop[k][20];
            }
        }
        else
        {
            for(k=0;k<16;k++)
            {
                sec_pop[k][i]=pri_pop[k][i];
            }
        }
    }
/*****
/* Function : Swap secondary and primary
*/
*****/

    for(i=0;i<20;i++)
    {
        for(k=0;k<16;k++)
        {
            pri_pop[k][i]=sec_pop[k][i];
        }
    }

    return(min_cost);
}

void main()
{
    int i,i_min,j;
    float dummy,lam_min;
    FILE *chi;

    gen_pop();
    read_data();
    chi=fopen("chis.dat","w");

    for(i=0;i<10000;i++)

```



```

{
    dummy=D_Evolution();
    fprintf(chi,"%d %f ",i,dummy);

    lam_min=1e64;
    for(j=0;j<20;j++)
    {
        dummy=callsolsos(j,0);
        if(lam_min>dummy)
        {
            lam_min=dummy;
            i_min=j;
        }
    }
    for(j=0;j<16;j++)
    {
        fprintf(chi,"%f ",pri_pop[j][i_min]);

    }
    fprintf(chi,"\n");
}
/* Find Minimum chi squared */
lam_min=1e64;
for(i=0;i<20;i++)
{
    dummy=callsolsos(i,0);
    if(lam_min>dummy)
    {
        lam_min=dummy;
        i_min=i;
    }
}
dummy=callsolsos(i_min,1);
}

```

Genetic algorithm test code

```

// Genetic Algorithm
// Directed Evolution

// Version 0.1
// Date - 31/09/98
// Author - mck@physics.dcu.ie

#include <stdio.h>
#include <stdlib.h>
#include <conio.h>
#include <math.h>

#define no_pop    25
#define no_var    10
#define no_step   100
#define const 1.253314137
#define tot_loop 1500

// Global Variables
int i,j,k,count;
int a,b,c,tempint;
int loop,cr_count;
double start_value[no_var];

```

```

double trail_value[no_var];
double bestfit[no_var];
double cost_a[no_pop];
double population[no_pop][no_var];
double secd[no_pop][no_var];
double far_start_shape[no_step][2];
double far_trail_shape[no_step];
double cr=0.6, f=0.5, temp_lamda;
double tempt, score, costmin, costold;
double ran_temp, best;
double lamda_min, lamda_max, delta;

FILE *data_out;
FILE *cost_out;
FILE *loop1;

double lineshape(double);
double cost(void);
void check(void);
void input(void);

// Lineshape generator
double lineshape(double linepoint)
{
    double y;
    double t[12];

    t[0]=((linepoint-trail_value[3])*(linepoint-trail_value[3]));
    t[1]=(trail_value[2]*trail_value[2]);
    if(t[1]==0) printf("t1");
    t[2]=-2*(t[0]/t[1]);
    t[3]=exp(t[2]);
    t[4]=((linepoint-trail_value[6])*(linepoint-trail_value[6]));
    t[5]=(trail_value[5]*trail_value[5]);
    if(t[5]==0) printf("t5");
    t[6]=-2*(t[4]/t[5]);
    t[7]=exp(t[6]);
    t[8]=((linepoint-trail_value[9])*(linepoint-trail_value[9]));
    t[9]=(trail_value[8]*trail_value[8]);
    if(t[9]==0) printf("t9");
    t[10]=-2*(t[8]/t[9]);
    t[11]=exp(t[10]);

    y=trail_value[0]+(((trail_value[1]/(trail_value[2]*const))*t[3]
)+
                ((trail_value[4]/(trail_value[5]*const))*t[7])+
                ((trail_value[7]/(trail_value[8]*const))*t[11]));

    return y;
}

// Costing function
double cost(void)
{
    int loop;
    double temp_cost, tot_cost;

    tot_cost=0.0;
    for(loop=0; loop<no_step; loop++)
    {

```

```

        temp_cost=((start_shape[loop][1]-trail_shape[loop])*
                    (start_shape[loop][1]-trail_shape[loop]));
        tot_cost=tot_cost+temp_cost;
    }

    tot_cost=tot_cost;
    return(tot_cost);
}

void check(void)
{

    ran_temp=(double)(rand()%1000);
    if(trail_value[1]<1 || trail_value[1]>3000) trail_value[1]=
    4000.0*(ran_temp/1000)+0.00001;

    ran_temp=(double)(rand()%1000);
    if(trail_value[2]<0.1 || trail_value[2]>3) trail_value[2]=
    3*(ran_temp/1000)+0.00001;

    ran_temp=(double)(rand()%1000);
    if(trail_value[3]<(lamda_min) || trail_value[3]>(lamda_max))
trail_value[3]=
    1270+60*(ran_temp/1000);

    ran_temp=(double)(rand()%1000);
    if(trail_value[4]<1 || trail_value[4]>3000) trail_value[4]=
    4000.0*(ran_temp/1000)+0.00001;

    ran_temp=(double)(rand()%1000);
    if(trail_value[5]<0.1 || trail_value[5]>3) trail_value[5]=
    3*(ran_temp/1000)+0.00001;

    ran_temp=(double)(rand()%1000);
    if(trail_value[6]<(lamda_min) || trail_value[6]>(lamda_max))
trail_value[6]=
    1270+60*(ran_temp/1000);

    ran_temp=(double)(rand()%1000);
    if(trail_value[7]<1 || trail_value[7]>3000) trail_value[7]=
    4000.0*(ran_temp/1000)+0.00001;

    ran_temp=(double)(rand()%1000);
    if(trail_value[8]<0.1 || trail_value[8]>3) trail_value[8]=
    3*(ran_temp/1000)+0.00001;

    ran_temp=(double)(rand()%1000);
    if(trail_value[9]<(lamda_min) || trail_value[9]>(lamda_max))
trail_value[9]=
    1270+60*(ran_temp/1000);
}

void input(void)
{

    double input[2000][2];
    double temp;

    int i,j;

    FILE *data_in;

```

```

data_in=fopen("100a.dat","r");

i=0;
while(!feof(data_in))
{
    fscanf(data_in,"%lf %lf",&input[i][0],&input[i][1]);
    i++;
}
lamda_max=input[0][0];
lamda_min=input[i-2][0];
delta=(lamda_max-lamda_min)/no_step;

j=0;
for(i=0;i<no_step;i++)
{
    temp=lamda_max-(i*delta);
    while(input[j][0]>temp) j++;
    start_shape[i][0]=input[j][0];
    start_shape[i][1]=input[j][1];
}

}

void main()
{
    clrscr();
    input();
    data_out=fopen("temp.dat","w");
    /*
    // Get start values
    printf("Input start value for baseline,area,width,lamda ? \n");
    scanf("%lf %lf %lf %lf %lf %lf %lf %lf %lf %lf",
    &start_value[0],
    &start_value[1],&start_value[2],&start_value[3],&start_value[4],
    ,
    &start_value[5],&start_value[6],&start_value[7],&start_value[8],
    ,
    &start_value[9]);

    //generate start shape
    for(i=0;i<no_var;i++)
    {
        trail_value[i]=start_value[i];
    }
    */
    for(i=0;i<no_step;i++)
    {
        /*
        start_shape[i][0]=((((start_value[3]+start_value[6]+
        start_value[9])/3)-3.5)+((double)i*7e-2));
        temp_lamda=start_shape[i][0];
        start_shape[i][1]=lineshape(temp_lamda)+(20-
        (double)(rand()%40));
        */
        fprintf(data_out,"%lf %lf\n",start_shape[i][0],start_shape[i][1]);
    }

    fclose(data_out);
}

```

```

// Generate random vectors in search space

for(i=0;i<no_pop;i++)
{
    ran_temp=(double) (rand()%1000);
    population[i][0]=300+300*(ran_temp/1000);
    ran_temp=(double) (rand()%1000);
    population[i][1]=1000+2000.0*(ran_temp/1000);
    ran_temp=(double) (rand()%1000);
    population[i][2]=1+2*(ran_temp/1000);
    ran_temp=(double) (rand()%1000);
    population[i][3]=1270+60*(ran_temp/1000);
    ran_temp=(double) (rand()%1000);
    population[i][4]=1000+2000.0*(ran_temp/1000);
    ran_temp=(double) (rand()%1000);
    population[i][5]=1+2*(ran_temp/1000);
    ran_temp=(double) (rand()%1000);
    population[i][6]=1270+60*(ran_temp/1000);
    ran_temp=(double) (rand()%1000);
    population[i][7]=1000+2000.0*(ran_temp/1000);
    ran_temp=(double) (rand()%1000);
    population[i][8]=1+2*(ran_temp/1000);
    ran_temp=(double) (rand()%1000);
    population[i][9]=1270+60*(ran_temp/1000);
}

//Calculate Cost array
for(i=0;i<no_pop;i++)
{
    for(k=0;k<no_step;k++)
    {
        temp_lamda=start_shape[k][0];
        for(j=0;j<no_var;j++)
        {
            trail_value[j]=population[i][j];
        }
        trail_shape[k]=lineshape(temp_lamda);
    }
    cost_a[i]=cost();
}
cost_out=fopen("cost.dat","w");
count=0;
costmin=1e12;
while(count<tot_loop)
{
    for(i=0;i<no_pop;i++)
    {
        //Pick three vectors from the search Space
        a=(rand()%no_pop);
        b=(rand()%no_pop);
        c=(rand()%no_pop);

        j=(rand()%no_var);

        // f=(rand()%10);
        // f=f/10;

        for(k=0;k<no_var;k++)

```

```

        {
            tempt=((double) (rand()%100)/100);
            if(tempt < cr || k==10)
            {
                trail_value[j]=population[c][j]+(f*(population[a][j]-
population[b][j]));
            }
            else
            {
                trail_value[j]=population[i][j];
            }
            j=(j+1);
            if(j==10) j=0;
        }
        //Calculate cost of trail vector
        check();

        for(k=0;k<no_step;k++)
        {
            temp_lamda=start_shape[k][0];
            trail_shape[k]=lineshape(temp_lamda);
        }
        score=cost();

        if(score<=cost_a[i])
        {
            for(k=0;k<no_var;k++)
            {
                secd[i][k]=trail_value[k];
                cost_a[i]=score;
            }
        }
        else
        {
            for(k=0;k<no_var;k++)
            {
                secd[i][k]=population[i][k];
            }
        }
    }

    for(i=0;i<no_pop;i++)
    {
        for(k=0;k<no_var;k++)
        {
            population[i][k]=secd[i][k];
        }
    }

    //if(count==100) f=0.7;
    //if(count==500) f=0.8;
    //if(count==750) f=0.9;

    count++;

    //find costmin

```

```

costold=costmin;

for(i=0;i<no_pop;i++)
{
    if(costmin>cost_a[i])
    {
        costmin=cost_a[i];
        tempint=i;
        for(k=0;k<no_var;k++)
        {
            bestfit[k]=population[i][k];
        }
    }
}
best=costmin/90;
printf("%d %lf %d %lf \n",cr_count,f,count,best);
if(best<250)
{

if(costold-costmin<10)
{
    cr_count++;
}
else
{
    cr_count=0;
}

if(cr_count>10)
{
    ran_temp=rand()%100;
    f=ran_temp/100;
    cr_count=0;
}
}

fprintf(cost_out,"%d %lf \n",count,best);
}

fclose(cost_out);
data_out=fopen("templ.dat","w");
for(i=0;i<no_var;i++)
{
    trail_value[i]=bestfit[i];
}

for(i=0;i<no_step;i++)
{
    start_shape[i][0]=((((bestfit[3]+bestfit[6]+
bestfit[9])/3)-3.5)+((double)i*7e-2));
    temp_lamda=start_shape[i][0];
    start_shape[i][1]=lineshape(temp_lamda);
    fprintf(data_out,"%lf %lf
\n",start_shape[i][0],start_shape[i][1]);
}

fclose(data_out);
for(k=0;k<no_var;k++)
{
    printf("%lf ",bestfit[k]);
}

```

}

Deconvolution test code (deconvolute *perfect* data)

```
#include <stdio.h>
#include <stdlib.h>
#include <conio.h>
#include <math.h>

int i,j;
float far data[8333];
double function[1300];

double far dataac[7033];
double intsum,tempff;
float tempf;
float far datad[8333];

FILE *org;
FILE *conv;
FILE *deconv;
FILE *input;
FILE *filter;

void main()
{

clrscr();

/*****
/*  GENERATE INPUT FUNCTION          */
/*  8333 Steps total                */
*****/
/*
for(i=0;i<8333;i++)
{
    if((i>3000 && i<3100) || (i>3300 && i<3400))
    {
        data[i]=1;
    }
    else
    {
        data[i]=0;
    }
}

/*****
/*  Integrate accross input          */
/*  7933 Steps total                */
*****/
/*
for(i=0;i<8033;i++)
{
/*****
/*  GENERATE Filter FUNCTION          */
/*  300 Steps total                */
*****/
/*
```

```

for(j=0;j<150;j++)
{
    function[j]=j;
}
for(j=299;j>149;j--)
{
    function[j]=(299-j);
}

intsum=0.0;
for(j=0;j<300;j++)
{
    intsum+=((float)data[i+j]*(float)function[j]);
}
datac[i]=intsum;
}

*/
// Read in data file

input=fopen("fdata.rel","r");

for(i=0;i<650;i++)
{
    fscanf(input,"%f %f ",&tempf,&tempf);
}

for(i=0;i<7033;i++)
{
    fscanf(input,"%f %lf ",&tempf,&tempff);
    if(tempff<215)
    {
        datac[i]=tempff;
    }
    else
    {
        datac[i]=tempff;
    }
    printf("%lf \n",datac[i]);
}
fclose(input);

// Read in Filter Function

filter=fopen("lorentz.dat","r");
for(i=0;i<1300;i++)
{
    fscanf(filter,"%f %lf",&tempf,&function[i]);

    function[i]=function[i]/100;
    printf("%lf \n",function[i]);
}
fclose(filter);

/*****
/* Deconvolute Data to Input          */
/* 7933 Steps total                    */
*****/

```

```

//Make assumption about start of data

for(i=0;i<8333;i++)
{
    datad[i]=0.042;
}

//Start deconvolution

for(i=0;i<7033;i++)
{
    /******
    /*  GENERATE Filter FUNCTION          */
    /*  300 Steps total                   */
    /******

    //Integrate to second last step

    intsum=0.0;
    for(j=0;j<1299;j++)
    {
        intsum+=datad[i+j]*(float)function[j];
    }

    intsum=intsum;
    datad[i+1298]=(datac[i]-intsum);
    //printf("%d %f \n",i,datad[i+400]);
}

//Output Data

org=fopen("org.dat","w");
conv=fopen("conv.dat","w");
deconv=fopen("deconv.dat","w");

for(i=0;i<7033;i++)
{
    fprintf(conv,"%d %f \n",i+650,datac[i]);
}

for(i=650;i<7683;i++)
{
    fprintf(deconv,"%d %f \n",i,datad[i]);
    fprintf(org,"%d %f \n",i,data[i]);
}

fclose(org);
fclose(conv);
fclose(deconv);

//getch();

}

```

C.5 Program 5: Simulation of Bragg grating with apodisation

Author: Dr. Vincent Ruddy

```
C          VRAPOD3.FOR
C      Lineshape with apodisation

      IMPLICIT DOUBLE PRECISION (A-H,K,O-Z)
      COMPLEX PQ,RS,SM1,TERM1,TERM2,TERMT,TERMB,GAMMA,CT,CSIG,A,B
      COMPLEX AA,BB,F,TI,TR,SHAA,SNBB,TETA
      DIMENSION ALF(10000),ANSP(3000),X(3000)
      SM1=(0.0,1.0)
      PIE=3.14159
C      Define the Bragg wavelength and grating length in metres
      XLAMB=1300.0E-9
      XL=2.5E-3
C      Define the index modulation value (maximum value at grating
centre)
      DELN=2.000E-4
C      Define the Gaussian apodisation function ALF(I)
      DO 2 I=1,1
      ALF(I)=1.0E+5
C      Set up the imaginary part of the phase to account for apodisation
C      sigi is the imaginary part of the detuning parameter sigma to
C      take into account Gaussian apodisation
C      of the form
C           $\exp(-ALF(Z+L/2)**2)$ 
C      The function y which is
C
      Kappa*TANH(A+iB)
C
      -----
C
      GAMMA-i(SIGMA)*TANH(A+iB)
C
      and its complex conjugate are multiplied together

      SIGI=ALF(I)*XL/2.0
      YMAX=0.0
      DO 1 N=1,300
      XLAM=1297.8+(4.0)*N/300.0
      XLAM=XLAM*(1E-9)
      XKAP=PIE*DELN/XLAM
C      Set up SIGR the real part of the detuning parameter sigma
      S1=(2.0*PIE/XLAM)*DELN
      S2=(2.0*PIE*1.45)*((1.0/XLAM)-(1.0/XLAMB))
      SIGR=S1+S2
C      Define the COMPLEX number SIGMA (SIGR,SIGI)
      CSIG=SIGR+SM1*SIGI
      TOP=-2*SIGR*SIGI
      BOT=(XKAP**2)-(SIGR**2)+(SIGI**2)
      IF (BOT.EQ.0.0) THEN
```

```

      TETA=PIE/2.0

      ELSE
        TETA=DATAN2 (TOP,BOT)
      ENDIF
      TP=TETA/2.0
      G=DSQRT (BOT**2+TOP**2)
      F=DSQRT (G)
      A=XL*F*DCOS (TP)
      B=XL*F*DSIN (TP)
      AA=2.0*A
      BB=2.0*B
      IF (AIMAG (AA) .EQ. 0.0)   THEN
        CHAA=DCOSH (AA)
        SHAA=DSINH (AA)
      ELSE
        AAP=AIMAG (AA)
        CHAA=DCOS (AAP)
        SHAA=SM1*DSIN (AAP)
      ENDIF
      IF (AIMAG (BB) .EQ. 0.0)   THEN
        CSBB=DCOS (BB)
        SNBB=DSIN (BB)
      ELSE
        BBP=AIMAG (BB)
        CSBB=DCOSH (BBP)
        SNBB=-SM1*DSINH (BBP)
      ENDIF
      GAMMA= (A/XL) +SM1* (B/XL)
      TR= (SHAA) / (CHAA+CSBB)
      TI=SNBB/ (CHAA+CSBB)
      CT=TR+SM1*TI
      PQ=XKAP*CT
      TERMT=CONJG (PQ)
      RS=GAMMA-SM1* (CSIG) * (CT)
      TERMB=CONJG (RS)
      TERM1=PQ*TERMT
      TERM2=RS*TERMB
      ANSP (N) =TERM1/TERM2
      YMAX=AMAX1 (ANSP (N) , YMAX)
      X (N) =XLAM
      X (N) =XLAM* (1.0E9)
      WRITE (*, 3) X (N) , ANSP (N)
1      CONTINUE
      IF (YMAX.LT.0.95) THEN
        GO TO 2
      ELSE
        CONTINUE
      ENDIF
      DO 30 K=1,300
      IF (ANSP (K) .EQ. YMAX) THEN
        XLAMO=X (K)
      ELSE
        CONTINUE
      ENDIF
30      CONTINUE
C      Normalise the spectrum to 1.0 on the peak
      DO 5 M=1,300
      YY=ANSP (M) /YMAX
      W=ABS (X (M) -XLAMO)
      HLM=0.3568

```

```

      IF(YY GT 0 3560 AND YY LT 0 3575) THEN
        W=W*(1 0E9)
C      WRITE (*,3) DELN,ALF(I),YMAX,W
      ELSE
      CONTINUE
      ENDIF
5     CONTINUE
2     CONTINUE

3     FORMAT(5X,E15 9,5X,E15 9,2X,E15 9,2X,E10 4,2X,E15 9)
4     FORMAT(5X,2(3X,E10 4))
25    FORMAT(5X,I9,5X,E10 4,5X,E10 4,5X,E10 4,5X,E10 4)
      END

```

An example of the output from this program is shown in figure C-1

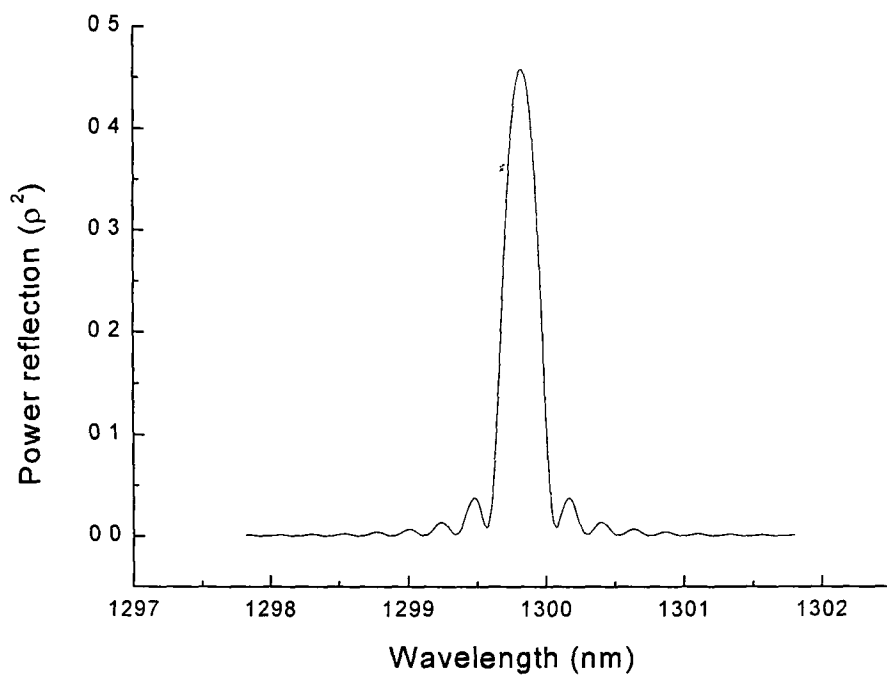


Figure C 1